TÉCNICO LISBOA

Computational fluid dynamics simulation of TPMS scaffolds for bone tissue engineering

Tiago Alexandre Hilário Veríssimo Pires

Thesis to obtain the Master of Science Degree in

Biomedical Engineering

Supervisors:

Prof. Paulo Rui Alves Fernandes

Prof. André Paulo Galvão de Castro

Examination Commitee

Chairperson: Prof. João Orlando Marques Gameiro Folgado

Supervisor: Prof. Paulo Rui Alves Fernandes

Members of the Commitee: Prof. Rui Miguel Barreiros Ruben

October 2019

Preface

Declaration

I declare that this document is an original work of my own authorship and that it fulfills all the requirements of the Code of Conduct and Good Practices of the Universidade de Lisboa.

This work presented in this thesis was performed at Instituto de Engenharia Mecânica of Instituto Superior Técnico (Lisbon, Portugal), during the period February-October 2019, under the supervision of Prof. Paulo Fernandes and Prof. André Castro.

Acknowledgments

I would like to express my sincerest gratitude to all of the people that helped me achieved what would otherwise be an impossible goal.

First and foremost, I would like to thank my supervisors, Prof. Paulo Fernandes and Prof. André Castro, for introducing me to this fascinating field of research and for assisting me every step of the way.

I would also like to thank Prof. José Miranda Guedes, for helping me better understand some of the intricacies around CFD analysis.

Additionally, I would like to thank all my friends and colleagues for their continuous support and cooperation throughout these demanding past months.

I also express my deepest thank you to my family. To my uncles (Francisco and Manuel), my aunt (Hermínia) and my cousins Filipe and Telma, who are always in my thoughts, no matter how far they might be. Finally, I would like to thank my mother Florbela Pires, my father António Pires and my grandmother Deolinda Hilário Veríssimo, for encouraging me to follow my interests and for supporting me all these years.

Abstract

Bones are a fundamental component of the human body given their multitude of functions. Thus, Bone Tissue Engineering has been focusing on improving the current methods for dealing with damaged bone. In this sense, the use of scaffolds has been presented as a possible alternative to traditional methods.

Scaffolds are artificially designed porous support matrices, meant to allow cell seeding and cell proliferation. These properties are influenced by the permeability of the scaffolds. Taking this into consideration, this work used Computational Fluid Dynamics models to analyse the permeability and fluid streamlines of different TPMS scaffold geometries. The results from the simulations were used to better understand the relation between a scaffold's geometry and its permeability values. The computational models are also compared to an experimental setup in order to be validated.

Because of the high computational cost to test the entire setup, three less demanding alternative models were designed. It was verified that the periodic model was the more appropriate, since it could be used for all of the designs keeping the original geometry. The results from the numerical analysis presented a good correlation with the experimental values, validating the computational models.

The analysis of the fluid streamlines revealed how the gyroid geometries are the most appropriate design for most cases of scaffold fabrication. The study of the streamlines also showed that the Schwarz D geometries were only appropriate for very specific scenarios and the tested Schwarz P geometries did not possess the desired qualities for cell seeding and proliferation.

Key-words: Bone Tissue Engineering; Scaffolds; Permeability; Triply Periodic Minimal Surfaces; Computational Fluid Dynamics; Streamlines

Resumo

Os ossos são uma componente fundamental do corpo humano dada a sua multiplicidade de funções. Assim, a Engenharia de Tecidos Ósseos foca-se em melhorar os métodos para lidar com ossos danificados. Neste sentido, o uso de scaffolds tem sido apresentado como alternativa aos métodos tradicionais.

Scaffolds são matrizes porosas de suporte, artificialmente desenhadas, com o propósito de permitir cultivo e proliferação celular. Estas propriedades são influenciadas pela permeabilidade dos scaffolds. Posto isto, este trabalho recorreu a modelos Dinâmicos de Fluídos Computacionais para analisar a permeabilidade e linhas de fluxo de diferentes geometrias TPMS de scaffold. Os resultados destas simulações contribuíram para a compreensão da relação entre a geometria de um scaffold e os seus valores de permeabilidade. Os modelos computacionais foram comparados a um setup experimental de forma a serem validados.

Devido ao elevado custo computacional para testar a totalidade do setup, foram desenhados três modelos alternativos menos exigentes. Verificou-se que o modelo periódico foi o mais apropriado, uma vez que podia ser usado para todos os designs mantendo a geometria original. Os resultados da análise numérica apresentaram uma boa correlação com os valores experimentais, validando os modelos computacionais.

A análise das linhas de fluxo revelou que as geometrias giroide são o design mais apropriado para a maior parte dos casos de fabricação de scaffolds. O estudo destas linhas demonstrou também que as geometrias Schwarz D eram apenas apropriadas para casos muito específicos e que as geometrias Schwarz P testadas não possuíam as qualidades desejadas para cultivo e proliferação celular.

Palavras Chave: Engenharia de Tecidos Ósseos; Scaffolds; Permeabilidade; Superfície Mínima Triplamente Periódica; Dinâmica de Fluídos Computacional; Linhas de Fluxo

Contents

Preface i

Acknowledgments iii

Abstract v

Resumo vii

List of Figures xi

List of Tables xv

Symbols and Abbreviations xvii

1. Introduction 1

1.1. Bone Biomechanics ... 1

1.2. Motivation and Objectives ... 3

1.3. Structure ... 4

2. Tissue engineering 5

2.1. Scaffold Requirements ... 5

2.2. Scaffold Production ... 6

2.2.1. Materials ... 6

2.2.1.1. Metal ... 6

2.2.1.2. Ceramic ... 7

2.2.1.3. Polymers ... 8

2.2.2. Manufacturing Techniques ... 8

2.2.3. TPMS geometry ... 10

2.3. Mathematical basis ... 11

2.3.1. Conservation Laws ... 11

2.3.1.1. Conservation of Mass/ Continuity Equation ... 11

2.3.1.2. Conservation of Momentum ... 12

2.3.1.3. Conservation of Energy ... 14

2.3.2. Navier-Stokes Equations ... 15

2.3.3. Darcy's law ... 16

2.4. CFD and FVM analysis ... 17

3. State of the Art 19

3.1. Permeability system ... 19

3.2. Numerical modeling ... 21

4. Methodology 29

4.1. Model geometry ... 29

4.1.1. Model shape and dimensions ... 29

4.1.2. Meshing ... 30

4.2. Numerical models ... 31

4.2.1. Periodic model ... 32

4.2.2. Symmetric model 33
4.2.3. Simplified model 34
4.3. Simulation parameters 35
5. Results **37**
5.1. Symmetric models 37
5.2. Periodic models 40
5.3. Simplified models 45
5.4. Model comparison 50
5.5. Experimental Results 55
5.6. Streamlines 57
6. Discussion **63**
6.1. Model Comparison 63
6.2. Geometry Influences 65
6.3. Streamline Analysis 66
6.4. Experimental comparison 67
7. Conclusions and future research **69**
7.1. Conclusions 69
7.2. Future research 70
Bibliography **73**
Appendix **79**
Experimental data **79**
ANSYS FLUENT Parameters **81**

List of Figures

Figure 1.1. Structure of the bone *(Tortora and Derrickson, 2014).*

Figure 2.1. Illustration of a 3x3 a) Schwarz P geometry, b) gyroid geometry and c) Schwarz D geometry *(Vijayavenkataraman et al., 2018).*

Figure 2.2. Representation of the shear stresses and normal stresses *(McDonough, 2009)*.

Figure 2.3. First bed of sand experimental setup for determining Darcy's law *(Darcy, 1856).*

Figure 3.1. Representation of the constant-head gravity permeability system (left) and the falling head gravity permeability system (right) *(Pennella et al., 2013)*.

Figure 3.2. Representation of the peristaltic pump permeability system *(Pennella et al., 2013)*.

Figure 3.3. Representation of the syringe pump permeability system *(Mohee et al., 2019)*.

Figure 3.4. Representation of the unitary cell (left) and cylindrical scaffold design (right) used by *Dias et al. (2012)*.

Figure 3.5. Unitary cells for the scaffold design in *Rahbari et al. (2016)*.

Figure 3.6. Experimental setup for the cell deposition tests (*Marin et al., 2017b)*.

Figure 3.7. Variation of computational normalized longitudinal permeability versus porosity for 5 lattice based and 4 TPMS based geometries *(Montazerian et al., 2017)*.

Figure 3.8. Variation of computational normalized radial permeability versus porosity for the 5 lattice based geometries *(Montazerian et al., 2017)*.

Figure 3.9. Velocity contours for Newtonian models on the left and the equivalent non-Newtonian models on the right*(Ali and Sen, 2018)*.

Figure 3.10. Comparison of the calculated permeability for Newtonian and non-Newtonian models *(Ali and Sen, 2018)*.

Figure 4.1. a) Image of all of the components of the permeability chamber; b) representation of the main permeability chamber and its dimensions and c) dimensions of the cover of the permeability chamber (to keep the scaffold inside the chamber).

Figure 4.2. Image of the lid of the permeability chamber (left) and its respective representation with its most relevant dimensions (right).

Figure 4.3. Representation of the CFD chamber with its dimensions.

Figure 4.4. Mesh of a single unitary cell for a SP70.

Figure 4.5. SP70 scaffold with a 1x1x4 configuration with the chamber attached.

Figure 4.6. Illustration of the Matlab routine on both planes. Scaffold with the chamber before the routine (top) and after the routine (bottom) viewed on the xy plane.

Figure 4.7. SP70 scaffold with a 2x2x4 configuration with the chamber attached.

Figure 4.8. Simplified SP70 scaffold with a 4x4x4 configuration with the chamber attached.

Figure 5.1. Streamlines for a SP70 scaffold with an inlet velocity of 5 ml/min, with a symmetry boundary condition in the right side (black line) and the middle of the model (purple line).

Figure 5.2. Comparison of the velocity contour of the fluid at the middle of the model (left) and at the symmetry plane (right) with an inlet velocity of 5 ml/min of a SP70 scaffold.

Figure 5.3. Calculated permeability in function of the flow rate for all of the four symmetric scaffold models.

Figure 5.4. Calculated permeability in function of the flow rate for periodic scaffold models with 50% porosity.

Figure 5.5. Calculated permeability in function of the flow rate for periodic scaffold models with 60% porosity.

Figure 5.6. Calculated permeability in function of the flow rate for periodic scaffold models with 70% porosity.

Figure 5.7. Calculated permeability in function of the flow rate for periodic scaffold models with 80% porosity.

Figure 5.8. Calculated permeability in function of the flow rate for simplified scaffold models with 50% porosity.

Figure 5.9. Calculated permeability in function of the flow rate for simplified scaffold models with 60% porosity.

Figure 5.10. Calculated permeability in function of the flow rate for simplified scaffold models with 70% porosity.

Figure 5.11. Calculated permeability in function of the flow rate for simplified scaffold models with 80% porosity.

Figure 5.12. Calculated permeability in function of the flow rate for the periodic and symmetric models of the SP50 scaffold.

Figure 5.13. Calculated permeability in function of the flow rate for the periodic and symmetric models of the SP60 scaffold.

Figure 5.14. Calculated permeability in function of the flow rate for the periodic and symmetric models of the SP70 scaffold.

Figure 5.15. Calculated permeability in function of the flow rate for the periodic and symmetric models of the SP80 scaffold.

Figure 5.16. Calculated permeability in function of the flow rate for all scaffold models with 50% porosity.

Figure 5.17. Calculated permeability in function of the flow rate for all scaffold models with 60% porosity.

Figure 5.18. Calculated permeability in function of the flow rate for all scaffold models with 70% porosity.

Figure 5.19. Calculated permeability in function of the flow rate for all scaffold models with 80% porosity.

Figure 5.20. Calculated permeability in function of the flow rate for the experimental values and periodic values of scaffolds with 60% porosity.

Figure 5.21. Calculated permeability in function of the flow rate for the experimental values and periodic values of scaffolds with 70% porosity.

Figure 5.22. Correlation between the computationally calculated permeability and the experimentally measured permeability for all of the 60% and 70% scaffold porosities.

Figure 5.23. Correlation between the computationally calculated permeability and the experimentally measured permeability for a) SP60, b) SP70, c) SD60, d) SD70, e) SG60 and f) SG70.

Figure 5.24. Overview of the streamlines of the a) SP70 scaffolds; b) SD70 scaffolds and c) SG70 scaffolds.

Figure 5.25. Side view of the streamlines of the a) SP70 scaffolds; b) SD70 scaffolds and c) SG70 scaffolds.

Figure 5.26. View from the outlet of the streamlines of the a) SP70 scaffolds; b) SD70 scaffolds and c) SG70 scaffolds.

Figure 5.27. Sideview of the wireframe plus streamlines with an inlet flwo rate of 10 ml/min of a) the SP70 scaffold and b) the SP50 scaffold.

Figure 5.28. Sideview of the streamlines of the SP70 scaffold with a) 20 ml/min inlet flow rate; b) 60 ml/min inlet flow rate c) 100 ml/min inlet flow rate.

List of Tables

Table 4.1. Number of nodes and elements for each periodic scaffold model with the chambers.

Table 4.2. Number of nodes and elements for each symmetric scaffold model with the chambers.

Table 4.3. Number of nodes and elements for each simplified scaffold model with the chambers.

Table 5.1. Conversion of the inlet flow rate to the numerical simulation's inlet velocity.

Table 5.2. Measured pressure difference of the numerical simulation of the symmetric models.

Table 5.3. Calculated pressure drop for the symmetric scaffolds.

Table 5.4. Resulting permeability for the symmetric scaffolds.

Table 5.5. Calculated pressure drop for the periodic SP scaffolds.

Table 5.6. Calculated pressure drop for the periodic SD scaffolds.

Table 5.7. Calculated pressure drop for the periodic SG scaffolds.

Table 5.8. Resulting permeability for the periodic SP scaffolds.

Table 5.9. Resulting permeability for the periodic SD scaffolds.

Table 5.10. Resulting permeability for the periodic SG scaffolds.

Table 5.11. Measured pressure difference of the numerical simulation of the simplified SP models.

Table 5.12. Measured pressure difference of the numerical simulation of the simplified SD models.

Table 5.13. Measured pressure difference of the numerical simulation of the simplified SG models.

Table 5.14. Calculated pressure drop for the simplified SP scaffolds.

Table 5.15. Calculated pressure drop for the simplified SD scaffolds.

Table 5.16. Calculated pressure drop for the simplified SG scaffolds.

Table 5.17. Resulting permeability for the simplified SP scaffolds.

Table 5.18. Resulting permeability for the simplified SD scaffolds.

Table 5.19. Resulting permeability for the simplified SG scaffolds.

Symbols and Abbreviations

m – mass [kg]

t – time [s]

V – fixed volume [m^3]

ρ – density [kg/m^3]

$\mathbf{U}$ – fluid velocity [m/s]

u, v and w – fluid velocity in the x, y and z direction, respectively [m/s]

F_x, F_y and F_z – forces acting on the volume in the x, y and z direction, respectively [N]

F_{Bx} – body forces acting on the volume in the x direction [N]

F_{Sx} – surface forces acting on the surface of the volume in the x direction [N]

S – Surface of the fixed volume [m^2]

F_B – body forces acting on the volume [N]

F_S – surface forces acting on the surface of the volume [N]

τ_{xx},τ_{yy} and τ_{zz} – normal stresses [Pa]

τ_{xy},τ_{xz},τ_{yx},τ_{yz},τ_{zx} and τ_{zy} – shear stresses [Pa]

n – outwards unit normal vector

σ – tensor of the viscous stresses and pressures applied to each surface

g – gravity force [m^2/s]

e – sum of the internal energy per unit mass

P – magnitude per unit area

q – conductive heat flux leaving the volume [W/m^2]

τ – viscous stresses tensor

g_x, g_y and g_z – gravity forces in the x,y and z directions [m^2/s]

K – permeability [m^2]

Q – flow rate [m^3/s]

μ – dynamic viscosity [Pa.s]

L – length [m]

A – cross sectional area of the flow [m^2]

ΔP – pressure difference / pressure drop [Pa]

Re – Reynolds number

D – diameter of the pipe [m]

3DF – 3D Fiber Deposition

BTE – Bone Tissue Engineering

CAD - Computer-Aided Design

CaP – Calcium Phosphate

CFD – Computational Fluid Dynamics

CoCr – Cobalt-Chrome

DLS – Digital Light Processing

EBM – Electron Beam Melting

FDM – Fused Deposition Modeling

FVM – Finite Volume Method

HA – Calcium Hydroxyapatite

LSCB – Least Sqaures Cell-Based

MJP – Multijet Printing

NiTi – Nickel-Titanium

PCL – Poly(caprolactone)

PGA – Poly(glycolic-acid)

PLA – Poly(lactic-acid)

SLA – Stereolithography

SLM – Selective Laser Melting

SLS – Selective Laser Sintering

Ta – Tantalum

TCP – Tricalcium Phosphate

TE – Tissue Engineering

TPMS – Triply Periodic Minimum Surfaces

1. Introduction

Originally, tissue engineering (TE) was broadly described as "*the application of principle and methods of engineering and life science towards the fundamental understanding of structure-function relationships in normal and pathological mammalian tissues and the development of biological substitutes to restore, maintain or improve tissue functions*" *(Skalak, 1988)*. Currently, TE is an expanding multidisciplinary field that includes the study of bioreactors, cell proliferation and scaffold production, among various other fields. This work centers on the area of TE that focuses on bone, called bone tissue engineering (BTE).

1.1. Bone Biomechanics

The primary support structure in the human body are the bones as described by *Tortora and Derrickson (2014)*, which are constituted by 15% water, 30% collagen fibers and 55% crystallized mineral salts (primarily calcium phosphate). Bones perform six main functions:

1. Provide a support structure for the body;
2. Protect the most important internal organs, such as the brain, heart and lungs from impact;
3. Assist with movement specifically the bones connected to skeletal muscles;
4. Store and release minerals to the body when necessary (mineral homeostasis);
5. Produce red blood cells in the red bone marrow and
6. Store triglycerides in yellow bone marrow in the form of adipose cells.

Bone, or osseous tissue, can be divided into two distinct tissue types: trabecular bone (also known as cancellous or spongy bone) and cortical bone (also known as compact bone).

The ratio of trabecular to cortical bone differs from bone to bone. However, cortical bone accounts for an average of 80% of all bone tissue whereas trabecular accounts for 20% *(Sikavitsas et al., 2001; Porter et al., 2009)*. Cortical bone tissue is composed of repeating structural units known as osteons, that consist of concentric lamellae around a central canal and, as seen in the Fig 1.1, it is mainly found on the exterior portion of the bone.

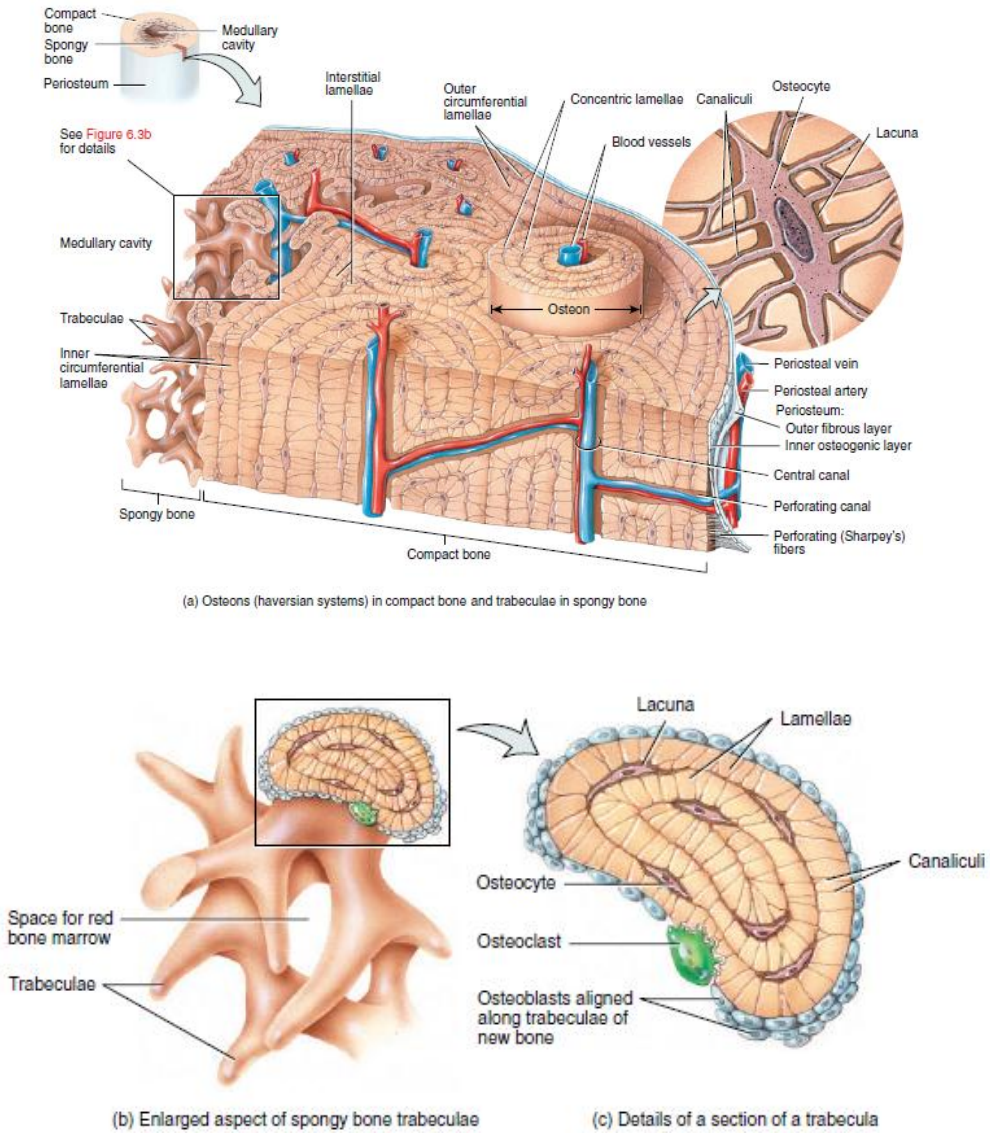

Figure 1.1. Structure of the bone *(Tortora and Derrickson, 2014).*

Trabecular bone is composed by lamellae arranged in thin columns known as trabeculae. The spaces between the trabeculae are filled with either red bone marrow or yellow bone marrow, depending on the type of bone. Due to the differences in configuration and function of these two types of bone tissue, they posses different porosity (trabecular bone is 50-90% porous whereas cortical is only 10%) and different ultimate compressive strength (cortical bone can have up to 10 times higher compressive strength than trabecular bone) *(Sikavitsas et al., 2001)*.

Considering the multitude of functions carried out by osseous tissues, any injury or defect on the tissue that cannot be easily repaired (these complications can be pathological, traumatic or surgical in nature) represents an issue that demands quick intervention. *Porter et al. (2009)* illustrates how the current standard for addressing these lesions is typically bone grafting, which consist of removing the damaged bone and replacing it with healthy tissue. The transplanted bone tissues can be an autograft, allograft or xenograft, depending on the origin of the tissue.

An autograft involves transplanting a patient's healthy osseous tissue from one area (normally from the pelvis or iliac crest) to another in order to replace a portion of damaged bone. Despite being the most common treatment, it has a number of severe complications. In up to 30% of cases the symptoms of these complications include pain, higher risk of infection, inflammation, hematoma and paresthesia, among others *(Porter et al., 2009)*.

In an allograft, the transplanted bone originates from another human body. It may be sourced from either viable (living) or sterilized non-viable sources. However, it still presents severe complications in disease transmission and host immune responses to the foreign body.

The third, and less frequent, type of bone graft is the xenograft, which is a graft from a non-human animal. Despite this technique having showed some early promise, it is now considered unsuitable due to the high risk of disease transmission, virus transmission, infection, toxicity (from the sterilization process) and host rejection *(Porter et al., 2009)*.

In an attempt to overcome the current limitations of bone grafting, BTE has been researching the creation, utilization and optimization of scaffolds. These scaffolds are artificially designed porous support matrices, meant to allow cell seeding and cell proliferation. This can happen in either an in vivo setting (implant) or an in vitro setting (bioreactor). Thus, scaffolds could be used for both trabecular and cortical bone, with the required geometric configurations. However, this implies the need for a much more in-depth study of the different properties of each one of the possible geometries.

1.2. Motivation and Objectives

The motivation for the work is further encourage the use of scaffolds as a viable alternative to bone grafts in BTE. To achieve this, there is a need for more in depth studies to better understand one of the scaffold's most important characteristics: its geometry. This geometry is responsible not only for how much mechanical support the scaffold provides, but also for determining how cells will enter and interact with it. Therefore, it's essential to understand how different geometries will influence all of the different scaffold properties.

The main purpose of this work is to determine the influence of different scaffold geometries on its fluidic properties, namely its permeability. To this end, a computational fluid dynamics (CFD) analysis will be used to simulate an experimental setup, designed to obtain the permeability of twelve distinct geometries. The permeabilities obtained (alongside the flow streamlines of the CFD) will be compared between themselves to better understand how a change in a scaffold's geometry changes the fluid flow inside of it.

The results obtained from this study aspire to lead to a better comprehension of which geometry is more appropriate for which situation and a more careful analysis of the flow conditions inside a scaffold when designing its geometry.

1.3. Structure

This work is divided into seven chapters: 1. Introduction; 2. Tissue engineering; 3. State of the Art; 4. Methodology; 5. Results; 6. Discussion and 7. Conclusions and future research.

Chapter 1. Introduction

This chapter provides an initial view into the subject of bones and BTE as well as the motivation behind the development of this work. It also shows the structure of the thesis.

Chapter 2. Tissue engineering

This chapter presents the necessary background regarding tissue engineering. This includes the explanation behind both the conservation and Darcy's laws; the requirements and production methods of a scaffold and the basis behind a finite volume method analysis.

Chapter 3. State of the Art

This chapter focuses on a historic look into the advances of numerical modelling regarding permeability analysis of scaffolds meant for BTE. It also discusses the different types of available systems to access a scaffold's permeability.

Chapter 4. Methodology

This chapter explains the chosen geometry to be tested; the different models created to evaluate the geometry and the parameters selected for the numerical simulations.

Chapter 5. Results

This chapter lays out the obtained pressured drops as well as the desired calculated permeabilities of every different scaffold for each of the created models. It also shows the comparisons of these results among themselves and between experimental results.

Chapter 6. Discussion

In this chapter, the results from the previous chapter are analysed in depth by comparing the calculated permeability values to the flow streamlines in order to better understand the flow inside the permeability chamber.

Chapter 7. Conclusions and future research

Finally, conclusions regarding the permeability of all of the scaffolds are drawn based on the observations from the previous chapter. Suggestions for possible future research in this area are also presented.

2. Tissue Engineering

2.1. Scaffold Requirements

Porter et al. (2009) outlines 11 requirements that would ideally need to be met by any scaffold intent on replacing damaged bone tissue; which are:

1. Providing mechanical support for the injured bone;
2. Allowing substrate deposition inside the scaffold;
3. Allowing vascularisation inside the pores of the scaffold;
4. Encouraging cell migration into the scaffold;
5. Promoting osteogenic differentiation;
6. Enhancing osseointegration;
7. Degrading in a similar rate to bone growth;
8. Only producing non-toxic degradation products;
9. Not inducing any inflammatory response;
10. Being capable of sterilization without loss of bioactivity and
11. Delivering bioactive molecules/drugs to accelerate healing whilst preventing any pathology.

While point 11 is a very desirable characteristic for scaffolds, it isn't inherently necessary. However, the remaining 10 points are all mandatory. Point 1 relates to the main function of bones in the human body, to provide its primary support structure, with any implanted scaffold having to provide a similar level of mechanical support.

Points 2-6 relate to the geometry of the scaffold itself, which needs to stimulate the cells of the human body to migrate inside the scaffold. Afterwards, these cells need to differentiate into bone tissue and blood vessels. These characteristics are directly connected with a very important characteristic in BTE; that of permeability. A scaffold's permeability will influence cell seeding, its differentiation and its growth, making it an essential parameter to consider in scaffold production. *Rahbari et al. (2016)* and *Dias et al. (2012)* discuss how higher scaffold permeability generates better conditions for cell growth inside them and how this permeability is dictated by the pore size and porosity of scaffolds. These studies also indicate how larger pore sizes and higher porosities lead to more permeable scaffolds. However, higher permeability in scaffolds is not without its limitations. *Melchels et al. (2010)* notes that when permeability is too high, all cells are able to pass through the scaffold, stopping cells adhering to its walls. Furthermore, in trying to reach higher permeability, the mechanical properties might be compromised, missing the previously established point 1 *(Rahbari et al, 2016)*. To reach the balance between the mechanical properties and permeability of the scaffolds, it was determined that the ideal pore diameter was around 300 µm in order to obtain the desired vascularisation *(Hutmacher et al., 2007)*. However, a minimum diameter of 100 µm would be sufficient to allow the passage of cells.

Another point that also conflicts with mechanical support is the degradation rate, because if the scaffolds degrades too quickly the structural properties might be compromised. In order for both of

these points to be satisfied, the scaffolds need to not only provide similar structural support as bone but also degrade at a similar rate to the bone growth rate. Thus, scaffolds need to facilitate the transfer of the load from their degrading structure to the newly formed bone. *Porter et al. (2009)* and *Hutmacher et al. (2007)* indicate that scaffolds need to maintain structural properties for the initial 1-3 months and need to be fully reabsorbed within approximately 12-18 month in order to meet both established requirements.

The concern with not producing toxic products, and not inducing an inflammatory response, accentuate the interaction of the scaffold with the human body as a foreign object.

Another consideration is that scaffolds must also be capable of simultaneously undergoing sterilization (so it can be used as a transplant) while not losing its bioactivity (so it can stimulate biochemical responses from the surrounding tissues).

A final consideration, when designing scaffolds, is the inherent variability associated with its manufacturing. *Brunelli et al. (2017)* and *Marin and Lacroix (2015)* discuss how this variability can affect several mechanical and fluidic properties of said scaffolds. This means that imprecisions in geometry, because of the manufacturing method, must also be taken into account when designing scaffolds, at least until newer fabrication techniques that drastically reduce this imprecision are developed and made available.

2.2. Scaffold Production

In order to fulfill the previously discussed scaffold requirements for a successful bone transplant, the three principal characteristics to look into are the material of the scaffold, the chosen printing technique and its internal structure (which is influenced by the chosen geometry and porosity). All of these contents will be analysed in the following chapters.

2.2.1. Materials

Scaffold fabrication in the field of BTE requires the use of different materials, either as an isolated material or a combination of metals, ceramics and/or polymers.

2.2.1.1. Metal

Since the early onset of surgical processes, metal and metallic alloys have always been a material to consider when designing new tools and implants, with scaffolds being no exception. A major appeal of a scaffold-based geometry for creating larger metal implants is the reduction of stress shielding when compared to a full metal implant. The dominant type of metals for these implants that were discussed by *(Kelly et al., 2017)* are titanium alloys (Ti-6Al-4V), with the occasional nickel-titanium (NiTi), cobalt-chrome (CoCr) and Tantalum (Ta). However, *Tan et al. (2013)* and *Porter et al. (2009)* raised the pressing matter that these metals still present a degree of stress shielding which can cause

osteoporosis and corrosion, leading to necessary follow-up surgeries. In an attempt to side-step this complication while maintaining the inherent desired mechanical properties of metals, a new solution is being investigated: biodegradable magnesium based metals *(Tan et al., 2013)*. The main draw of these materials is that they can degrade inside the human body (thus hopefully eliminating any future surgeries) while possessing a much closer density (1.7-2.0 g/cm^3) and elastic modulus (45 GPa) to bone than other metals. The main issue currently facing magnesium based metals is the degradation rate, which is too fast. As such, it can induce hemolysis, osteolysis, stimulation of gas bubbles and a rapid decrease of the desired mechanical properties. To correct this, new magnesium alloys are being developed and studied; such as Mg-Ca, Mg-Zn and Mg-RE alloys.

2.2.1.2. Ceramic

Ceramic materials, similar to metals, have a long history in the field of prosthesis manufacturing and are also a material to consider when designing scaffolds. As described by *Hutmacher et al. (2007)* the main appeal of ceramic as a material for surgical applications is its similarity to the biological environment, resulting in a significantly lower risk of inflammatory responses. Other favourable characteristics of ceramic materials are its high compressive strength, high wear resistance and low frictional properties.

When looking to transpose these benefits of ceramics to scaffold manufacturing, degradability is an important factor to take into consideration. *Oh et al. (2006)* presents one of the most common families of ceramic material that allows the creation of biodegradable scaffolds: calcium phosphate (CaP), which is also biodegradable and allows for osteoconductivity. Inside CaP materials, two of the most utilized are calcium hydroxyapatite (HA) and Tricalcium phosphate (TCP).

HA is a highly crystalline form of calcium phosphate with its synthetic form being produced through a reaction at high temperatures. In addition, HA is a chemical analog of human bone mineral which explains its high rate of biocompatibility and osteoconductive potential. TCP is also a biodegradable and bioactive bone replacement material with a chemical composition and crystallinity approximate to the mineral phase of bone, but it has a much higher degradation rate than HA, approximately three to twelve times higher *(Hutmacher et al., 2007)*. However, the brittleness of CaP materials means that they are a poor choice for situations involving high compressive loading on bones.

A final possibility discussed by *Tan et al. (2013)* for a biodegradable material is bioactive glass-ceramic, which falls into the bioactive classification due to the formation of HA crystal on the surface of the glass, after contact with the biological medium. This is a material that contains small amounts of a crystalline phase, namely apatite, β-wollastonite, phologopite and witolikte. This material has had some usage in reconstructive surgeries and its application for scaffold manufacturing is a very relevant topic in current research *(El-Rashidy et al., 2017)*.

2.2.1.3. Polymers

The third and most promising material are polymers which are macromolecules composed of a large number of monomers connected through covalent bonds. The importance of this material in the field of scaffold fabrication is because of its availability, ease in manufacturing and inherent degradability (which as discussed previously is a fundamental necessity in scaffold design). This degradability in polymers can occur through two distinct paths, either surface degradation or bulk degradation. In surface degradation, the molecules at the surface degrade faster than the overall material, allowing for the majority of the material to maintain its structural integrity. In contrast, in bulk degradation the rate of fluid penetration and material degradation exceeds the solubilisation rate of the surface, causing the loss of the structural properties of the material *(Porter et al., 2009)*.

Polymers can be divided into natural polymers and synthetic polymers according to its origin. Natural polymers can be further subdivided into polysaccharides polymers (which include starch, alginate, chitosan and hyaluronic acid derivatives) and protein polymers (collagen and fibrin). However, these natural materials have several drawbacks when compared to synthetic ones. These drawbacks include an overall lower mechanical properties, higher physiological activity and higher variance in degradation rate. Synthetic polymers lack these flaws and have already been reported by *Tan et al. (2013)* to be non-toxic and have controllable degradation rates, so much so that some of these synthetic polymers have already been used as degradable surgical sutures.

There exists several kinds of synthetic biodegradable polymers; and new ones are currently being developed. However, the most commonly used polymers are poly(lactic-acid) (PLA), poly(glycolic-acid) (PGA) and poly(caprolactone) (PCL) and all their respective copolymers. PLA is of the three, the most used polymer and the one with the most clinical research, however *Porter et al. (2009)* discusses how, due to possessing the lowest modulus of the main polymers, it is normally made into a composite with another material in order to obtain a higher modulus. PGA has a higher modulus than PLA but because of its hydrophilism it has the highest degradation rate, limiting its application in TE. Finally, PCL is the polymer that presents the highest modulus alongside the lowest degradation rate, making it a favourable material in the fields of orthopaedics and drug delivery devices. Furthermore, the products resulting from the degradation of PCL are more easily absorbed in the human body than the glycolides and polylactides from PLA and PGA.

Considering the characteristics discussed in all these materials, namely their strengths and limitations, their choice in scaffold fabrication is still an ongoing field of research.

2.2.2. Manufacturing Techniques

Having looked into the different materials that can make up a scaffold, another key aspect in creating scaffolds is how they are manufactured. This is important, because each type of manufacturing process has distinct benefits and some of these methods can only be utilised for specific types of materials. This work will focus on the predominant type of scaffold manufacturing techniques, that are 3D printing methods. Per *Kelly et al. (2017)*, the most common 3D printing methods are:

- Powder bed fusion methods: this method can be divided into three more specific methods which are electron beam melting (EBM), selective laser sintering (SLS) and selective laser melting (SLM). Overall, all of these methods consist on the same principle of melting/sintering of the chosen material (in powder form) layer by layer to create the desired shape. The main differences between the methods are 1) whether they are melting or sintering the powder, and 2) the cooling rate (with SLM having a much higher cooling rate that EBM). From these three printing methods, SLM can be used to print all materials; SLS can be used to print polymer and ceramic based designs and EBM can only be used for metals. Furthermore, SLM and EBM are almost always the only 3D printing techniques used for metals designs.

- Fused deposition modeling (FDM): this is one of the most commonly used methods of polymer methods and consists in continuously heating and melting a thermoplastic polymer in a heated chamber, and applying pressure to push the melted polymer through the nozzle. Afterwards, the part is built layer by layer, from the bottom up. One of the limitations of this method is the fact that using it with softer polymers can be more problematic than with harder polymers due to the higher risk of buckling. Besides polymers, FDM can also be used to create ceramic and metallic parts (although is it very rarely used for metallic parts).

- 3D fiber deposition (3DF): this is an analogous method to FDM but without the melting of the material, being used for either extremely soft materials like hydrogels, or materials that solidify after leaving the syringe.

- Stereolithography (SLA): the main focus of this method is the selective solidification of sequential layers of a liquid polymer resin through photopolymerization. In each layer, the laser traces the design of the desired part to only photopolymerize that portion. Afterwards, a new resin layer is added on top and this cycle repeats itself until the part is completed. When compared to other methods, SLA offers the benefit of allowing the creation of much more complex geometries; however, due to the necessity of the photopolymer resins, which are normally toxic, the parts created by this technique are very limited in terms of implantation options.

- Digital light processing (DLS): this technique is very similar to SLA, including its benefits and drawbacks with the defining difference being that in DLS the entire layer of polymer resin is cured at the same time by projecting light through an optical mask.

- Inkjet printing: this method consists on an inkjet head with thousands of small nozzles, which selectively deposit the material layer by layer in droplet form. The major complication with this method is, once again, the material; which has to be either a melted wax or a low viscosity photopolymer in order to pass through the nozzles. A type of inkjet printing is Multijet Printing

(MJP) which casts the chosen printing material with a wax support layer by layer. This MJP technique is the one this work will focus on.

2.2.3. TPMS Geometry

Several different geometries have been considered when designing scaffolds for TE, for example, *Montazerian et al. (2017)* studied the permeability of several distinct geometries ranging from simpler lattice geometries to much more complex triply periodic minimum surfaces (TPMS). As expected, the TPMS structures always outperform the other designs (when comparing designs with the same porosity), revealing the benefits of choosing these geometries when attempting to optimize the permeability of scaffold meant for bone implantation. Accordingly, this work will be focussed on analysing scaffolds designed with the three most commonly studied TPMS geometries: Schwartz P, Schwartz D and gyroid.

A minimal or zero-mean curve surface is defined as a surface that is locally area-minimizing; this means that for a given boundary condition, these surfaces will have a minimal surface area. If these surfaces also have translational symmetry in three independent directions (x, y and z directions), then they are also triply periodic (TPMS). The main characteristic that makes TPMS appealing as a possible geometry for TE is their lack of self-intersection, resulting in geometries with no cut off portions, or in a biological perspective, no areas where cells couldn't interact.

The first TPMS were designed by German mathematician Karl Hermann Schwarz at the end of the 19th century that includes Schwarz P, Schwarz D, Schwarz H and Schwarz CLP. From these geometries the ones that are more frequently studied, as previously mentioned, are the Schwarz P which stand for Schwarz "Primitive" and the Schwarz D which stand for Schwarz "Diamond". Schwarz P as indicated by their name is one of the simplest TPMS geometry, being approximated by the following equation *(Dinis et al., 2014)*:

$$\cos(x) + \cos(y) + \cos(z) = 0 \tag{2.1}$$

Schwarz D is a fairly more complex geometry that can be approximated by the following equation:

$$\sin(x) * \sin(y) * \sin(z) + \sin(x) * \cos(y) * \cos(z) +$$

$$+ \cos(x) * \sin(y) * \cos(z) + \cos(x) * \cos(y) * \cos(z) = 0 \tag{2.2}$$

The third considered geometry for this work was the gyroid geometry, discovered by American physicist Alan H. Schoen in the 1970s. This is the most complex out of all three geometries because it possesses neither planar symmetries nor any straight lines, being composed of curved surfaces. It is approximated by:

$$\cos(\mathrm{x}) * \sin(\mathrm{y}) + \cos(\mathrm{y}) * \sin(\mathrm{z}) + \cos(\mathrm{z}) * \sin(\mathrm{x}) = 0 \tag{2.3}$$

These geometries are illustrated in Figure 2.1.

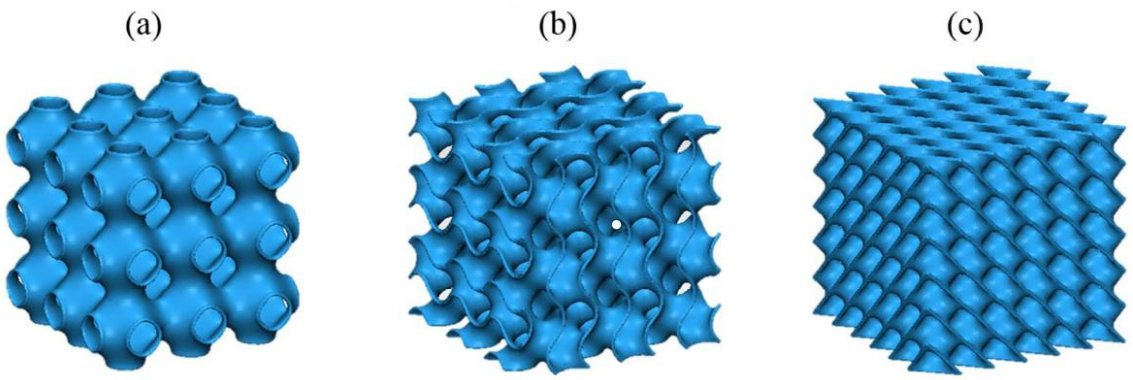

Figure 2.1. Illustration of a 3x3 a) Schwarz P geometry, b) gyroid geometry and c) Schwarz D geometry *(Vijayavenkataraman et al., 2018)*.

To create the 3D scaffolds out of these geometrical surfaces, *(Dinis et al., 2014)* developed a software application that receives the desired type of surface, the number as cubic elements per side of the design (determines the precision of the scaffold) and the + hole size and – hole size parameters. These hole size parameters determine the quantity of "material" added on each side of the surface, transforming it into a 3D geometry. To ensure the original surface is the center of the geometry, it's preferable to use the same value for both the + hole size and – hole size parameters. Finally, the software then returns the calculated porosity of the scaffold as well as the necessary files to allow the scaffold to be printed using a 3D printer.

2.3. Mathematical Basis

The mathematical basis for solving numerical simulations, involving fluids and the calculation of a porous media's permeability, are the continuity laws, the Navier-Stokes equations and Darcy's law. These laws are the basis for this work's computational analysis and are discussed in the following chapters.

2.3.1. Conservation Laws

To give answers to numerical fluid analysis, there is a set of three fundamental laws: the conservation laws (the conservation of mass/the continuity equation, the conservation of momentum and the conservation of energy). In this chapter, these laws will be further explored, based on *Chandran et al. (2012)* and *McDonough (2009)*.

2.3.1.1. Conservation of Mass / Continuity Equation

The law of conservation of mass states that for an arbitrary fixed volume V, where a fluid flows through it, the rate of change of mass of the fluid is equal to the rate of the mass going into the volume minus the rate of mass coming out of the system. Furthermore, if fluid in the system is

incompressible and with a constant density ρ, then this means that, for our constant volume, the mass of the fluid remains unchanged. This relation can be expressed by the following equation:

$$\frac{dm}{dt} = \frac{d}{dt}\int_V \rho \, dV = 0 \tag{2.4}$$

Afterwards, expanding this expression using the Reynolds Transform and the Gauss theorem, results in:

$$\int_V \frac{\partial \rho}{\partial t} + \rho \, \nabla \mathbf{U} \, dV = 0 \tag{2.5}$$

In this equation, $\mathbf{U}$ ($\mathbf{U} = u\,\overrightarrow{e_x} + v\,\overrightarrow{e_y} + w\,\overrightarrow{e_z}$) is equal to the velocity of the flow.

Finally, since the volume V is chosen arbitrarily, this means that the expression must be equal to zero for any volume, which means that the inside of the integration must be zero:

$$\frac{\partial \rho}{\partial t} + \rho \, \nabla \mathbf{U} = 0 \tag{2.6}$$

As mentioned previously, the fluid we are studying is being considered as incompressible and with a constant density, therefore the expression 2.6 can ultimately be simplified to:

$$\nabla \mathbf{U} = 0 \tag{2.7}$$

2.3.1.2. Conservation of Momentum

Considering Newton's second law of motion that states that the variation of momentum of a body is equal to the forces acting on said body, then these forces can be represented as:

$$F_x = \frac{d(mu)}{dt}, F_y = \frac{d(mv)}{dt}, F_z = \frac{d(mw)}{dt} \tag{2.8}$$

If instead of studying momentum variation, the variation of momentum per unit volume was studied, the expression would be:

$$\frac{F_x}{V} = \frac{d(\rho u)}{dt}, \frac{F_y}{V} = \frac{d(\rho v)}{dt}, \frac{F_z}{V} = \frac{d(\rho w)}{dt} \tag{2.9}$$

For the following segments only the x component will be analyzed, because the remaining two components would have a similar approach.

Considering an Eulerian view of the fluid flow, the left-side component of equation 2.9 can be written as:

$$\frac{F_x}{V} = \frac{D}{Dt}\int_V \rho u \, dV \tag{2.10}$$

Using Reynolds Transport Theorem, followed by the Gauss Theorem and considering again an incompressible flow ($\nabla \mathbf{U} = 0$) with a constant density ρ:

$$\frac{F_x}{V} = \int_V \rho \frac{Du}{Dt}\, dV \tag{2.11}$$

The right-side part of equation 2.9 can be divided into two segments, the body forces that act on the entire volume plus the surface forces that act on the surface of the volume, resulting in the following expressions for the x component and the overall expression, respectively:

$$\frac{d(\rho u)}{dt} = \int_V F_{Bx}\, dV + \int_S F_{Sx}\, dS \tag{2.12a}$$

$$\frac{d(\rho \mathbf{U})}{dt} = \int_V F_B\, dV + \int_S F_S\, dS \tag{2.12b}$$

The surface forces are given by the combination of the viscous stresses (σ) and the pressures (τ) as shown in Figure 2.2. The normal stresses are given by τ_{xx},τ_{yy} and τ_{zz}, while the shear stresses are given by τ_{xy},τ_{xz},τ_{yx},τ_{yz},τ_{zx} and τ_{zy}. The shear stresses can be simplified:

$$\tau_{xy} = \tau_{yx}\,, \tau_{xz} = \tau_{zx}\,, \tau_{yz} = \tau_{zy} \tag{2.13}$$

This simplification allows for the implementation of fewer variables, resulting in easier future calculations. Afterwards, the force F_S can be represented as $\sigma . n$, where n is the outwards unit normal vector to the surface S and σ is the tensor which represents the viscous stresses and pressures applied to each surface, given by:

$$\sigma = \begin{bmatrix} -\rho + \tau_{xx} & \tau_{xy} & \tau_{xz} \\ \tau_{xy} & -\rho + \tau_{yy} & \tau_{yz} \\ \tau_{xz} & \tau_{yz} & -\rho + \tau_{zz} \end{bmatrix} \tag{2.14}$$

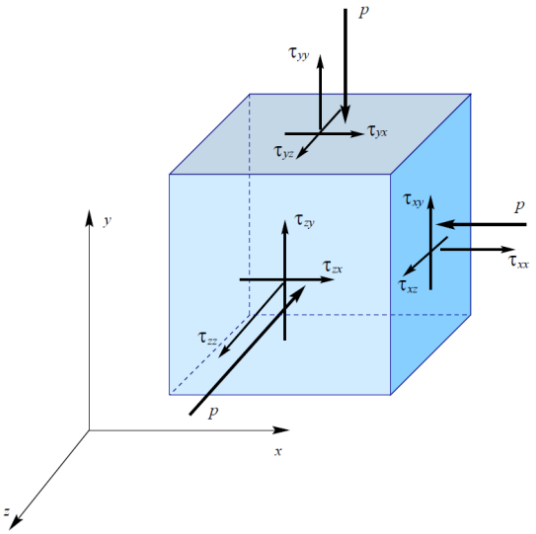

Figure 2.2. Representation of the shear stresses and normal stresses *(McDonough, 2009)*.

Regarding the body forces, they are typically caused by the presence of gravitational, electromagnetic and electrotactic fields, however, in the study of fluids, the traditional assumption only considers the gravitational force, such that:

$$\mathrm{F_B} = \rho \mathrm{g} \tag{2.15}$$

After all these simplifications, the conservation of momentum equation is given by:

$$\rho \frac{\partial \mathbf{U}}{\partial \mathrm{t}} + \rho \mathbf{U} \,.\, \nabla \mathbf{U} - \rho \mathrm{g} - \nabla \sigma = 0 \tag{2.16}$$

2.3.1.3. Conservation of Energy

This chapter focuses on the conservation of energy equation as described by *Currie (2012)*. This equation is derived from the first law of thermodynamics which states that the change in the energy of the system is equal to the sum of the total work done on the system plus any heat that was added to it. This total energy in fluids is composed by the sum of the internal energy per unit mass (e) with the kinematic energy per unit mass and considering, once again, an arbitrary volume V the total energy contained on that volume will be:

$$\int_{\mathrm{V}} \rho \mathrm{e} + \frac{1}{2} \rho \, \mathbf{U} . \mathbf{U} \, \mathrm{dV} \tag{2.17}$$

Regarding the total work done to the system, as established in chapter 2.3.1.2., the forces responsible for the work can be divided into surface forces or body forces (of which only the gravitational forces are considered). This work is given by the product of the velocity and the component of each force that is collinear with the velocity. This means that the total energy difference per volume is going to be equal to the work done by the surface forces plus the work done by the body forces minus the net amount of heat leaving the fluid per unit time. This results in the following equation:

$$\frac{D}{Dt} \int_{\mathrm{V}} \rho \mathrm{e} + \frac{1}{2} \rho \, \mathbf{U} . \mathbf{U} \, \mathrm{dV} = \int_{\mathrm{S}} \mathbf{U} . \mathrm{PdS} + \int_{\mathrm{V}} \mathbf{U} . \rho \mathrm{g dV} - \int_{\mathrm{S}} \mathrm{q} \,.\, \mathrm{ndS} \tag{2.18}$$

In this equation, P represents the magnitude per unit area, q is the conductive heat flux leaving the control volume and n is the unit outward normal.

Knowing that P can be written as $\sigma.\mathrm{n}$; using the Reynold's Transport Theorem and the Gauss Theorem and the fact that this expression must be equal to zero for any value of V, allows the equation to be written as:

$$\frac{\partial}{\partial t} \left(\rho \mathrm{e} + \frac{1}{2} \rho \, \mathbf{U} . \mathbf{U} \right) + \nabla \left(\rho \mathrm{e} + \frac{1}{2} \rho \, \mathbf{U} . \mathbf{U} \right) \mathbf{U} \, - \nabla \mathbf{U} \sigma - \mathbf{U} . \rho \mathrm{g} + \nabla \mathrm{q} = 0 \tag{2.19}$$

Further developing the first two components of the expression 2.16 and using equation 2.3 we obtain:

$$\rho\frac{\partial e}{\partial t}+\rho\mathbf{U}\frac{\partial \mathbf{U}}{\partial t}+\rho\mathbf{U}\nabla e+\rho\mathbf{U}.\mathbf{U}\nabla\mathbf{U}-\mathbf{U}\nabla\sigma-\sigma\nabla\mathbf{U}-\mathbf{U}.\rho g+\nabla q=0 \quad (2.20)$$

Finally considering equation 2.16 (with each component multiplied by $\mathbf{U}$) the simplified final expression for the energy conservation law is obtained:

$$\rho\frac{\partial e}{\partial t}+\rho\mathbf{U}\nabla e-\sigma\nabla\mathbf{U}+\nabla q=0 \quad (2.21)$$

2.3.2. Navier-Stokes Equations

Having obtained the conservation of mass and momentum expressions as well as calculated the σ tensor, it's possible to obtain the Navier-Stokes Equations. These are the governing equations that describe the motion of a fluid at any time or location within the flow field. To obtain them, it's first necessary to calculate $\nabla\sigma$:

$$\nabla\sigma=\left(-\frac{\partial\rho}{\partial x}+\frac{\partial\tau_{xx}}{\partial x}+\frac{\partial\tau_{xy}}{\partial y}+\frac{\partial\tau_{xz}}{\partial z}\right)\overrightarrow{e_x}+\left(-\frac{\partial\rho}{\partial y}+\frac{\partial\tau_{xy}}{\partial x}+\frac{\partial\tau_{yy}}{\partial y}+\frac{\partial\tau_{yz}}{\partial z}\right)\overrightarrow{e_y}+\left(-\frac{\partial\rho}{\partial z}+\frac{\partial\tau_{xz}}{\partial x}+\frac{\partial\tau_{yz}}{\partial y}+\frac{\partial\tau_{zz}}{\partial z}\right)\overrightarrow{e_z} \quad (2.22)$$

Replacing the tensor for equation 2.22, the conservation of momentum law can be written as a combination of three equations (one for each axis of motion):

$$\rho\frac{Du}{Dt}=\rho\frac{\partial u}{\partial t}+\rho\left(u\frac{\partial u}{\partial x}+v\frac{\partial u}{\partial y}+w\frac{\partial u}{\partial z}\right)=\rho g_x-\frac{\partial\rho}{\partial x}+\frac{\partial\tau_{xx}}{\partial x}+\frac{\partial\tau_{xy}}{\partial y}+\frac{\partial\tau_{xz}}{\partial z} \quad (2.23a)$$

$$\rho\frac{Dv}{Dt}=\rho\frac{\partial v}{\partial t}+\rho\left(u\frac{\partial v}{\partial x}+v\frac{\partial v}{\partial y}+w\frac{\partial v}{\partial z}\right)=\rho g_y-\frac{\partial\rho}{\partial y}+\frac{\partial\tau_{xy}}{\partial x}+\frac{\partial\tau_{yy}}{\partial y}+\frac{\partial\tau_{yz}}{\partial z} \quad (2.23b)$$

$$\rho\frac{Dw}{Dt}=\rho\frac{\partial w}{\partial t}+\rho\left(u\frac{\partial w}{\partial x}+v\frac{\partial w}{\partial y}+w\frac{\partial w}{\partial z}\right)=\rho g_z-\frac{\partial\rho}{\partial z}+\frac{\partial\tau_{xz}}{\partial x}+\frac{\partial\tau_{yz}}{\partial y}+\frac{\partial\tau_{zz}}{\partial z} \quad (2.23c)$$

Furthermore, the tensor τ(the viscous stresses tensor) can be expressed as:

$$\tau=\begin{bmatrix}\tau_{xx}&\tau_{xy}&\tau_{xz}\\ \tau_{xy}&\tau_{yy}&\tau_{yz}\\ \tau_{xz}&\tau_{yz}&\tau_{zz}\end{bmatrix}\Leftrightarrow\mu\begin{bmatrix}2\frac{\partial u}{\partial x}&\left(\frac{\partial u}{\partial y}+\frac{\partial v}{\partial x}\right)&\left(\frac{\partial w}{\partial x}+\frac{\partial u}{\partial z}\right)\\ \left(\frac{\partial u}{\partial y}+\frac{\partial v}{\partial x}\right)&2\frac{\partial v}{\partial y}&\left(\frac{\partial v}{\partial z}+\frac{\partial w}{\partial y}\right)\\ \left(\frac{\partial w}{\partial x}+\frac{\partial u}{\partial z}\right)&\left(\frac{\partial v}{\partial z}+\frac{\partial w}{\partial y}\right)&2\frac{\partial w}{\partial z}\end{bmatrix} \quad (2.24)$$

Finally, replacing the values of the viscous stresses tensor in the equations 2.20 with their values as expressed in equation 2.21 (and considering an incompressible fluid with constant density and viscosity), results in:

$$\rho\left(\frac{\partial u}{\partial t}+u\frac{\partial u}{\partial x}+v\frac{\partial u}{\partial y}+w\frac{\partial u}{\partial z}\right)=\rho g_x-\frac{\partial \rho}{\partial x}+\mu\left(\frac{\partial^2 u}{\partial x^2}+\frac{\partial^2 u}{\partial y^2}+\frac{\partial^2 u}{\partial z^2}\right) \quad (2.25a)$$

$$\rho\left(\frac{\partial v}{\partial t}+u\frac{\partial v}{\partial x}+v\frac{\partial v}{\partial y}+w\frac{\partial v}{\partial z}\right)=\rho g_y-\frac{\partial \rho}{\partial y}+\mu\left(\frac{\partial^2 v}{\partial x^2}+\frac{\partial^2 v}{\partial y^2}+\frac{\partial^2 v}{\partial z^2}\right) \quad (2.25b)$$

$$\rho\left(\frac{\partial w}{\partial t}+u\frac{\partial w}{\partial x}+v\frac{\partial w}{\partial y}+w\frac{\partial w}{\partial z}\right)=\rho g_z-\frac{\partial \rho}{\partial z}+\mu\left(\frac{\partial^2 w}{\partial x^2}+\frac{\partial^2 w}{\partial y^2}+\frac{\partial^2 w}{\partial z^2}\right) \quad (2.25c)$$

These final three equations are the Navier-Stokes Equations represented through with cartesian coordinates.

2.3.3. Darcy's law

As discussed in a chapter 2.1., the permeability of bone, and consequently of any scaffold designed to replace damaged bone, is one of the most important factors in its design. To determine this permeability the chosen tool is Darcy's law, which as mentioned by *Jones (1962)* can be expressed as:

$$K=\frac{Q*\mu*L}{A*\Delta P} \quad (2.26)$$

where, K is the permeability expressed in m^2; ΔP is the pressure drop before and after the section under study expressed in Pa; L is the length of the section or the test sample expressed in m; A is the cross sectional area of the flow expressed in m^2; μ is the dynamic viscosity of the fluid expressed in Pa*s and Q is the flow rate expressed in m^3/s. This law was discovered by its namesake Henry Philibert Gaspard Darcy in the 19th century with his famous experiment consisting on the flow of water through beds of sand as illustrated in Figure 2.3. These tests demonstrated the linear relation (the permeability) between the supplied flow rate and the pressure difference in a porous medium. Afterwards, this relation would be proven through the homogenization of the previously discussed Navier-Stokes equations.

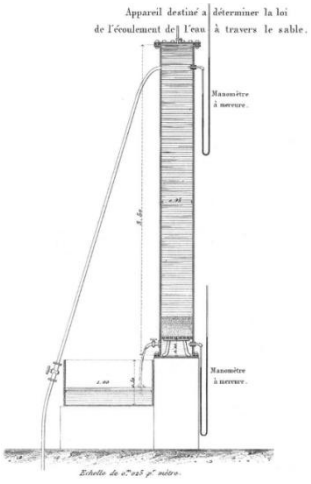

Figure 2.3. First bed of sand experimental setup for determining Darcy's law *(Darcy, 1856).*

This equation has been an essential tool in determining the permeability of porous mediums and recently it has been used to determine the permeability of scaffolds (these are treated as an analogous of a porous medium), such as in *Dias et al. (2012)* and *Mohee et al. (2019)*. However, Darcy's law can only be applied to laminar flow for a fluid with constant viscosity, which is why before applying this law we must determine the Reynolds number of the flow. The Reynolds number is a dimensionless parameter given by:

$$\mathrm{Re} = \frac{\rho * \mathbf{U} * \mathrm{D}}{\mu} \tag{2.27}$$

where ρ is the fluid density; $\mathbf{U}$ is the velocity of the fluid and D is the diameter of the pipe (or in the scaffolds case, the diameter of the pore). This variable determines the type of fluid flow, with the flow being laminar at lower Reynolds number and turbulent at higher numbers. *Ochoa et al. (2009)* and *Chor and Li (2006)* discussed how applying Darcy's law is only correct for a Reynolds number equal or lower than 1 with Re values up to 8.6 giving a insignificant variation. For analysing flow that present a Reynolds number higher than 8.6, it's preferable to the Forchheimer equation and the Ergun equation, both of which take into consideration the inertial forces present at those higher Reynolds numbers *(Chor and Li, 2006 and Orr and Burg, 2008)*.

Finally, another flaw of Darcy's law is its ineffectiveness in determining the permeability of a porous medium if the fluid is a non-Newtonian fluid. *Ali and Sen (2018)* concluded, after comparing the application of Darcy's law for both a Newtonian based model for blood and a non-Newtonian counterpart, that the law was ineffective for calculating permeability for non-Newtonian models. This means that although the law is perfectly suitable for more basic analyses, special consideration must be given not only to the Reynolds number of the fluid flow as well as the viscosity properties of the studied fluid.

Despite all of the limitations of Darcy's law, it was considered to be the best option to develop the present work.

2.4. CFD and FVM analysis

The earlier studies involving fluids dynamics were conducted with either mathematical calculations or experimental trials. However these methods pose several limitations, such as the increasing complexity and time requirement of the mathematical calculations and the necessity of several iterations in experimental trials (leading to a waste of time and material). With the advances in technology and computational capacity, a third alternative surfaced: numerical simulation, which in this field is known as computational fluid dynamics (CFD). CFD consists on modeling the flow of a fluid by numerically solving the Navier-Stokes equations (which would be too time-consuming to be solved analytically). This method allows for a faster calculation of numerous variables (such as

pressure, velocity and wall shear stress) in more intricate scenarios while it reduces the need for such a large number of experimental tests.

CFD analysis can be applied to a certain domain by using several techniques, like finite element method and the finite difference method, nonetheless the approach chosen for a majority of CFD analysis is the Finite Volume Method (FVM). FVM is described by *Moukalled et al. (2016)* as "*(...) a numerical technique that transforms the partial differential equations representing conservation laws over differential volumes into discrete algebraic equations over finite volumes*". In other words, FVM consists in a method that attempts to resolve the conservation laws by applying them over each volume and finding the solution for the resulting equations.

FVM can be split into three steps: creating the mesh; applying the equations and solving the system. The mesh is created by separating the 2D fluid domain into several small non-overlapping volumes with either a uniform grid system or, more commonly, a grid consisting of unstructured triangular elements (in the case of a 3D fluid domain these elements would be consistent hexahedral elements or unstructured tetrahedral elements). After the grid is completed, the partial differential equations are transformed into algebraic equations by integrating them over each of the generated discrete elements. Finally, the resulting complex system is solved by iterative processes, returning the values of the unknown variables for every one of the elements of the domain.

As a method for solving numerical fluid simulations, FVM presents two advantages over alternatives methods, namely it being strictly conservative and having an easier implementation of boundary conditions. In flow dynamics, the flux that exits from a given volume face must be equal to the flux entering the adjacent face and because FVM is based on volumes instead of elements, this makes it strictly conservative, making it preferable over the other methods. Besides this, all of the unknown variables are evaluated at the centroid of the volume, making it less invasive to insert constraints on the boundaries (when compared to the other methods).

Taking into account all of these considerations, for this work it was decided to implement a CFD analysis using a FVM method with constant hexahedral elements, with this choice of elements being explained in chapter 4.

3. State of the Art

Numerical analysis of the fluidic properties of scaffolds has been conducted since the 1990s. Since then, various innovative studies and techniques have been developed to better calculate the scaffold's properties and their possible applications. The permeability of a scaffold has been the focus of various studies. These studies utilise different permeability measuring systems, which were analysed to determine the one that best fits this work's objectives.

3.1. Permeability system

As previously mentioned, the key characteristic of scaffolds for the development of this work is their permeability. Thusly, a closer look into the different systems designed for measuring a scaffolds' permeability is required.

As described in *Pennella et al. (2013)*, the methods for evaluating a scaffolds' permeability can be divided into direct and indirect methods. A direct method is based on empirical measurements on the pressure drop or flow rate through the scaffold. Afterwards, Darcy's law is used to determine the permeability value. Indirect methods focus on measuring certain characteristics of the scaffolds, such as their porosity and pore size. These parameters are then applied to pre established formulas in order to obtain the permeability value *(Pennella et al., 2013)*. The problem with indirect methods is that their formulas require coefficients which are very hard to determine without resorting to empirical tests. Because of this, it is advisable the implementation of direct methods to establish the permeability of less studied scaffolds.

Direct methods can be further divided into two distinct types: gravity-based and pump-based methods. Gravity-based methods place the scaffold inside a vertical oriented chamber with water entering from the top and exiting the bottom. The principal behind these types of experimental systems is that gravity will force the fluid through the scaffold (assuming it's already saturated with said fluid) and that the difference in the flow rate will be dependent on the permeability of the scaffold. Gravity based systems can either follow the falling head or constant head method (Figure 3.1). In the falling head method the water is in a tube with the experiment consisting on measuring the drop in the level of the water and the time it takes for the water to drop. The constant head method has a reservoir on the top of the chamber with a constant level of water (normally maintained through a fluid inlet), and it functions by measuring the time it takes for a certain volume of water to pass through the system. Out of these two gravity-based systems, the constant head method is the more commonly used because it has a constant pressure drop as well as a constant flow rate. The constant head gravity-based permeability system has been used in studies such as *Mohee et al. (2019), Montazerian et al. (2017) and Dias et al. (2012)*.

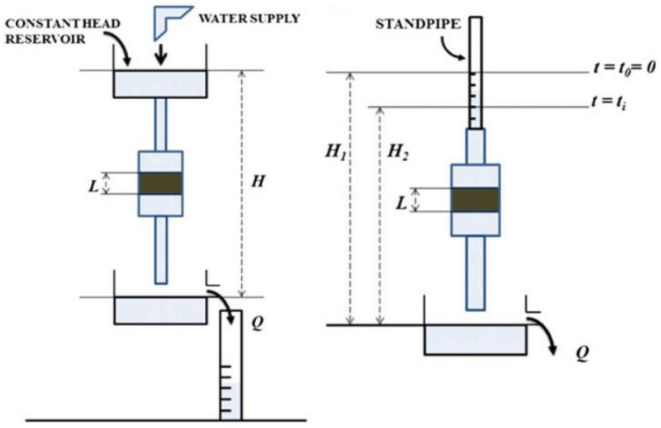

Figure 3.1. Representation of the constant-head gravity permeability system (left) and the falling head gravity permeability system (right) *(Pennella et al., 2013)*.

Pump-based methods also have the test scaffold inside a test chamber; however, in this system what is measured is the pressure difference before and after the scaffold instead of the flow rate. This pressure drop is then used to determine the permeability using Darcy's law. The basis behind this method is a pump that applies a constant flow rate through the scaffold resulting in a pressure drop at the ends of the chamber which is picked up by a sensor. This measured pressure drop is influenced not only the scaffold inside the chamber but also by the cross-sectional variations across the system. Taking this into consideration, another set of measurements for an empty chamber must be conducted in order to obtain the actual pressure drop using the following expression:

$$\Delta P_{scaffold} = \Delta P_{measured} - \Delta P_{empty} \tag{3.1}$$

Similar to the gravity-based method, the pump-based method can also be divided into two distinct categories according to the chosen pump: peristaltic pump (Figure 3.2) or syringe pump (Figure 3.3). The system with a peristaltic pump provides an endless supply of fluid at a constant flow rate to the scaffold. However, because of the nature of the peristaltic pump, it requires a fluid flow damper in order to minimize the pressure variation caused by the peristaltic pulse inherent to the pump. The alternative to the peristaltic pump is a syringe pump, where a syringe filled with fluid, which then pumps a predefined volume of said fluid, at a constant flow rate through the system. This results in measurements which are not influenced by the peristaltic pulse but have a limited time in which to obtain these measurements. Both of the pump-based methods have been used in studies determining the permeability of scaffolds for TE such as *Truscello et al. (2012)* and *Ochoa et al. (2009)* for the peristaltic pump and *Mohee et al. (2019)* and *Castro et al. (2019)* for the syringe pump.

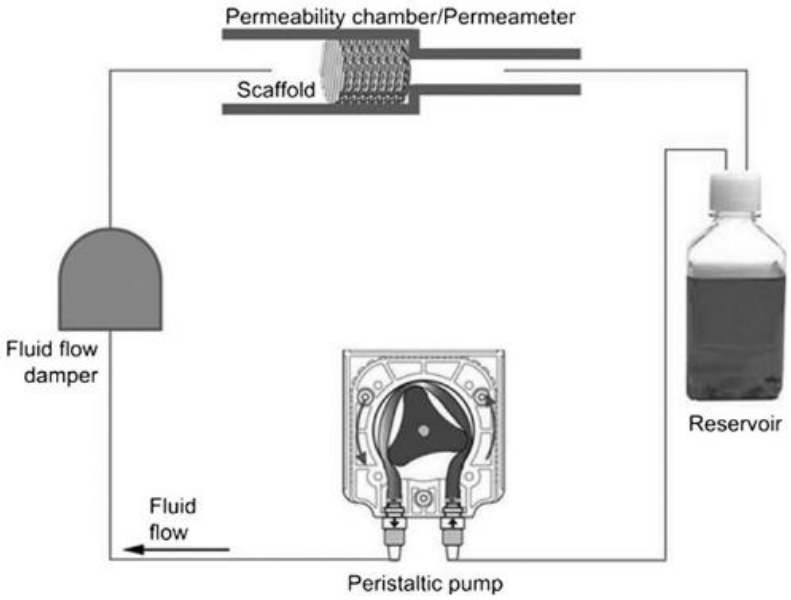

Figure 3.2. Representation of the peristaltic pump permeability system *(Pennella et al., 2013)*.

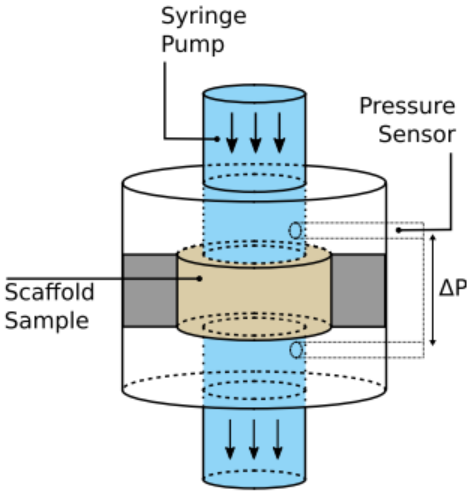

Figure 3.3. Representation of the syringe pump permeability system *(Mohee et al., 2019)*.

3.2. Numerical Modeling

One of the first studies that attempted to calculate permeability through a numerical process was *Pillai and Advani (1995)*. The objective of this study was to find the permeability of a fibrous porous medium by using a CFD analysis followed by the application of Darcy's law. Despite this study being focused on fibrous porous mediums instead of scaffolds, it proved how a numerical analysis could be useful in several areas when investigating the permeability of different structures.

Moving forward one of the earlier investigations to apply a numerical analysis to the analysis of scaffold geometry was *Jung and Torquato (2005)*. This study calculated the permeability of six different 50% porous TPMS geometries, by resolving the Navier-Stokes and continuity equations thorough homogenization methods. Their findings showed that, although the specific surface of a given geometry is not necessarily connected to its permeability value, they were related because of the fact the pore spaces are normally connected in TPMS geometries (which presented the higher permeability values). Therefore, it was determined that a higher specific surface of geometry indirectly indicates a lower permeability. Although this was not the first study to apply a numerical method to investigate scaffolds, this was one of the first to consider similar TPMS geometries to the ones studied in this work.

Another study that implemented homogenization methods in order to determine the permeability of a scaffold was *Dias et al. (2012)*, in which the calculated permeability was compared to ones obtained experimentally. The computational results were obtained through a mathematical approach based on both Darcy's law and the homogenization method. These methods were applied to a porous periodic media as illustrated on Figure 3.4. For the experimental component of the study, a constant-head gravity based permeability measurement system was chosen. In both the computational and experimental components, several scaffolds were designed with different geometries, porosities and pore sizes to determine how each of these characteristics affects the scaffolds permeability. Their findings reveal that each of the studies' parameters had an effect on the permeability, meaning that a scaffold's permeability is not only determined by a single factor, but is instead a single measurement that already encompasses a scaffold's porosity, pore size and geometry.

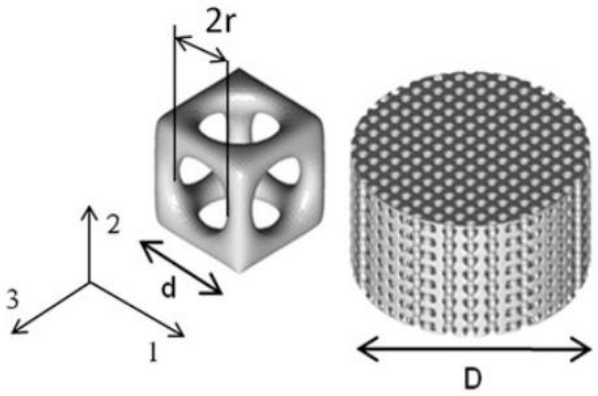

Figure 3.4. Representation of the unitary cell (left) and cylindrical scaffold design (right) used by *Dias et al. (2012)*.

Following these studies, more research was conducted using similar numerical processes to determine a scaffold's permeability. However, some of these studies found some limitations in the underlining process such as *Marin and Lacroix (2015)*. This study focused on the physical limitations of scaffold production, namely the variability inherent to the manufacturing and how this affects the fluidic properties. The study focused on five different physical scaffolds with the same geometry, by comparing numerical results of the original Computer-Aided Design (CAD) with µ-CT reconstructions

of each scaffold. The CFD analyses were conducted on geometries that included the scaffold inside a cylindrical chamber. For the simulation, the geometry was meshed using tetrahedral shapes and the simulation parameters were defined with a fluid density of 1000 kg/m^3 and viscosity of 0.001 kg/(m.s) (the constants for water); an outlet pressure of 0 Pa, a no slip wall condition and an inlet velocity of 1 mm/s. Besides the inlet flow rate/velocity (dependent of the study), the remaining established parameters are the ones used in almost all CFD analyses in order to determine the pressure drop between the inlet and outlet, by using the previously discussed continuity and Navier-Stokes equations alongside Darcy's law. The outcome revealed a clear distinction in the characteristics of the CAD and each scaffold. Furthermore, there were different results between each scaffold. This highlights how slight alterations during the manufacturing of a scaffold might considerably alter its properties. The simulation parameters discussed for this research were chosen for the present work.

Besides the manufacturing process, other possible limitation in the study of a scaffold's permeability is the usage of Darcy's law. *Rahbari et al. (2016)* highlighted some of the limitations regarding this law. *Rahbari et al. (2016)* conducted a study concerning the permeability of potential TE scaffolds. These scaffolds were cylindrical and each of their unitary cells possessed a simple design consisting of a solid cube with three cylinders in the center of each face subtracted (Figure 3.5). This study utilised the previously discussed the parameters *Marin and Lacroix (2015),* with varying inlet flow rates. *Rahbari et al. (2016)* showed that the highest velocities in the scaffold were present in the passages parallel to the flow. It was also shown that turbulent flow was more common on the passages parallel to the flow at the lower porosities. Furthermore, it was determined that a lower inlet flow rate caused an increase of the permeability coefficient, especially at the higher porosities. However, there were some notable differences between the numerical and experimental results. *Rahbari et al. (2016)* established that these discrepancies stemmed from two factors: the fact that at lower porosities the flow starts to exhibit turbulent flow at certain velocities (making the implementation of Darcy's law less ideal) and that these numerical simulations often overlook the material's wettability and roughness. These are factors to take into consideration when designing future numerical tests.

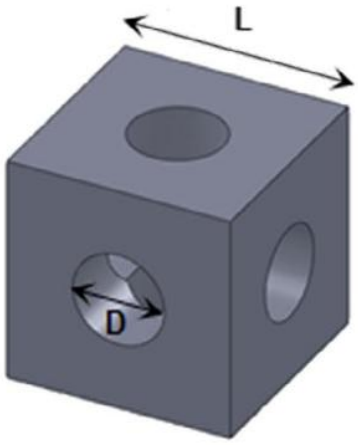

Figure 3.5. Unitary cells for the scaffold design in *Rahbari et al. (2016)*.

A topic for CFD scaffold analysis that has been getting more attention in recent years is cell seeding inside the scaffolds, which is, in the end, one of the major goals of its design. Some studies that looked into cell seeding were *Marin et al. (2017a, 2017b)*. *Marin et al. (2017a)* created a multiphase CFD model alongside particle tracking velocimetry (PTV) experiments in order to understand the relation between fluid flow and cell transport. The comparison between the experimental and numerical analysis would allow for a more in depth understanding on how different conditions, such as velocity and scaffold geometry, influence where the cells travel, and more importantly, where they could possibly be deposited inside the scaffold. For the numerical analysis, the fluid was represented with the same parameters as the previously discussed studies, with a time-dependent inlet flow rate: 0.3 ml/min for the first 10 s that would then change periodically between 0.05 to 0.09 ml/min every 0.125 s for 5s. These flow parameters were chosen in order to simulate the conditions of a bioreactor, instead of a bone implant situation. The cells were modeled as inert microsphere particles with a 0.01 mm diameter. The results of the study showed that the cells would normally follow the fluid streamlines, which were determined to be dependent on the inlet velocity. Furthermore, it was also establish that, in order to overcome the gravity forces, it was required to have higher flow rates. However, this increase also resulted in an increase in the drag forces affecting the cells. Despite this, the majority of the cells would never contact the scaffold because they would either be lost because of sedimentation (gravity forces would stop the cells before reaching the scaffold) or they would pass through the scaffold without interacting with it. This study highlights the importance of understanding how the cells travel inside a scaffold and the analysis of the streamlines of the fluid flow in order to be able to better judge the effectiveness of future scaffold designs.

Marin et al. (2017b) focuses on understanding the interactions of cells and scaffold walls in a bioreactor environment, through both experimental tests as well as CFD simulations. The experimental and computational setup are represented in Figure 3.6, with a syringe connected to the inlet and another connected to the outlet, generating an alternate flow (alternating after 0.5 ml of dispensed fluid in order to make the cells pass through the scaffold multiple times), which is known as dynamic seeding. A set of tests with a single non-alternating flow were implemented for comparison (static seeding). Furthermore, for the inlet flow rate, three different ones were chosen as a means to understand how they influence the deposition: 0.012, 0.12 and 0.6 ml/min (these flow rates correspond to velocities at the scaffold entrance of 0.1, 1 and 5 mm/s, respectively). Additionally, the computational component also considered gravity, with a set of tests with this variable and another set without. The results from *Marin et al. (2017b)* revealed that, in most cases, there was a heterogeneous distribution of cells for the static seeding, rendering this type unsuitable for clinical applications. In the dynamic seeding, without the presence of gravity (as seen in *Marin et al. (2017a)*), the cells would follow the streamlines, strengthening the argument that scaffolds design must maximize the interaction between these streamlines and the scaffold walls. The dynamic seeding results without gravity also showed how higher flow rates would result in more streamlines, and thus cells, impacting and interacting with the scaffold walls. However, at a certain velocity, the flow rate would begin to cause the appearances of vortexes, leading to cells being trapped inside them. As for dynamic seeding with the effect of gravity, the experiments reveal that at low fluid velocities, gravity

would cause a very poor transport of cells through the scaffold. This indicates a need to moderate between the effects of fluid velocity and gravity. In the end, *Marin et al. (2017b)* found that the chosen scaffold, with their designed perfusion system, had a poor performance, highlighting the need for new approaches to enable better cell-scaffold wall interactions, such as new scaffold geometry or new perfusion systems. *Marin et al. (2017a, 2017b)* are proof of the importance of the flow streamline when attempting to design scaffolds for a TE application. Considering what these studies have underlined relative to the importance of the fluid streamlines, regarding the cell-scaffold interaction, they are a key component of the present work. In this sense, a study of the scaffolds streamlines will be conducted to better evaluate their viability.

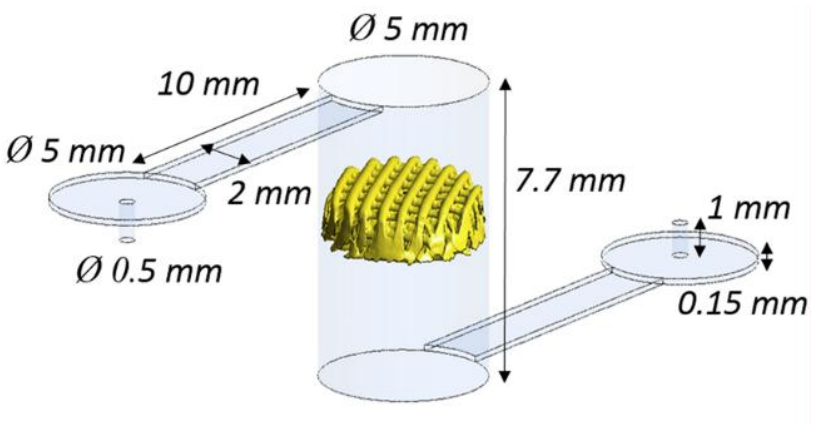

Figure 3.6. Experimental setup for the cell deposition tests (*Marin et al., 2017b)*.

Another research that also studied the permeability of different scaffolds, through numerical methods, was *Montazerian et al. (2017).* This study analysed the permeability of different lattice and TPMS scaffolds. This research analysed these scaffolds in regards to their longitudinal permeability as well as introducing the concept of the radial permeability as a possible additional factor in the design and fabrication of scaffolds. To this end *Montazerian et al., (2017)* created cylindrical scaffolds of each of their chosen geometries in a CAD program and submitted them to the previously mentioned conditions with an inlet velocity of 10^{-6} m/s. To support their numerical findings, an experimental test setup was devised following a gravity based constant-head permeability test. Their results demonstrate how TPMS geometries were overall much more permeable than the lattice geometries of equal porosity, namely at much lower porosity percentages, as seen in Figure 3.7. Regarding the radial permeability component of the study, it was only conducted on the lattice scaffolds and it showed that the results were comparable to the longitudinal permeability as seen in Figure 3.8, highlighting this parameter's possible relevance in future scaffold design and research. Their results also present a comparison of the permeability of different TPMS scaffolds for different porosity (although not analysing or discussing the reasons behind this), making a valuable point of comparison for this work.

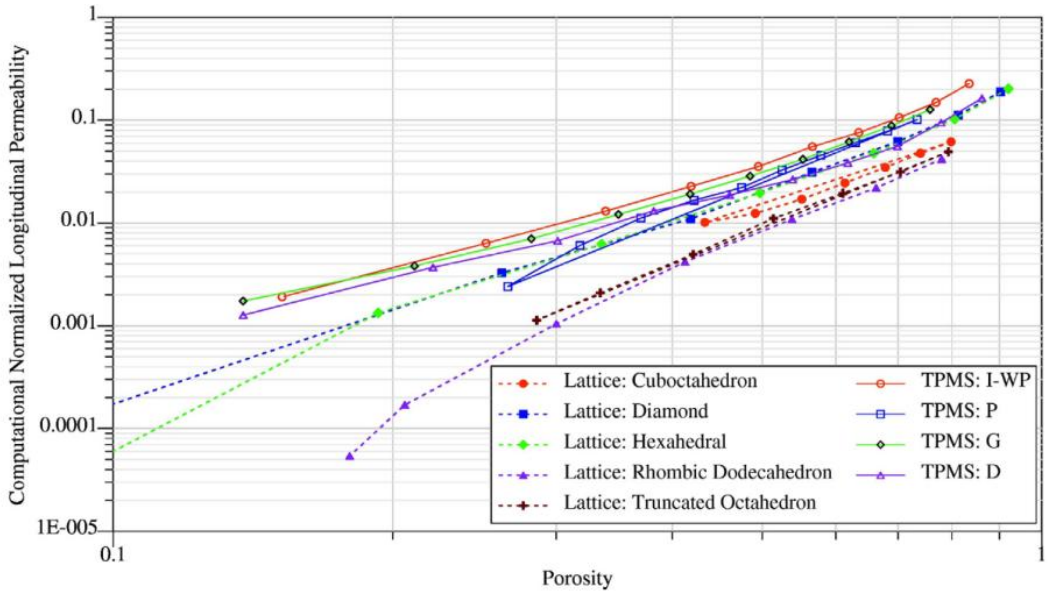

Figure 3.7. Variation of computational normalized longitudinal permeability versus porosity for 5 lattice based and 4 TPMS based geometries *(Montazerian et al., 2017)*.

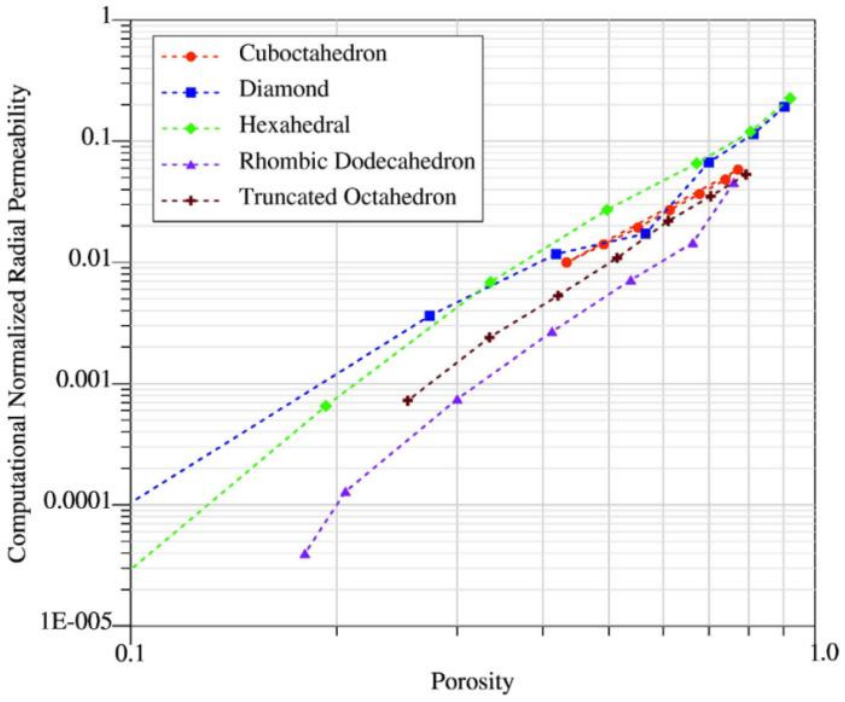

Figure 3.8. Variation of computational normalized radial permeability versus porosity for the 5 lattice based geometries *(Montazerian et al., 2017)*.

Finally, another study that uncovered some limitations with Darcy's law was *Ali and Sen (2018)*. This study conducted research into lattice based and TPMS gyroid based geometry, however, instead of looking solely at the scaffolds' permeability, they analysed it as well as the wall shear stress (WSS) of both Newtonian and non-Newtonian models. The main objective of *Ali and Sen (2018)* was evaluating an often overlook and oversimplified aspect of scaffold design, that is the blood passing through the

scaffolds. To simplify the required CFD calculations, blood is normally considered as being a Newtonian fluid with a constant viscosity; however, certain components of the blood, such as cells and proteins, cause it to have a non-Newtonian nature. In this study, the fluid was expressed with either a constant viscosity of 0.004 kg/m.s for the Newtonian model (higher than other studies, because it focuses on the study of blood instead of water) or a viscosity calculated based on a power law approach for the non-Newtonian model. For the inlet boundary condition, *Ali and Sen (2018)* considered a flow rate of 60 ml/min that corresponds to an inlet velocity of approximately 0.7 mm/s. The results from the numerical simulation showed that the velocities inside the scaffolds and pressure drop of said scaffolds were both significantly higher in the non-Newtonian model (Figure 3.9 and Figure 3.10). However, there were no significant changes in their velocity profiles (Figure 3.9), meaning that the velocity profile was proportionally identical in both models. This fact reveals how the behaviour of the fluid inside the scaffolds is determined not by the chosen viscosity model but by the chosen scaffold geometry and inlet velocity. The higher velocities and measured pressure drops for the non-Newtonian model shows that model causes a much higher flow resistance and this, alongside the extreme difference observed in Figure 3.10, raises some possible limitations regarding the effectiveness of Darcy's law for non-Newtonian models.

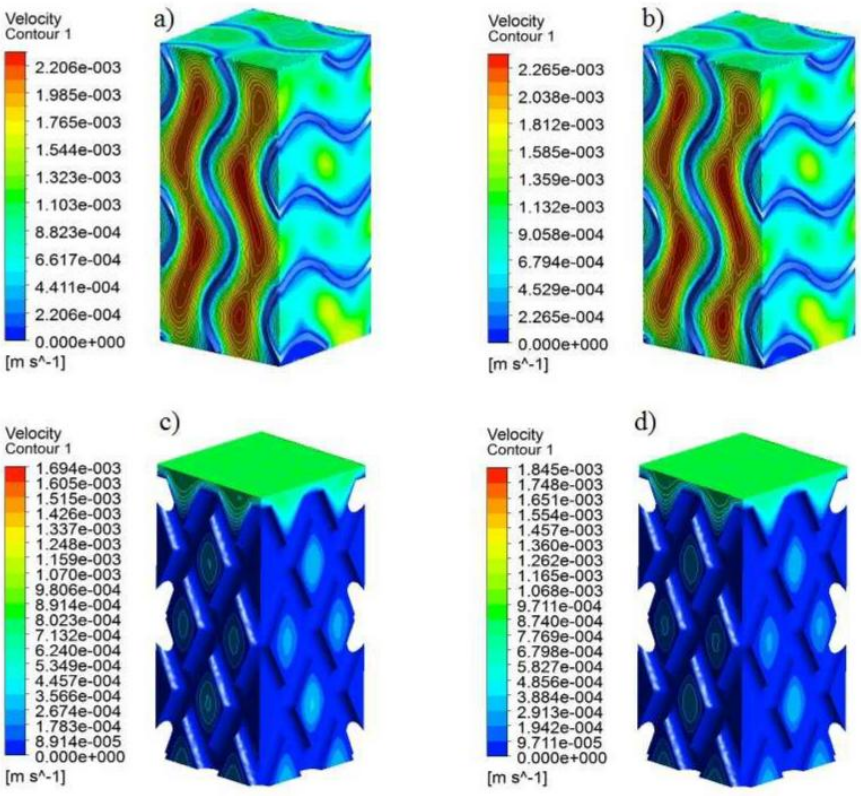

Figure 3.9. Velocity contours for Newtonian models on the left and the equivalent non-Newtonian models on the right*(Ali and Sen, 2018)*.

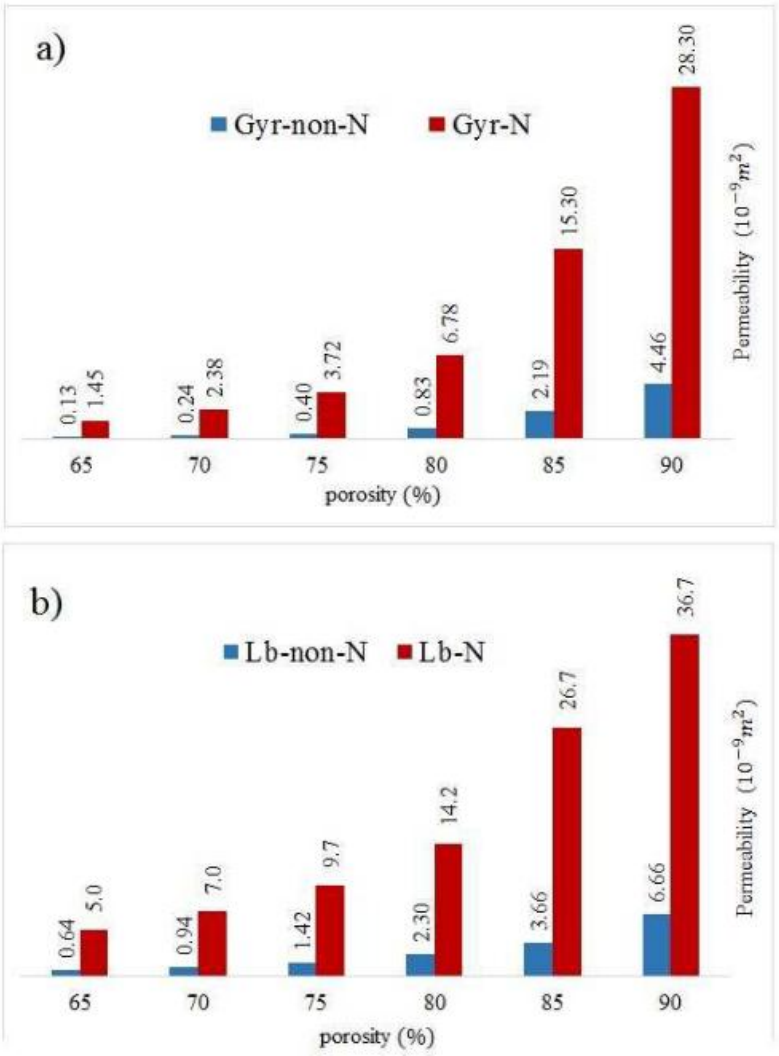

Figure 3.10. Comparison of the calculated permeability for Newtonian and non-Newtonian models *(Ali and Sen, 2018)*.

4. Methodology

In this chapter there will a discussion about this work's computational setup as well as the choices made regarding the meshing of the geometry and the implementation of the simulation parameters. It will also contain a clarification of the software that was required to create the different computer models used in the CFD analysis.

4.1. Model geometry

4.1.1. Model shape and dimensions

The computational model was based on the experimental setup used in *Castro et al. (2019)*. The main component to represent in the numerical analysis was the permeability chamber, more specifically, the inside of the chamber (as a CFD analysis simulates only the fluid phase and not the actual chamber). All of the components of the permeability chamber are represented in Figure 4.1a), with the dimensions of the inside of the chamber (the fluid phase of the simulation) represented in Figure 4.1b). There also existed two springs than maintained the scaffolds and the discs in the center of the permeability chamber. However, *Almeida, (2015)* verified that for this experimental setup, the springs did not affect the end result.

The dimensions of the discs that hold the scaffold inside the chamber are represented in Figure 4.1c), with the total length of the three parts together being 20 mm. Finally the lids that are attached at the inlet and outlet of the chamber are represented in Figure 4.2. Because of the portion of the lids that goes into the chamber, the actual total length of the simulated chamber is 77 mm and not the previously established 97 mm. This setup only allows for the testing of cubic, 13 mm sided scaffolds, meaning that all design must be subjected to this constraint.

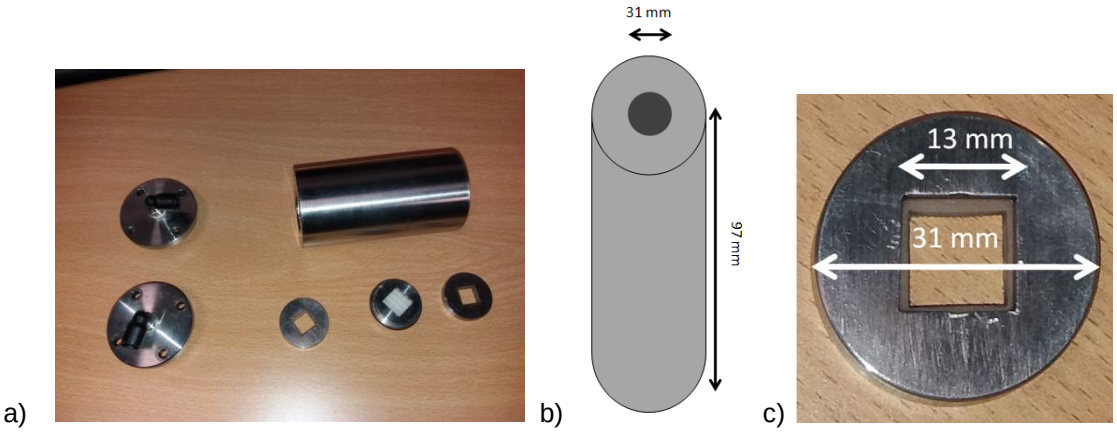

Figure 4.1. a) Image of all of the components of the permeability chamber; b) representation of the main permeability chamber and its dimensions and c) dimensions of the cover of the permeability chamber (to keep the scaffold inside the chamber).

Figure 4.2. Image of the lid of the permeability chamber (left) and its respective representation with its most relevant dimensions (right).

However, this configuration results in a large amount of space in the cylinders that is irrelevant for the numerical simulation. Therefore, it was decided to model the chamber with a smaller transversal squared area with 13 mm sides, as a way to the reduce the computational weigh of the simulations. This new model was a chamber with a squared cross section with 13 x 13 mm and the same total length of 77 mm.

This new chamber should, theoretically, wield the same results, seeing as the permeability of a scaffold is not dependent on the experimental setup. Furthermore, any differences should be corrected by measuring the pressure drop on an empty chamber and applying this to equation 3.1. In the end, this results in a chamber with the dimension illustrated in Figure 4.3.

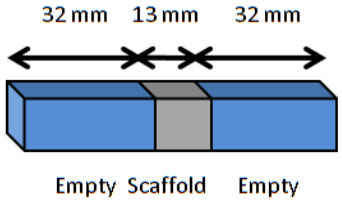

Figure 4.3. Representation of the CFD chamber with its dimensions.

4.1.2. Meshing

For creating the mesh of the scaffolds, the program previously mentioned in chapter 2.2.3., developed by *Dinis et al. (2014)* was used. The program returns .inp files, which are the input files for the ABAQUS ® software (Dassault Systemes Simulia Corp., Providence, Rhode Island, USA). These files represent the unitary cell of both the scaffold and the fluid phase with a cubic hexahedral mesh. The number of elements per side for a unitary cube is a required parameter of the software and it was determined that a minimum of forty elements per side was required to obtain a valid scaffold from a 3D printing process, namely through the MJD process. Therefore, it was decided to maintain the same number of elements in the numerical simulation as it would be required in an experimental setup. As for the configuration of the final scaffold, it was decided to be a 4 x 4 x 4 cubic scaffold with a 13 mm side (meaning each unitary cubic cell is a 3.25 mm sided cube and the mesh is constituted

by 0.08125 mm side cubes), in order to follow the scaffold shape tested in *Castro et al. (2019)*. For this work, three different TPMS geometries were considered (SP, SD and SG) with four different levels of porosity for each of them (50%, 60%, 70% and 80% porosity). This results in a total of twelve distinct scaffolds that will be henceforth be referred to by their geometry and porosity, for example, a SP scaffold with 70% porosity will be called SP70.

Having obtained a singular unitary cell with both phases (scaffold and fluid), a Matlab ® (MathWorks Inc., Natick, Massachusetts, USA) program was created that isolated the desired phase (in this case, the fluid phase), removing all of the nodes and elements of the mesh not being utilised. Afterwards, the program multiplies the fluidic unitary cell and combines them into the desired 4 x 4 x 4 shape. Finally, it attaches an empty chamber, before and after the scaffold, to simulate the permeability chamber. In order to maintain consistency through the simulation, the empty chambers were also mesh using 0.08125 mm sided cubes. An example of a finished mesh for a unitary cell can be seen in Figure 4.4. Finally, an entire empty chamber (13 x 13 x 77 mm) with an equivalent mesh had to be designed and analysed in order to obtain ΔP_{empty} for expression 3.1.

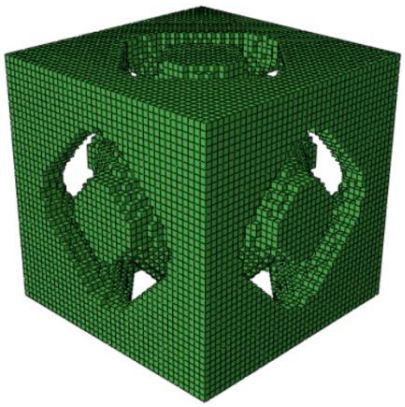

Figure 4.4. Mesh of a single unitary cell for a SP70.

4.2. Numerical models

After completing the program for generating the scaffold's meshes, it was determined that the establish mesh parameters made it impossible to run the numerical analysis with the entire chamber and scaffold. A complete model would be made out of approximately 24 million elements (even when considering the simplified chamber) and the hardware was unable to run the model. Therefore, three alternative models were designed, which were the periodic model, the symmetric model and the simplified model. These models assume the fluid is flowing in the z direction, on a xyz coordinate system.

4.2.1. Periodic model

The first alternative model to be designed was one that took advantage of the nature of the TPMS geometry, namely the fact that it's periodic. This new models assumed the scaffold being tested did not have a 4 x 4 x 4 configuration, but instead had an infinite amount of unitary cells in both directions perpendicular to the fluid flow (x and y). This would make it possible to model a simpler scaffold and chamber with 1/16 of the number of elements (Figure 4.5), with approximately 1.5 million elements (Table 4.1). These models ignore the effects of the walls of the chamber and focuses on determining the permeability of four cell deep scaffold. The main problem with these models is precisely the fact that, ignoring the effect of the chamber walls, will always wield a considerable higher permeability value than what would be observed in an experimental setup.

Figure 4.5. SP70 scaffold with a 1x1x4 configuration with the chamber attached.

Table 4.1. Number of nodes and elements for each periodic scaffold model with the chambers.

Model	Nodes	Elements
SP50	1,551,696	1,453,812
SP60	1,577,736	1,477,780
SP70	1,607,588	1,505,364
SP80	1,633,628	1,530,164
SG50	1,548,773	1,444,768
SG60	1,578,839	1,472,160
SG70	1,606,231	1,497,588
SG80	1,634,715	1,524,264
SD50	1,555,773	1,444,456
SD60	1,583,955	1,469,836
SD70	1,613,899	1,497,264
SD80	1,640,233	1,521,904

For the implementation of this periodic model, a periodic boundary condition of FLUENT ® ANSYS ® (Ansys Inc.,Canonsburg, Pennsylvania, USA) was chosen (further explained in the next chapter). However, this condition requires that two boundaries with an equal shape are chosen, which could only be done in the SP scaffolds. To overcome this problem, a Matlab routine was created, designed

to cut all the elements along the edge of the model in half, extract the outer half and place it on the opposite side of the model (Figure 4.6). This routine would guaranty that both sides have a boundary with the same shape. This program was applied on both the xz oriented faces and the yz oriented faces. The fact that the new edges of the models no longer accurately represent the edges of a real scaffold is not an important factor, because the goal of this model is to simulate an infinite repeating structure and not a real one. Furthermore, moving half a row of elements from one side to another would not affect the results because the structure has no limits (walls) in either x or y direction.

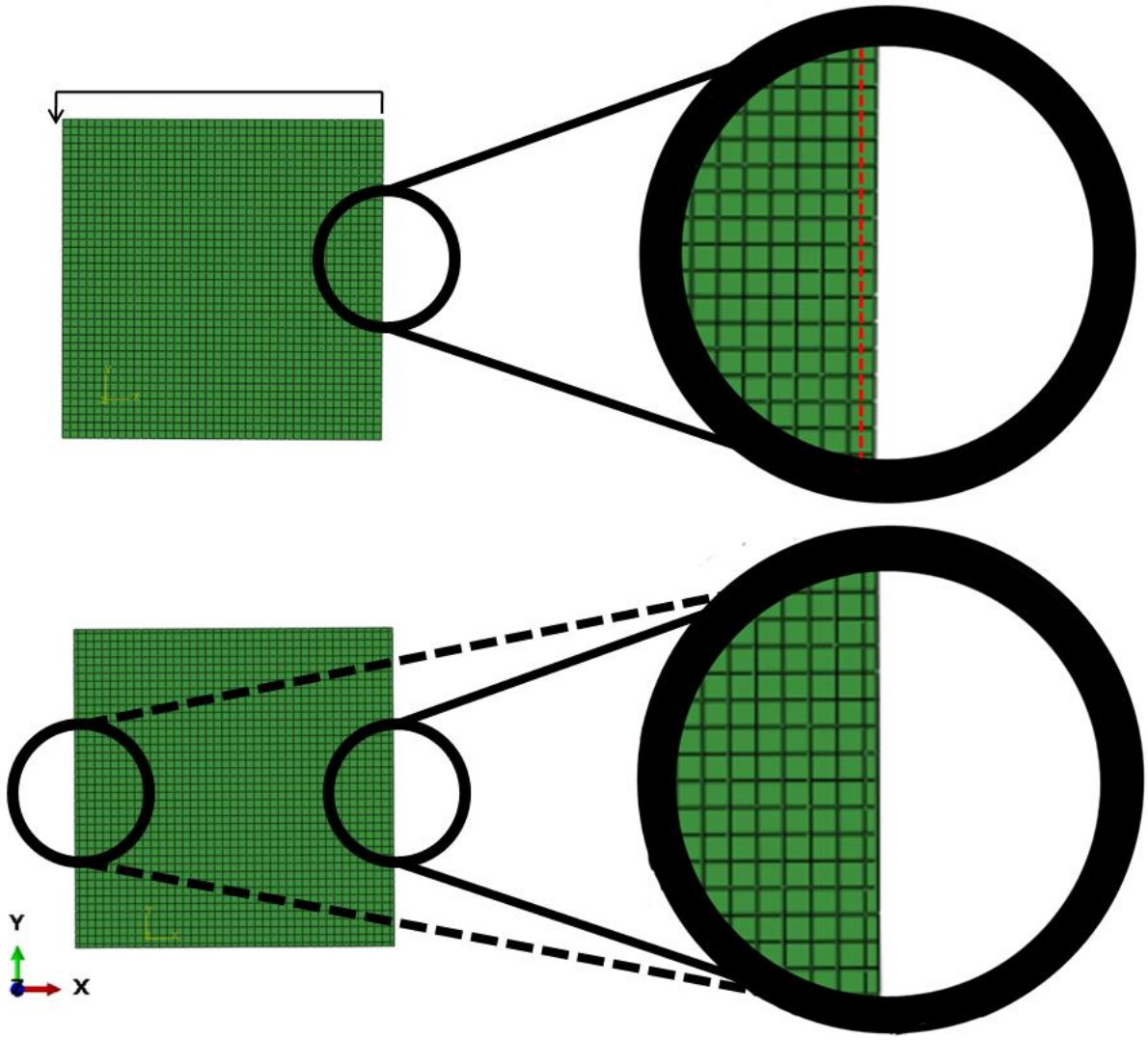

Figure 4.6. Illustration of the Matlab routine on both planes. Scaffold with the chamber before the routine (top) and after the routine (bottom) viewed on the xy plane.

4.2.2. Symmetric model

Another alternative considered model was a model with two symmetry axis running through the middle of the chamber in the xz and yz orientation. However, contrary to the periodic model, this model is only valid if two conditions are met: the geometry has to have two symmetry axes in its

middle and the fluid flow cannot pass through the symmetry axis. The second condition cannot be determined without first running the simulations, guarantying the fluid does not pass the boundary, thus validating this condition. However, the first condition can be validated *apriori*, only being valid for SP geometries, seeing as the other two do not possess any symmetry axes. Although TPMS geometries are necessarily periodic this does not mean they are necessarily symmetric.

The created geometry, considering only a quarter of the total model, possessed approximately 6 million elements (Table 4.2) and the scaffold had a 2 x 2 x 4 configuration (Figure 4.7). The FLUENT ANSYS's symmetric boundary condition was chosen (will also be further explored in the next chapter).

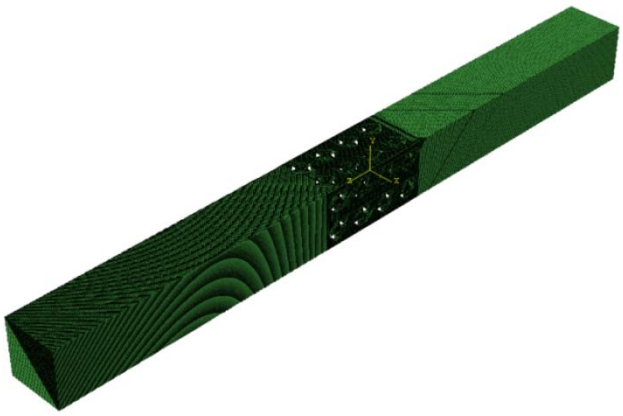

Figure 4.7. SP70 scaffold with a 2x2x4 configuration with the chamber attached.

Table 4.2. Number of nodes and elements for each symmetric scaffold model with the chambers.

Model	Nodes	Elements
SP50	5,765,637	5,529,856
SP60	5,863,397	5,621,376
SP70	5,975,701	5,727,104
SP80	6,074,101	5,822,336

4.2.3. Simplified model

The last alternative model that was designed was a simplified model with twenty elements per unitary cell instead of forty. This model goes against the condition established in the beginning of having a minimum of forty elements per unitary cell; however, because of the large number of total elements of the original chamber, out of the three considered models, this is the method that allows the entire chamber to be represented.

Half of the number of elements per side will result in a decrease of the geometry's accuracy and might influence the pressure difference observe at the ends of the chamber. However, half the elements per side will also result in 1/8 the total number of elements of the mesh, meaning a total number of elements of around 3 million (Table 4.3). Finally, because there are no alterations to the number of

unitary cells being studied, the scaffold will have the complete 4 x 4 x 4 configuration (Figure 4.8) and will have no requirements for any additional boundary conditions (other than the standard ones explained in the next chapter).

To obtain this new geometry, the steps described in chapter 4.1.2. were repeated, with twenty elements instead of forty for each unitary cell side. Furthermore, because of the fewer number of elements, the length of side the hexahedral elements for both the scaffolds and the chambers were 0.1625 mm instead of the previously discussed 0.08125 mm.

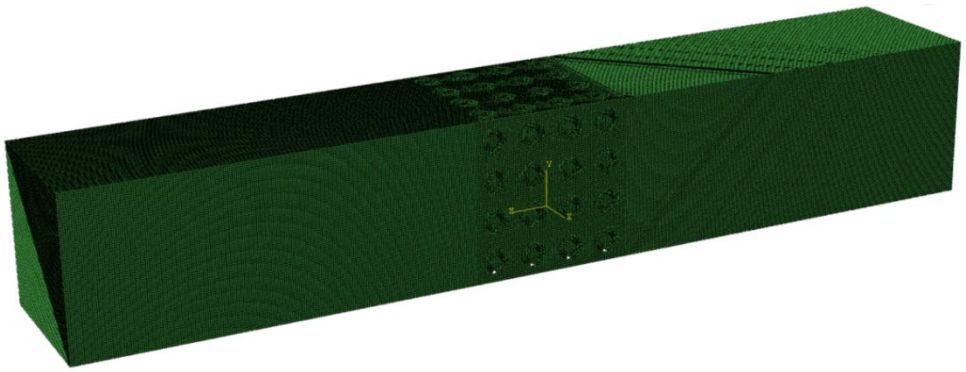

Figure 4.8. Simplified SP70 scaffold with a 4x4x4 configuration with the chamber attached.

Table 4.3. Number of nodes and elements for each simplified scaffold model with the chambers.

Model	Nodes	Elements
SP50	2,919,483	2,756,096
SP60	2,972,411	2,800,640
SP70	3,020,219	2,847,232
SP80	3,071,355	2,894,848
SG50	2,916,633	2,727,552
SG60	2,969,321	2,774,784
SG70	3,023,009	2,824,064
SG80	3,075,577	2,872,832
SD50	2,926,089	2,713,984
SD60	2,985,889	2,764,672
SD70	3,039,641	2,812,288
SD80	3,090,289	2,861,952

4.3. Simulation Parameters

Having created the geometry and respective mesh of each scaffold, the chosen software for conducting the CFD analysis was the 16.2 ANSYS FLUENT Solver. This commercial program consists on a FVM with the application of iterative methods to solve the previously discussed Navier-Stokes equations.

This CFD solver has already been proven its effectiveness in scaffold analysis such as described *by Ali and Sen (2018)* and *Marin and Lacroix (2015)*. Furthermore, FLUENT has been proven to be

appropriate for analysing the same permeability system being used in this work *(Almeida, 2015)*, as well as analysing scaffolds of similar complexity *(Marques, 2013)*.

To import the geometry and mesh from the ABAQUS file into the CFD program, the program Finite Element Modeler (a component of ANSYS) was used, which allows the categorization of specific surfaces of the geometry as the inlets, outlets, walls and boundary conditions of the numerical analysis.

Before studying which are the optimal parameters to solve the FVM, certain assumptions were made in order to simplify the calculations. One of these assumptions was that, as discussed in Chapter 2.3., the fluid passing through the scaffold is an incompressible Newtonian fluid. Furthermore, the flow of said fluid was assumed to be a steady-state laminar flow (that is, a non-turbulent flow that is time independent with no accumulation of fluid, meaning a constant inflow and outflow), similar conditions as were established by *Marin and Lacroix (2015)* and *Dias et al. (2012)*. Finally, because this work focuses more of the passage of fluid through the scaffold, neglecting any minor alterations to the scaffold itself, the walls of said scaffold were assumed to suffer no deformation and the scaffold-fluid interface was assumed to have a no slip condition.

Having established these characteristics of the fluid, the remaining parameters to determine were the several possible solver parameters. To understand and find the preferable option for each parameter, the ANSYS FLUENT 16.2 User's Guide was essential. The main parameters to define were the boundary conditions.

Boundary conditions determine the portions of the geometry where the flow can enter, where the flow can exit, where the walls of the structure are (as well as their properties) and other possibilities. For the conducted simulations, three conditions were always utilized, those being velocity-inlet, pressure-outlet and wall boundary. Velocity-inlet indicates surfaces where the fluid is entering and what is its velocity. In these simulations, this velocity was determined based on the mass flow rate of each specific simulation and the area of the inlet (with the mass flow rate being equal to the velocity divided by the area). The pressure-outlet defines the surface where the fluid would exit and the pressure at that surface. For this work, said pressure was 0 Pa, so that the pressure drop of the permeability chamber would be equal to the pressure at the inlet (since the pressure drop is pressure at the inlet minus the pressure at the outlet). Finally the wall boundary conditions define the walls of the scaffolds and the permeability chamber, being defined with a no slip boundary condition. All of these parameters are equal to the standard parameters discussed in chapter 3.2. Besides these standard boundary conditions, two additional ones implemented were the symmetry boundary condition (assumes the structure repeats itself along the selected surface and that no flow passes that surface from one side to the other) and the periodic boundary condition (assumes an infinitely repeating structure with the repetition occurring along the two selected parallel planes with an equal shape).

Besides the boundary conditions, there were also considered other parameters for the simulation, which are attached in the appendix.

5. Results

Having discussed the fundamentals behind TE, described the most relevant studies regarding scaffold numerical simulations and established the steps taken to obtain the results, this chapter will focus on presenting said results. These results are the measured pressure drop and the resulting permeability of all three alternative models for each of the twelve tested scaffolds (or four in the case of the symmetric model). Afterwards these results will be compared among themselves and a selection of them will be compared with results obtained in an experimental setup (although these experimental trials are not the focus of this work, since they are being conducting in a parallel research with our contribution, they will be used as a point of comparison). Finally, the fluid streamlines obtained in the CFD models will be analysed in an attempt to understand the differences observed in the permeability measurements, as well as to determine how the cells would interact with each of the twelve scaffold geometries.

For all of the models, a total of eleven different inlet flow rates were studied between 1 and 100 ml/min. The velocities used on the numerical program were calculated based on the corresponding inlet flow rates (in m^3/s) and the constant cross sectional area of 0.000169 m^2 (Table 5.1). Finally, the conversion from pressure drop was made using Darcy's law with a length of 0.013 m, the mentioned area of 0.000169 m^2 and a dynamic viscosity of 0.001 Pa.s.

Table 5.1. Conversion of the inlet flow rate to the numerical simulation's inlet velocity.

Flow rate (ml/min)	Flow Rate (m^3/s)	Velocity (m/s)
1	$1.6667 * 10^{-8}$	$9.86 * 10^{-5}$
2	$3.3333 * 10^{-8}$	$1.97 * 10^{-4}$
3	$5.0000 * 10^{-8}$	$2.96 * 10^{-4}$
4	$6.6667 * 10^{-8}$	$3.94 * 10^{-4}$
5	$8.3333 * 10^{-8}$	$4.93 * 10^{-4}$
10	$1.6667 * 10^{-7}$	$9.86 * 10^{-4}$
20	$3.3333 * 10^{-7}$	$1.97 * 10^{-3}$
40	$6.6667 * 10^{-7}$	$3.94 * 10^{-3}$
60	$1.0000 * 10^{-6}$	$5.92 * 10^{-3}$
80	$1.3333 * 10^{-6}$	$7.89 * 10^{-3}$
100	$1.6667 * 10^{-6}$	$9.86 * 10^{-3}$

5.1. Symmetric models

As mentioned before, the symmetric model assumed two symmetrical axis in the middle of the scaffold. However, before measuring the pressure drop of any symmetric scaffold, the first step was verifying the previously discussed criteria for applying the symmetry boundary, namely guarantying that no flow goes through the symmetry plane. In order to determine whether any flow passes from one unitary cell to another (in either the x or y direction), the streamlines of a SP70 scaffold were studied (Figure 5.1). The streamlines revealed that no flow crosses from one half of the scaffold to the other (separated by the purple line). This was the same behaviour that was observed in the symmetric boundary condition (black line). Furthermore, comparing the velocity contour (Figure 5.2) of the plane

in the middle of the model (represented by the purple line in Figure 5.1) and at the symmetry plane (represented by the black line in Figure 5.1), verifies that they are near identical. This further validates the applicability of the symmetry boundary condition for the SP scaffolds.

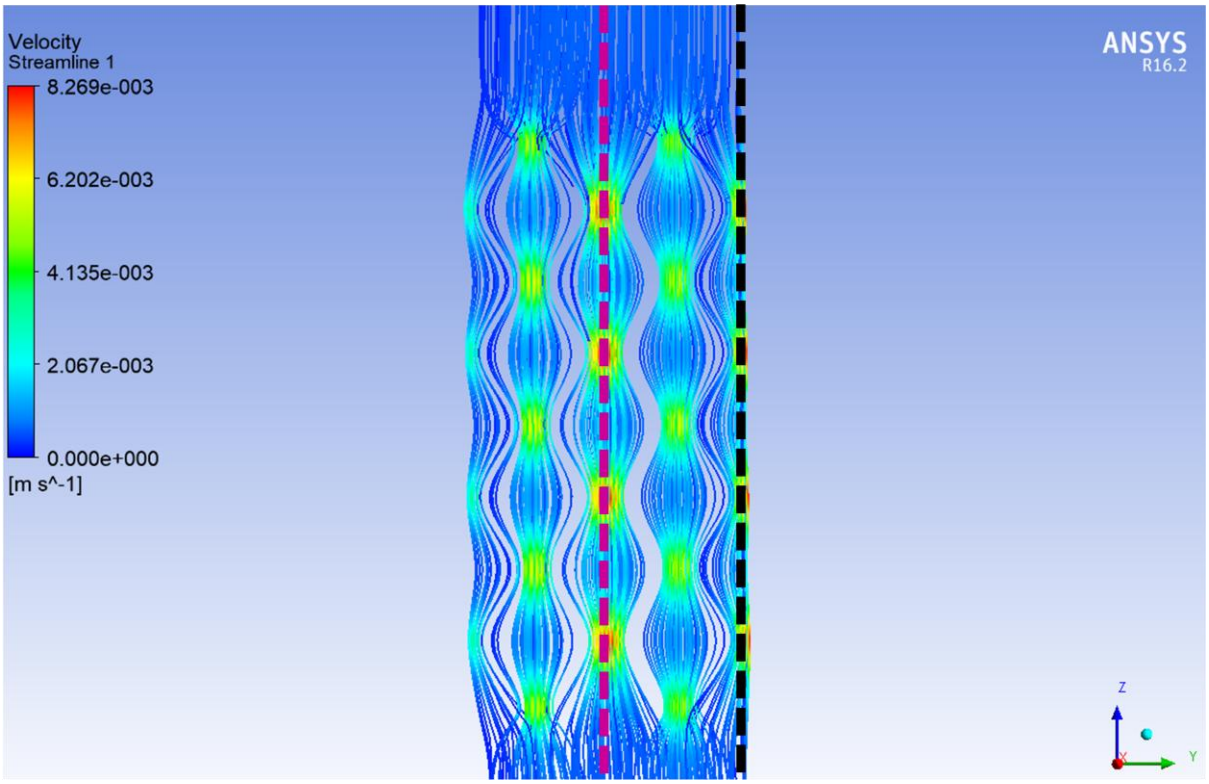

Figure 5.1. Streamlines for a SP70 scaffold with an inlet velocity of 5 ml/min, with a symmetry boundary condition in the right side (black line) and the middle of the model (purple line).

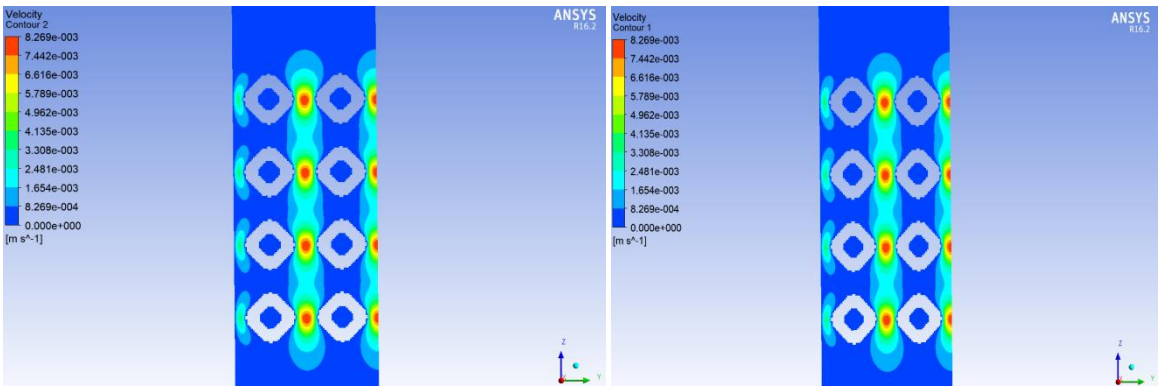

Figure 5.2. Comparison of the velocity contour of the fluid at the middle of the model (left) and at the symmetry plane (right) with an inlet velocity of 5 ml/min of a SP70 scaffold.

The measurements of the pressure difference for the symmetric scaffolds and the empty symmetric chamber are shown in Table 5.2. Afterwards, the $\Delta P_{scaffold}$ from equation 3.1. was calculated based on both of those measurements, with it being expressed in Table 5.3. Using Darcy's law we obtained the permeability for these scaffolds which can be seen in Table 5.4 and in Figure 5.3.

Table 5.2. Measured pressure difference of the numerical simulation of the symmetric models.

Flow rate (ml/min)	$\Delta P_{Measured}$ (Pa)				ΔP_{Empty}
	SP50	SP60	SP70	SP80	
1	1.172	0.259	0.111	0.065	0.002
2	2.355	0.518	0.223	0.130	0.004
3	3.570	0.781	0.335	0.195	0.006
4	4.803	1.043	0.447	0.260	0.008
5	6.089	1.310	0.561	0.326	0.011
10	13.243	2.707	1.143	0.660	0.021
20	31.509	5.947	2.426	1.378	0.044
40	81.883	14.223	5.540	3.059	0.091
60	147.622	24.479	9.255	5.018	0.143
80	-	36.315	13.437	7.187	0.197
100	-	49.613	18.062	9.559	0.255

Table 5.3. Calculated pressure drop for the symmetric scaffolds.

Flow rate (ml/min)	$\Delta P_{Scaffold}$ (Pa)			
	SP50	SP60	SP70	SP80
1	1.170	0.257	0.109	0.063
2	2.351	0.514	0.219	0.125
3	3.563	0.774	0.329	0.189
4	4.795	1.034	0.439	0.251
5	6.078	1.300	0.550	0.315
10	13.222	2.686	1.121	0.639
20	31.466	5.903	2.382	1.334
40	81.792	14.132	5.449	2.968
60	147.479	24.337	9.113	4.875
80	-	36.118	13.239	6.990
100	-	49.357	17.807	9.303

Table 5.4. Resulting permeability for the symmetric scaffolds.

Flow rate (ml/min)	Permeability (mm^2)			
	SP50	SP60	SP70	SP80
1	$1.10 * 10^{-3}$	$4.99 * 10^{-3}$	$11.73 * 10^{-3}$	$20.44 * 10^{-3}$
2	$1.09 * 10^{-3}$	$4.99 * 10^{-3}$	$11.74 * 10^{-3}$	$20.45 * 10^{-3}$
3	$1.08 * 10^{-3}$	$4.97 * 10^{-3}$	$11.70 * 10^{-3}$	$20.39 * 10^{-3}$
4	$1.07 * 10^{-3}$	$4.96 * 10^{-3}$	$11.70 * 10^{-3}$	$20.40 * 10^{-3}$
5	$1.06 * 10^{-3}$	$4.93 * 10^{-3}$	$11.65 * 10^{-3}$	$20.35 * 10^{-3}$
10	$0.97 * 10^{-3}$	$4.77 * 10^{-3}$	$11.44 * 10^{-3}$	$20.08 * 10^{-3}$
20	$0.82 * 10^{-3}$	$4.34 * 10^{-3}$	$10.76 * 10^{-3}$	$19.22 * 10^{-3}$
40	$0.63 * 10^{-3}$	$3.63 * 10^{-3}$	$9.41 * 10^{-3}$	$17.28 * 10^{-3}$
60	$0.52 * 10^{-3}$	$3.16 * 10^{-3}$	$8.44 * 10^{-3}$	$15.78 * 10^{-3}$
80	-	$2.84 * 10^{-3}$	$7.75 * 10^{-3}$	$14.67 * 10^{-3}$
100	-	$2.60 * 10^{-3}$	$7.20 * 10^{-3}$	$13.78 * 10^{-3}$

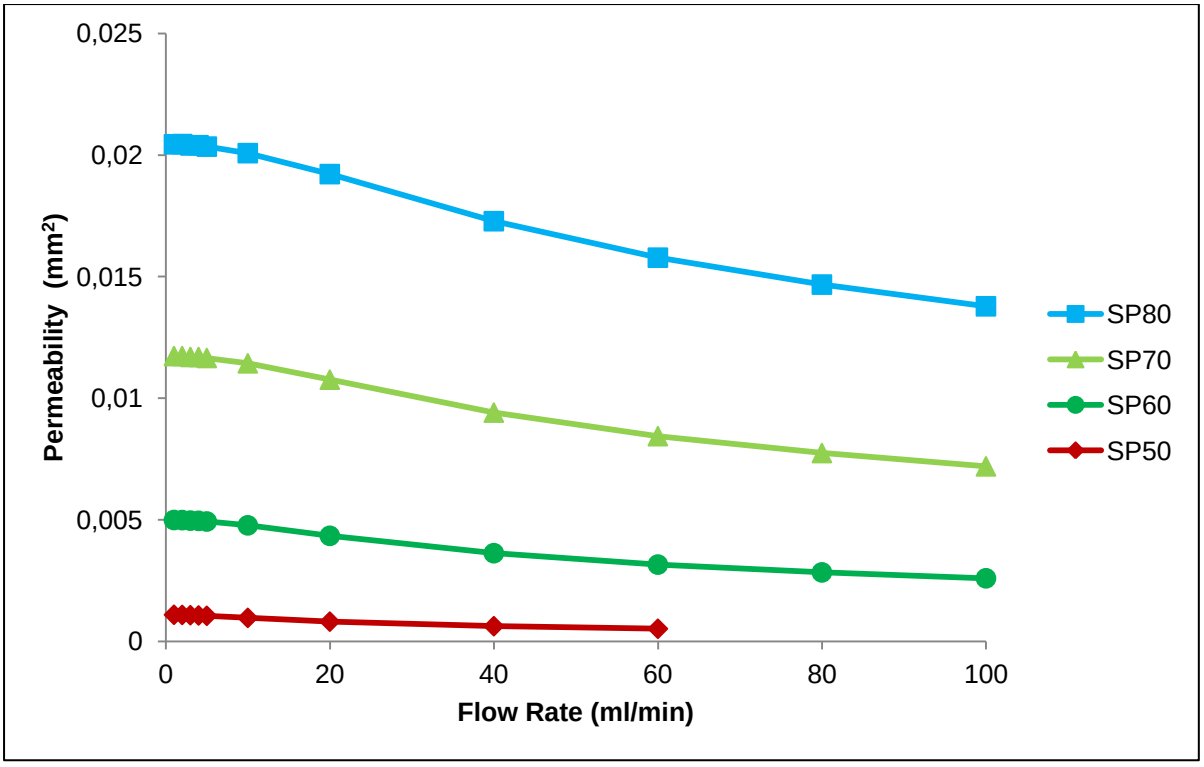

Figure 5.3. Calculated permeability in function of the flow rate for all of the four symmetric scaffold models.

As expected, there were higher permeability values for the scaffolds with the highest porosity; however, these values started to decrease at a flow rate of around 20 ml/min, signalling the point where the flow starts to exit the domain of Darcy's law. Nevertheless, this law is still applicable for the analysis of the fluid flow. Finally, for the flow rates of 80 and 100 ml/min, the numerical simulation did not converge for the SP50 scaffold, signalling the occurrence of a turbulent flow instead of the expected laminar flow. Because of this, no results could be obtained for those two simulations.

5.2. Periodic models

In the simulations of the periodic model of the empty chamber it was determined that the ΔP_{Empty} pressure value, for all of the inlet velocities, was approximately zero. This means that there was no significant difference between the values of $\Delta P_{Measured}$ and $\Delta P_{Scaffold}$, therefore only the values of $\Delta P_{Scaffold}$ were registered in Table 5.5, Table 5.6 and Table 5.7 (one for each of the scaffold geometries). The calculated permeability values are presented in Table 5.8, Table 5.9, Table 5.10, Figure 5.4, Figure 5.5, Figure 5.6 and Figure 5.7. The division of the permeability results between two graphs is because of the large number of results that could not be clearly legible in a single graph.

Table 5.5. Calculated pressure drop for the periodic SP scaffolds.

Flow rate (ml/min)	$\Delta P_{Scaffold}$ (Pa)			
	SP50	**SP60**	**SP70**	**SP80**
1	0.951	0.211	0.091	0.053
2	1.911	0.423	0.183	0.105
3	2.894	0.637	0.275	0.159
4	3.890	0.850	0.367	0.211
5	4.925	1.068	0.460	0.265
10	10.713	2.197	0.935	0.535
20	26.186	4.822	1.977	1.112
40	70.310	11.740	4.554	2.473
60	127.348	20.423	7.693	4.086
80	194.554	30.412	11.237	5.883
100	271.918	41.595	15.155	7.847

Table 5.6. Calculated pressure drop for the periodic SD scaffolds.

Flow rate (ml/min)	$\Delta P_{Scaffold}$ (Pa)			
	SD50	**SD60**	**SD70**	**SD80**
1	0.408	0.241	0.151	0.1039
2	0.815	0.482	0.302	0.208
3	1.225	0.724	0.453	0.312
4	1.631	0.964	0.604	0.415
5	2.042	1.207	0.756	0.520
10	4.099	2.420	1.514	1.041
20	8.269	4.869	3.044	2.092
40	17.007	9.958	6.206	4.259
60	26.475	15.401	9.565	6.552
80	36.680	21.195	13.113	8.964
100	47.728	27.393	16.881	11.515

Table 5.7. Calculated pressure drop for the periodic SG scaffolds.

Flow rate (ml/min)	$\Delta P_{Scaffold}$ (Pa)			
	SG50	**SG60**	**SG70**	**SG80**
1	0.219	0.132	0.089	0.061
2	0.437	0.264	0.177	0.123
3	0.657	0.3968	0.266	0.184
4	0.875	0.528	0.355	0.245
5	1.096	0.661	0.444	0.307
10	2.198	1.326	0.890	0.616
20	4.443	2.677	1.796	1.242
40	9.233	5.552	3.719	2.573
60	14.681	8.808	5.894	4.076
80	20.946	12.542	8.382	5.791
100	28.134	16.810	11.216	7.735

Table 5.8. Resulting permeability for the periodic SP scaffolds.

Flow rate (ml/min)	Permeability (mm^2)			
	SP50	**SP60**	**SP70**	**SP80**
1	$1.35 * 10^{-3}$	$6.07 * 10^{-3}$	$14.02 * 10^{-3}$	$24.31 * 10^{-3}$
2	$1.34 * 10^{-3}$	$6.06 * 10^{-3}$	$14.02 * 10^{-3}$	$24.32 * 10^{-3}$
3	$1.33 * 10^{-3}$	$6.04 * 10^{-3}$	$13.98 * 10^{-3}$	$24.26 * 10^{-3}$
4	$1.32 * 10^{-3}$	$6.03 * 10^{-3}$	$13.98 * 10^{-3}$	$24.27 * 10^{-3}$
5	$1.30 * 10^{-3}$	$6.01 * 10^{-3}$	$13.93 * 10^{-3}$	$24.21 * 10^{-3}$
10	$1.20 * 10^{-3}$	$5.84 * 10^{-3}$	$13.71 * 10^{-3}$	$23.95 * 10^{-3}$
20	$0.98 * 10^{-3}$	$5.32 * 10^{-3}$	$12.97 * 10^{-3}$	$23.06 * 10^{-3}$
40	$0.73 * 10^{-3}$	$4.37 * 10^{-3}$	$11.26 * 10^{-3}$	$20.74 * 10^{-3}$
60	$0.60 * 10^{-3}$	$3.77 * 10^{-3}$	$10.00 * 10^{-3}$	$18.83 * 10^{-3}$
80	$0.53 * 10^{-3}$	$3.37 * 10^{-3}$	$9.13 * 10^{-3}$	$17.44 * 10^{-3}$
100	$0.47 * 10^{-3}$	$3.08 * 10^{-3}$	$8.46 * 10^{-3}$	$16.34 * 10^{-3}$

Table 5.9. Resulting permeability for the periodic SD scaffolds.

Flow rate (ml/min)	Permeability (mm^2)			
	SD50	**SD60**	**SD70**	**SD80**
1	$3.15 * 10^{-3}$	$5.32 * 10^{-3}$	$8.49 * 10^{-3}$	$12.34 * 10^{-3}$
2	$3.15 * 10^{-3}$	$5.32 * 10^{-3}$	$8.50 * 10^{-3}$	$12.35 * 10^{-3}$
3	$3.14 * 10^{-3}$	$5.31 * 10^{-3}$	$8.48 * 10^{-3}$	$12.35 * 10^{-3}$
4	$3.14 * 10^{-3}$	$5.32 * 10^{-3}$	$8.49 * 10^{-3}$	$12.35 * 10^{-3}$
5	$3.14 * 10^{-3}$	$5.31 * 10^{-3}$	$8.48 * 10^{-3}$	$12.33 * 10^{-3}$
10	$3.13 * 10^{-3}$	$5.30 * 10^{-3}$	$8.47 * 10^{-3}$	$12.31 * 10^{-3}$
20	$3.10 * 10^{-3}$	$5.26 * 10^{-3}$	$8.43 * 10^{-3}$	$12.26 * 10^{-3}$
40	$3.02 * 10^{-3}$	$5.15 * 10^{-3}$	$8.26 * 10^{-3}$	$12.04 * 10^{-3}$
60	$2.91 * 10^{-3}$	$5.00 * 10^{-3}$	$8.04 * 10^{-3}$	$11.74 * 10^{-3}$
80	$2.80 * 10^{-3}$	$4.84 * 10^{-3}$	$7.82 * 10^{-3}$	$11.44 * 10^{-3}$
100	$2.69 * 10^{-3}$	$4.68 * 10^{-3}$	$7.60 * 10^{-3}$	$11.13 * 10^{-3}$

Table 5.10. Resulting permeability for the periodic SG scaffolds.

Flow rate (ml/min)	Permeability (mm^2)			
	SG50	**SG60**	**SG70**	**SG80**
1	$5.86 * 10^{-3}$	$9.70 * 10^{-3}$	$14.46 * 10^{-3}$	$20.89 * 10^{-3}$
2	$5.87 * 10^{-3}$	$9.71 * 10^{-3}$	$14.47 * 10^{-3}$	$20.90 * 10^{-3}$
3	$5.85 * 10^{-3}$	$9.69 * 10^{-3}$	$14.44 * 10^{-3}$	$20.86 * 10^{-3}$
4	$5.86 * 10^{-3}$	$9.71 * 10^{-3}$	$14.46 * 10^{-3}$	$20.89 * 10^{-3}$
5	$5.85 * 10^{-3}$	$9.69 * 10^{-3}$	$14.44 * 10^{-3}$	$20.87 * 10^{-3}$
10	$5.83 * 10^{-3}$	$9.67 * 10^{-3}$	$14.40 * 10^{-3}$	$20.81 * 10^{-3}$
20	$5.77 * 10^{-3}$	$9.58 * 10^{-3}$	$14.28 * 10^{-3}$	$20.64 * 10^{-3}$
40	$5.55 * 10^{-3}$	$9.24 * 10^{-3}$	$13.79 * 10^{-3}$	$19.93 * 10^{-3}$
60	$5.24 * 10^{-3}$	$8.73 * 10^{-3}$	$13.05 * 10^{-3}$	$18.87 * 10^{-3}$
80	$4.90 * 10^{-3}$	$8.18 * 10^{-3}$	$12.24 * 10^{-3}$	$17.71 * 10^{-3}$
100	$4.56 * 10^{-3}$	$7.63 * 10^{-3}$	$11.43 * 10^{-3}$	$16.57 * 10^{-3}$

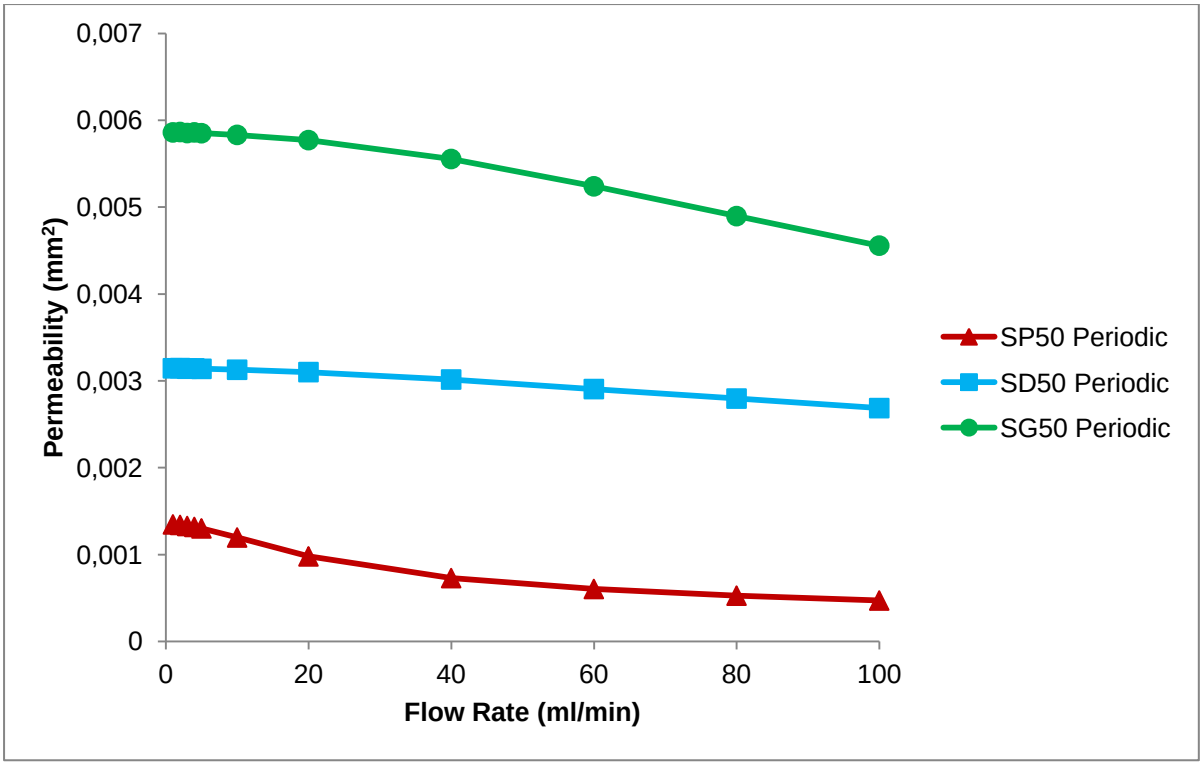

Figure 5.4. Calculated permeability in function of the flow rate for periodic scaffold models with 50% porosity.

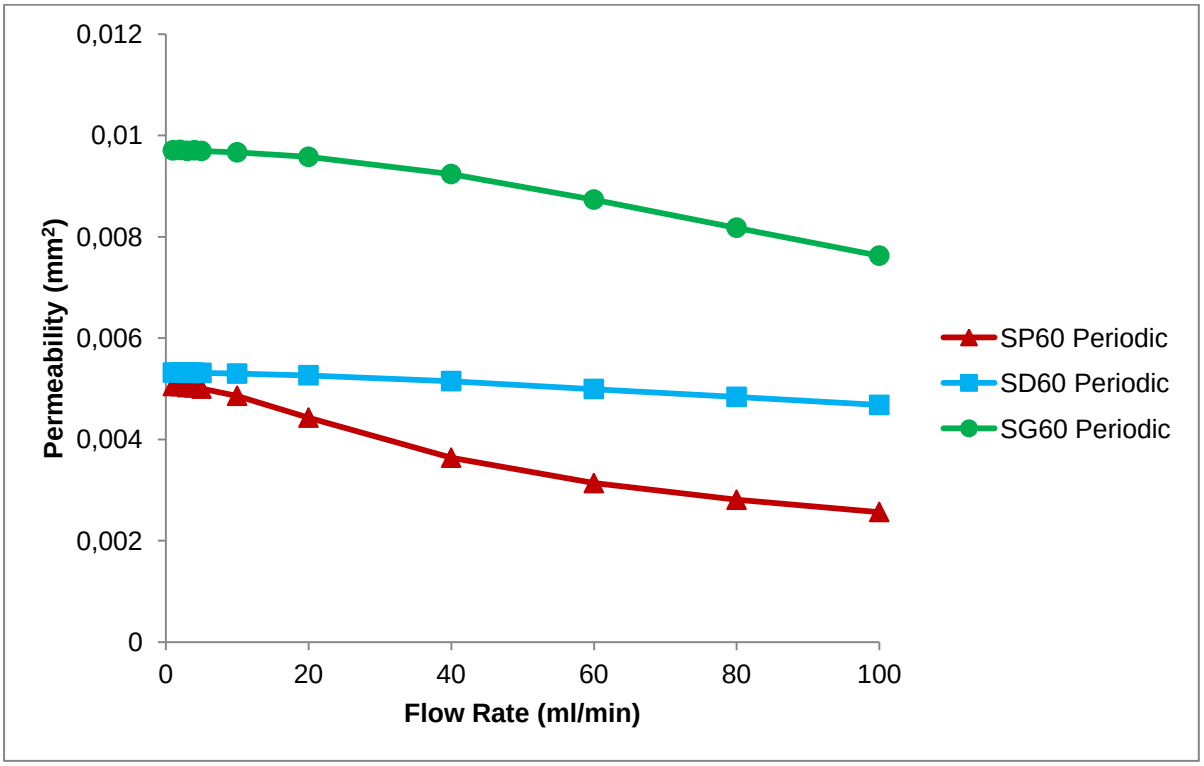

Figure 5.5. Calculated permeability in function of the flow rate for periodic scaffold models with 60% porosity.

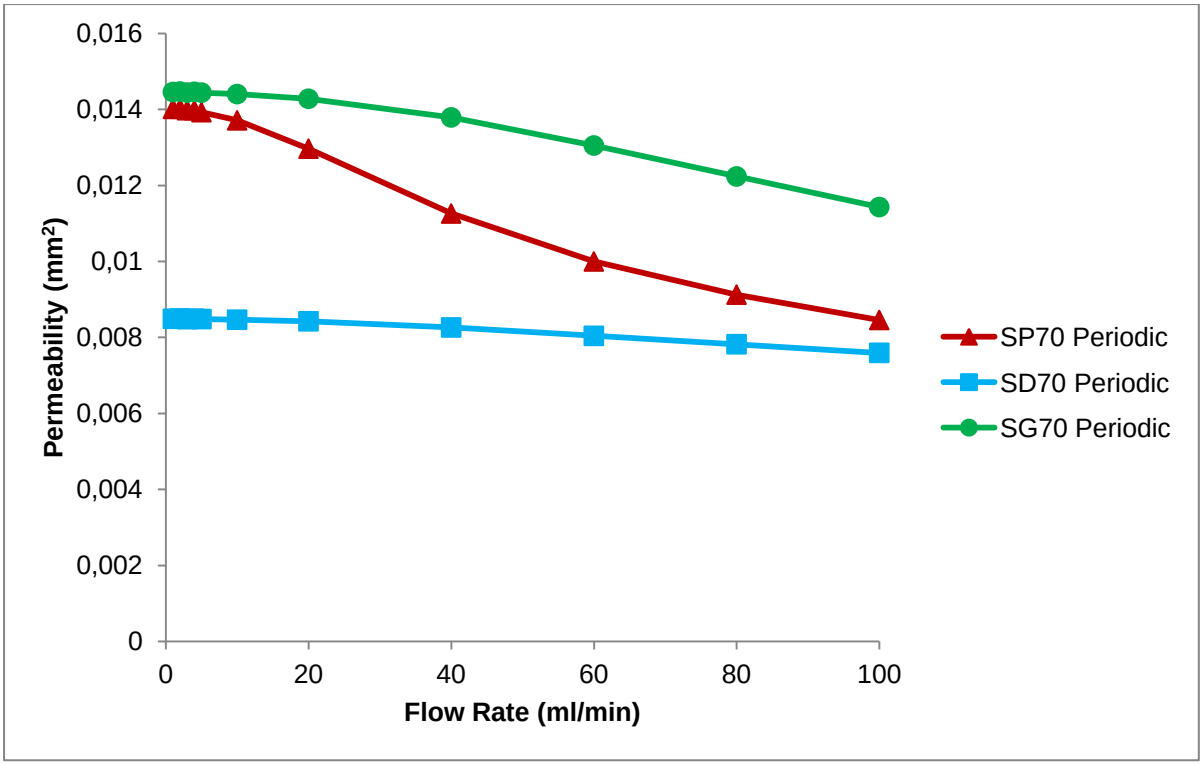

Figure 5.6. Calculated permeability in function of the flow rate for periodic scaffold models with 70% porosity.

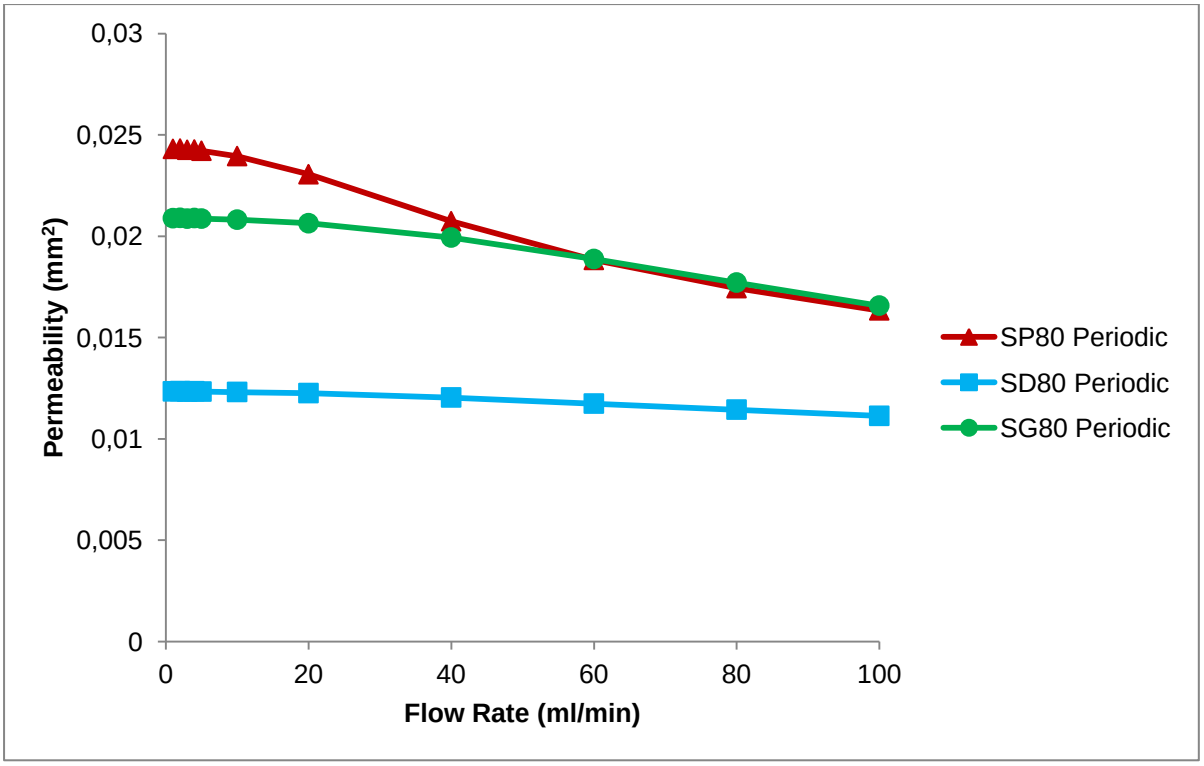

Figure 5.7. Calculated permeability in function of the flow rate for periodic scaffold models with 80% porosity.

The results show that all of the periodic models also suffered the same drop in permeability that was seen in the previous section. However, this decline was much higher in the SP geometries and barely noticeable in the SD geometries (gyroid structures presented an intermediate decline when compared to the other two). Also similar to what has observed in the previous chapter, was that geometries of the same type with higher porosity always resulted in a higher permeability.

When comparing the permeability of two scaffolds where one is not always higher than the other at all inlet flow rates (such as SP70 and SD80), the deciding factor should be the permeability at lower flow rates. This is because the lower flow rates results in velocities that are perfectly inside the domain of Darcy's law, unlike the higher flow rates. Taking this into consideration, the order of the permeability of the scaffolds (from the lowest permeability to the highest) was: SP50 < SD50 < SD60 < SG50 < SP60 < SD70 < SG60 < SD80 < SP70 < SG70 < SG80 < SP80. These results reveal how an increase of 20% porosity always leads to a better permeability, but the same does not always occur with a 10% increase (for example a SD70 scaffold has a lower permeability than a SG60 scaffold). Beyond that, the simulations also demonstrated how, for the same porosity, a SG scaffold always had a higher permeability than a SD scaffold. Finally, this set of simulations demonstrated how the SP scaffolds are the most influenced with the change in porosity, with SP80 having the highest permeability out of all 80% porous scaffolds; SP70 and SP60 having the middle values of permeability and SP50 having the worst.

5.3. Simplified models

The results for the simplified models were obtained following the same methods as discussed in section 5.1, namely measuring the $\Delta P_{Measured}$ and ΔP_{Empty} (Table 5.11, Table 5.12 and Table 5.13), and calculating the resulting $\Delta P_{Scaffold}$, (Table 5.14, Table 5.15 and Table 5.16) and permeability (Table 5.17, Table 5.18 and Table 5.19). The values of the permeability for all of the simplified models are shown in Figure 5.8, Figure 5.9, Figure 5.10 and Figure 5.11.

Table 5.11. Measured pressure difference of the numerical simulation of the simplified SP models.

Flow rate (ml/min)	$\Delta P_{Measured}$ (Pa)				ΔP_{Empty}
	SP50	SP60	SP70	SP80	
1	2.155	0.318	0.120	0.074	0.002
2	4.385	0.638	0.241	0.148	0.003
3	6.727	0.965	0.362	0.223	0.005
4	9.156	1.293	0.484	0.298	0.006
5	11.734	1.630	0.607	0.374	0.008
10	26.764	3.422	1.241	0.761	0.017
20	68.811	7.672	2.640	1.601	0.034
40	196.567	18.681	5.992	3.577	0.074
60	-	32.514	9.976	5.892	0.118
80	-	48.830	14.452	8.466	0.166
100	-	-	19.375	11.277	0.218

Table 5.12. Measured pressure difference of the numerical simulation of the simplified SD models.

Flow rate (ml/min)	$\Delta P_{Measured}$ (Pa)				ΔP_{Empty}
	SD50	SD60	SD70	SD80	
1	0.701	0.364	0.229	0.152	0.002
2	1.407	0.729	0.457	0.304	0.003
3	2.123	1.098	0.688	0.457	0.005
4	2.839	1.466	0.918	0.609	0.006
5	3.568	1.839	1.150	0.763	0.008
10	7.299	3.729	2.322	1.537	0.017
20	15.254	7.668	4.738	3.120	0.034
40	33.226	16.284	9.932	6.481	0.074
60	54.027	25.982	15.683	10.154	0.118
80	77.413	36.692	21.962	14.124	0.166
100	103.467	48.467	28.806	18.415	0.218

Table 5.13. Measured pressure difference of the numerical simulation of the simplified SG models.

Flow rate (ml/min)	$\Delta P_{Measured}$ (Pa)				ΔP_{Empty}
	SG50	SG60	SG70	SG80	
1	0.328	0.194	0.124	0.086	0.002
2	0.656	0.389	0.249	0.171	0.003
3	0.987	0.585	0.374	0.258	0.005
4	1.317	0.777	0.499	0.343	0.006
5	1.651	0.977	0.625	0.430	0.008
10	3.342	1.970	1.258	0.865	0.017
20	6.876	4.024	2.561	1.756	0.034
40	14.755	8.530	5.402	3.687	0.074
60	23.962	13.741	8.684	5.901	0.118
80	34.550	19.722	12.463	8.434	0.166
100	46.613	26.545	16.786	11.306	0.218

Table 5.14. Calculated pressure drop for the simplified SP scaffolds.

Flow rate (ml/min)	$\Delta P_{Scaffold}$ (Pa)			
	SP50	SP60	SP70	SP80
1	2.154	0.316	0.119	0.073
2	4.382	0.635	0.237	0.145
3	6.722	0.960	0.358	0.219
4	9.149	1.286	0.477	0.291
5	11.726	1.622	0.599	0.366
10	26.747	3.406	1.225	0.744
20	68.777	7.638	2.606	1.567
40	196.493	18.607	5.919	3.503
60	-	32.397	9.858	5.774
80	-	48.665	14.287	8.300
100	-	-	19.157	11.060

Table 5.15. Calculated pressure drop for the simplified SD scaffolds.

Flow rate (ml/min)	$\Delta P_{Scaffold}$ (Pa)			
	SD50	**SD60**	**SD70**	**SD80**
1	0.699	0.362	0.227	0.150
2	1.404	0.726	0.454	0.301
3	2.118	1.094	0.683	0.452
4	2.832	1.459	0.911	0.603
5	3.560	1.831	1.142	0.755
10	7.282	3.712	2.306	1.521
20	15.220	7.634	4.704	3.086
40	33.152	16.210	9.858	6.407
60	53.910	25.865	15.565	10.037
80	77.247	36.527	21.796	13.958
100	103.249	48.249	28.588	18.198

Table 5.16. Calculated pressure drop for the simplified SG scaffolds.

Flow rate (ml/min)	$\Delta P_{Scaffold}$ (Pa)			
	SG50	**SG60**	**SG70**	**SG80**
1	0.328	0.194	0.124	0.086
2	0.656	0.389	0.249	0.171
3	0.987	0.585	0.374	0.258
4	1.317	0.777	0.499	0.343
5	1.651	0.977	0.625	0.430
10	3.342	1.970	1.258	0.865
20	6.876	4.024	2.561	1.756
40	14.755	8.530	5.402	3.687
60	23.962	13.741	8.684	5.901
80	34.550	19.722	12.463	8.434
100	46.613	26.545	16.786	11.306

Table 5.17. Resulting permeability for the simplified SP scaffolds.

Flow rate (ml/min)	Permeability (mm^2)			
	SP50	**SP60**	**SP70**	**SP80**
1	$0.60 * 10^{-3}$	$4.05 * 10^{-3}$	$10.81 * 10^{-3}$	$17.66 * 10^{-3}$
2	$0.59 * 10^{-3}$	$4.03 * 10^{-3}$	$10.80 * 10^{-3}$	$17.66 * 10^{-3}$
3	$0.57 * 10^{-3}$	$4.01 * 10^{-3}$	$10.76 * 10^{-3}$	$17.60 * 10^{-3}$
4	$0.56 * 10^{-3}$	$3.99 * 10^{-3}$	$10.75 * 10^{-3}$	$17.59 * 10^{-3}$
5	$0.55 * 10^{-3}$	$3.95 * 10^{-3}$	$10.70 * 10^{-3}$	$17.53 * 10^{-3}$
10	$0.48 * 10^{-3}$	$3.77 * 10^{-3}$	$10.47 * 10^{-3}$	$17.22 * 10^{-3}$
20	$0.37 * 10^{-3}$	$3.36 * 10^{-3}$	$9.84 * 10^{-3}$	$16.37 * 10^{-3}$
40	$0.26 * 10^{-3}$	$2.76 * 10^{-3}$	$8.66 * 10^{-3}$	$14.64 * 10^{-3}$
60	-	$2.37 * 10^{-3}$	$7.80 * 10^{-3}$	$13.32 * 10^{-3}$
80	-	$2.11 * 10^{-3}$	$7.18 * 10^{-3}$	$12.36 * 10^{-3}$
100	-	-	$6.69 * 10^{-3}$	$11.59 * 10^{-3}$

Table 5.18. Resulting permeability for the simplified SD scaffolds.

Flow rate (ml/min)	Permeability (mm^2)			
	SD50	SD60	SD70	SD80
1	$1.83 * 10^{-3}$	$3.54 * 10^{-3}$	$5.65 * 10^{-3}$	$8.53 * 10^{-3}$
2	$1.83 * 10^{-3}$	$3.53 * 10^{-3}$	$5.65 * 10^{-3}$	$8.53 * 10^{-3}$
3	$1.82 * 10^{-3}$	$3.52 * 10^{-3}$	$5.63 * 10^{-3}$	$8.50 * 10^{-3}$
4	$1.81 * 10^{-3}$	$3.51 * 10^{-3}$	$5.63 * 10^{-3}$	$8.51 * 10^{-3}$
5	$1.80 * 10^{-3}$	$3.50 * 10^{-3}$	$5.61 * 10^{-3}$	$8.49 * 10^{-3}$
10	$1.76 * 10^{-3}$	$3.45 * 10^{-3}$	$5.56 * 10^{-3}$	$8.43 * 10^{-3}$
20	$1.69 * 10^{-3}$	$3.36 * 10^{-3}$	$5.45 * 10^{-3}$	$8.31 * 10^{-3}$
40	$1.55 * 10^{-3}$	$3.16 * 10^{-3}$	$5.20 * 10^{-3}$	$8.00 * 10^{-3}$
60	$1.43 * 10^{-3}$	$2.97 * 10^{-3}$	$4.94 * 10^{-3}$	$7.66 * 10^{-3}$
80	$1.33 * 10^{-3}$	$2.81 * 10^{-3}$	$4.71 * 10^{-3}$	$7.35 * 10^{-3}$
100	$1.24 * 10^{-3}$	$2.66 * 10^{-3}$	$4.49 * 10^{-3}$	$7.05 * 10^{-3}$

Table 5.19. Resulting permeability for the simplified SG scaffolds.

Flow rate (ml/min)	Permeability (mm^2)			
	SG50	SG60	SG70	SG80
1	$3.91 * 10^{-3}$	$6.60 * 10^{-3}$	$10.30 * 10^{-3}$	$14.96 * 10^{-3}$
2	$3.91 * 10^{-3}$	$6.60 * 10^{-3}$	$10.30 * 10^{-3}$	$14.96 * 10^{-3}$
3	$3.90 * 10^{-3}$	$6.58 * 10^{-3}$	$10.27 * 10^{-3}$	$14.93 * 10^{-3}$
4	$3.90 * 10^{-3}$	$6.60 * 10^{-3}$	$10.28 * 10^{-3}$	$14.94 * 10^{-3}$
5	$3.88 * 10^{-3}$	$6.56 * 10^{-3}$	$10.26 * 10^{-3}$	$14.91 * 10^{-3}$
10	$3.84 * 10^{-3}$	$6.51 * 10^{-3}$	$10.19 * 10^{-3}$	$14.83 * 10^{-3}$
20	$3.73 * 10^{-3}$	$6.37 * 10^{-3}$	$10.01 * 10^{-3}$	$14.60 * 10^{-3}$
40	$3.48 * 10^{-3}$	$6.01 * 10^{-3}$	$9.49 * 10^{-3}$	$13.91 * 10^{-3}$
60	$3.21 * 10^{-3}$	$5.60 * 10^{-3}$	$8.86 * 10^{-3}$	$13.04 * 10^{-3}$
80	$2.97 * 10^{-3}$	$5.20 * 10^{-3}$	$8.23 * 10^{-3}$	$12.16 * 10^{-3}$
100	$2.75 * 10^{-3}$	$4.83 * 10^{-3}$	$7.64 * 10^{-3}$	$11.34 * 10^{-3}$

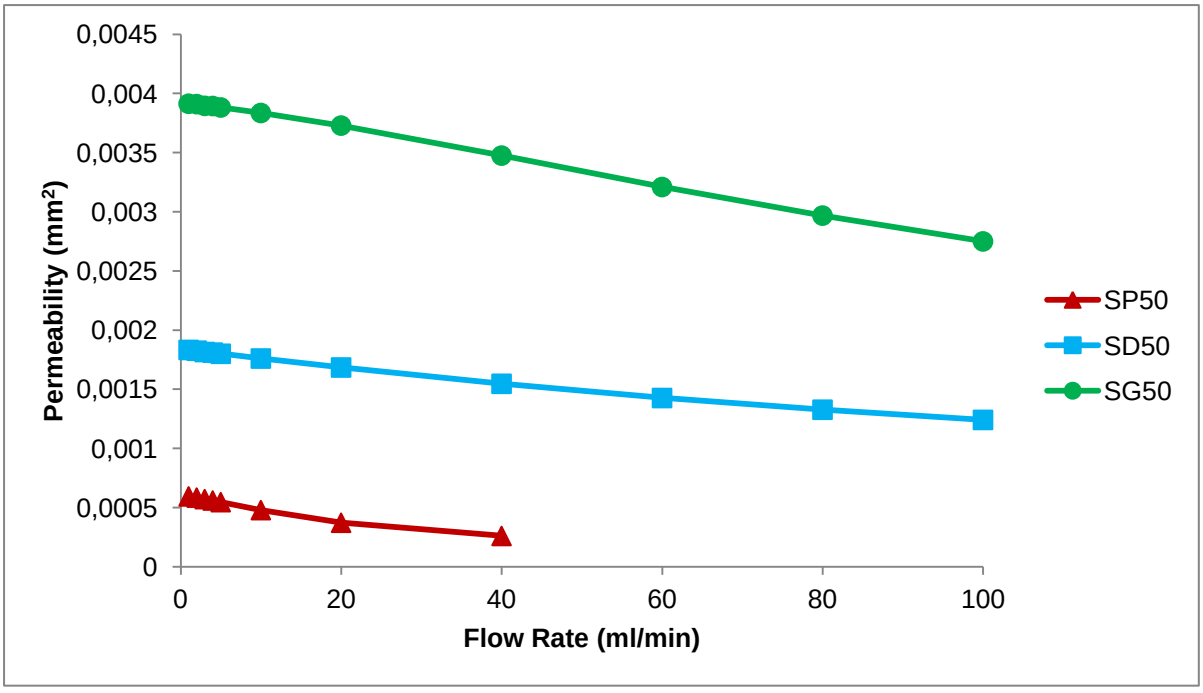

Figure 5.8. Calculated permeability in function of the flow rate for simplified scaffold models with 50% porosity.

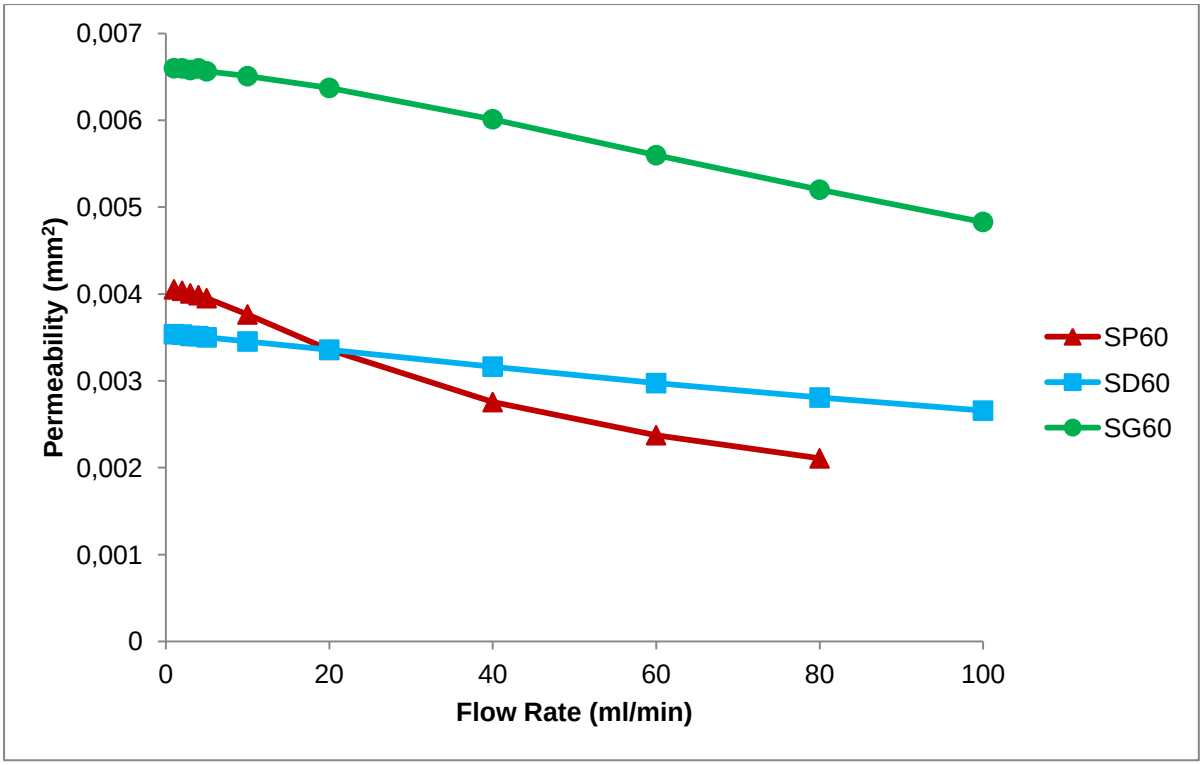

Figure 5.9. Calculated permeability in function of the flow rate for simplified scaffold models with 60% porosity.

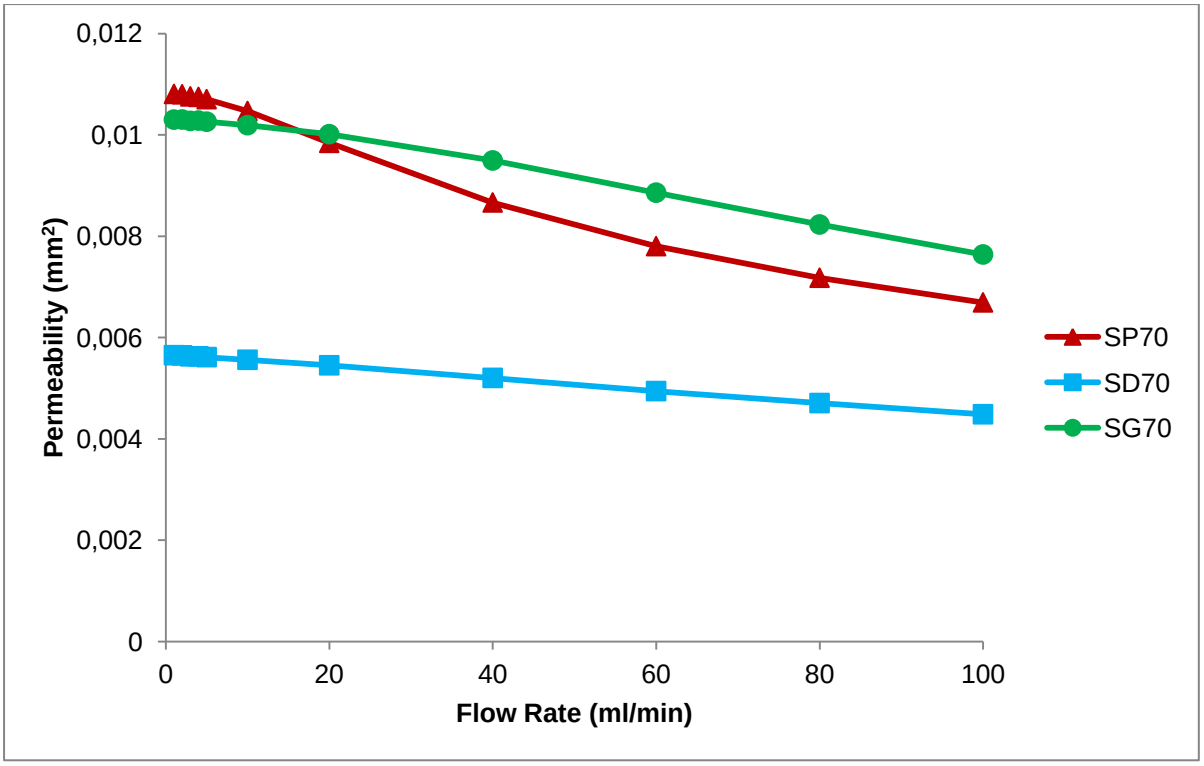

Figure 5.10. Calculated permeability in function of the flow rate for simplified scaffold models with 70% porosity.

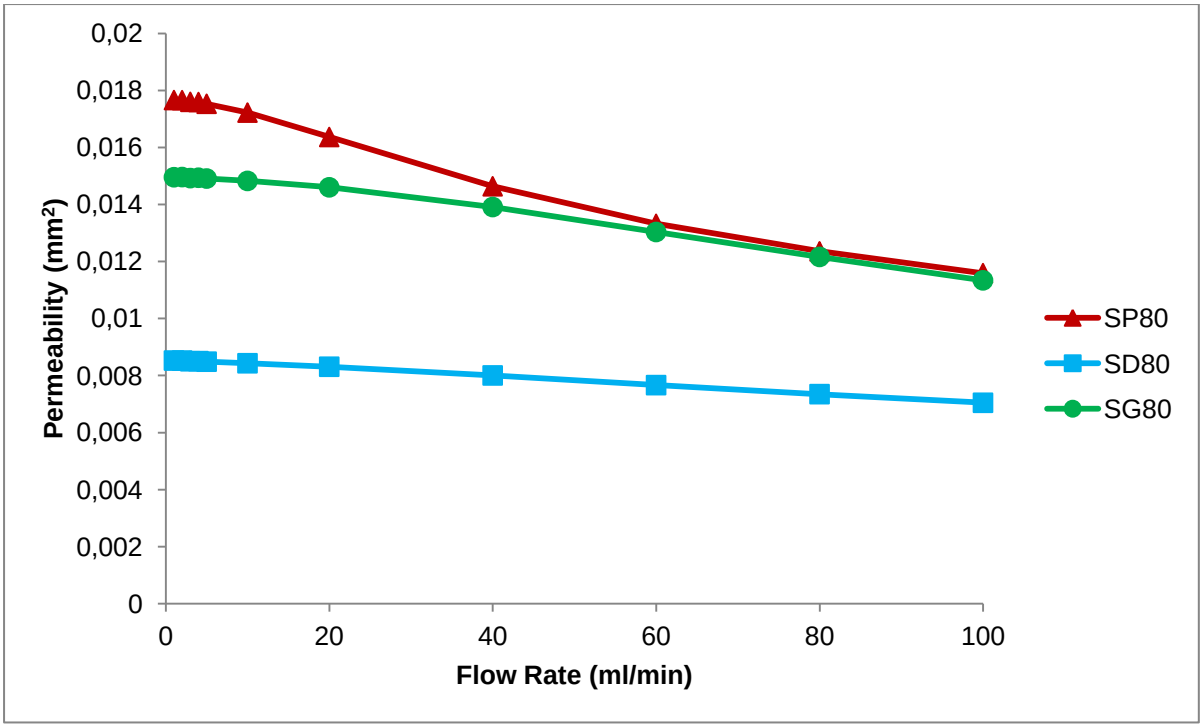

Figure 5.11. Calculated permeability in function of the flow rate for simplified scaffold models with 80% porosity.

The obtain values of permeability are in accordance with what was discussed in the previous section, with the only exception being the SG70 scaffolds having a slightly lower permeability than the SP70 scaffolds (instead of a slightly higher permeability).

5.4. Model comparison

This section focuses on the comparison between the permeability values of the three models. The limitation that first needs to be overcome is the fact that the periodic models do not take into account the effect on the wall of the permeability chamber, which would not allow a direct comparison with the other two models. To correct this shortcoming, a comparison was established between the permeability of the SP geometries of the periodic and symmetric models (since the SP symmetric models are the closest to an actual scaffold), represented in Figure 5.12, Figure 5.13, Figure 5.14 and Figure 5.15. This comparison confronted the individual permeability values from the symmetric models with the correspondent values (same scaffold and same inlet flow rate) from the periodic models. The comparison ascertained that values from the symmetric models were 15% to 18% lower than the periodic models, with an average of 16.7%. This value was the result of the effect of the chamber wall on the SP scaffolds (seeing as the chamber wall is the significant difference between the two models). Taking this into consideration, this effect of a decrease in permeability of 16.7% was applied to the twelve periodic models (by multiplying all the calculated permeabilities by a correction factor of 0.833, which was calculated from the 16.7%). The now corrected periodic models can then finally be compared to the simplified and symmetric models, as seen in Figure 5.16, Figure 5.17, Figure 5.18 and Figure 5.19.

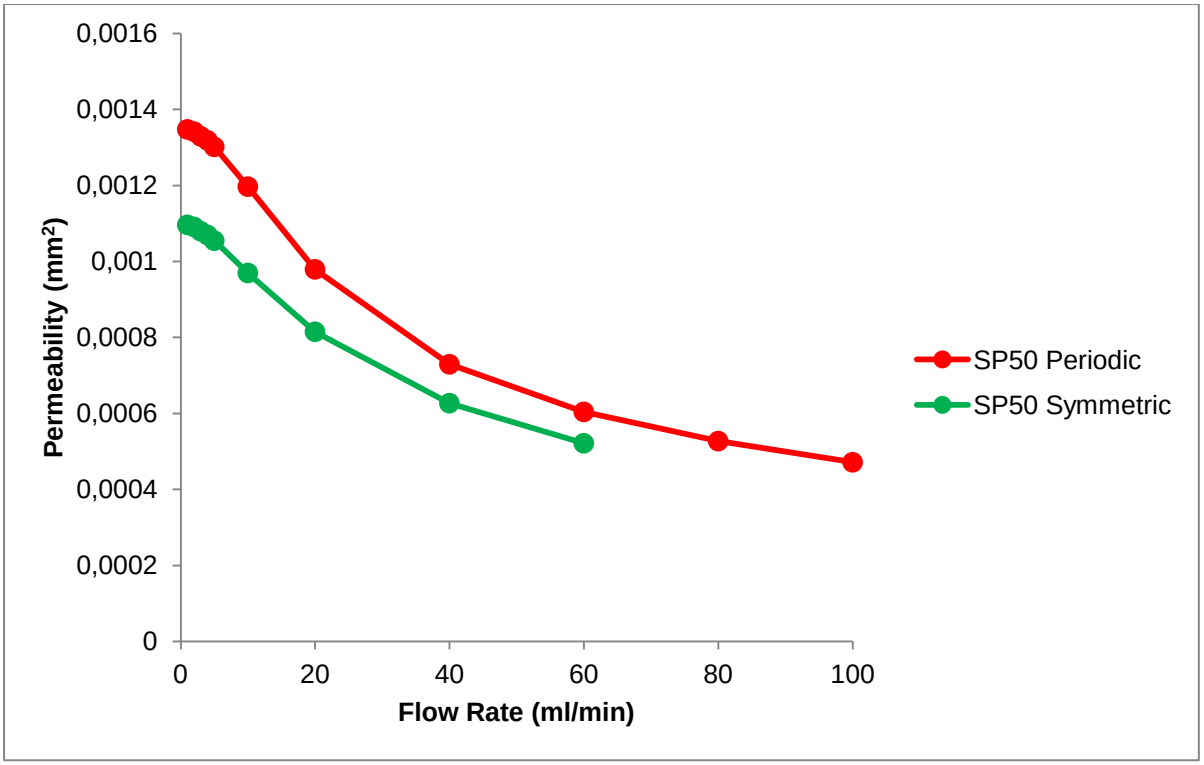

Figure 5.12. Calculated permeability in function of the flow rate for the periodic and symmetric models of the SP50 scaffold.

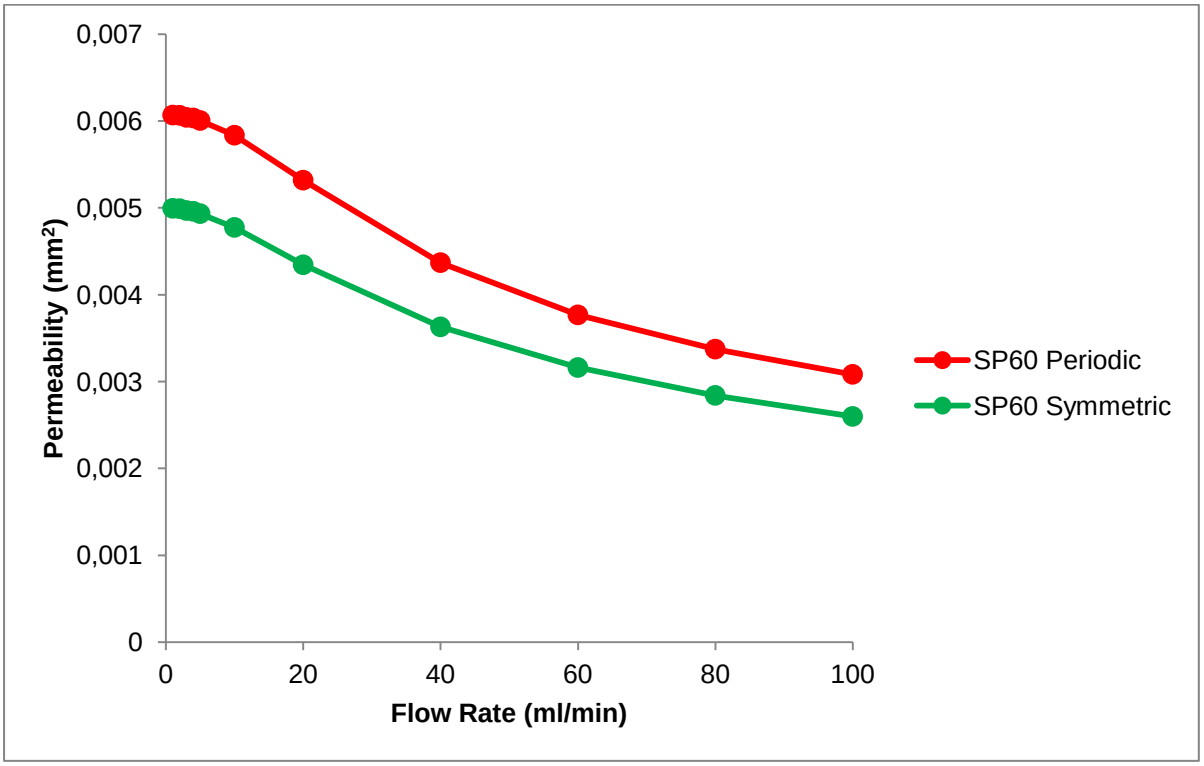

Figure 5.13. Calculated permeability in function of the flow rate for the periodic and symmetric models of the SP60 scaffold.

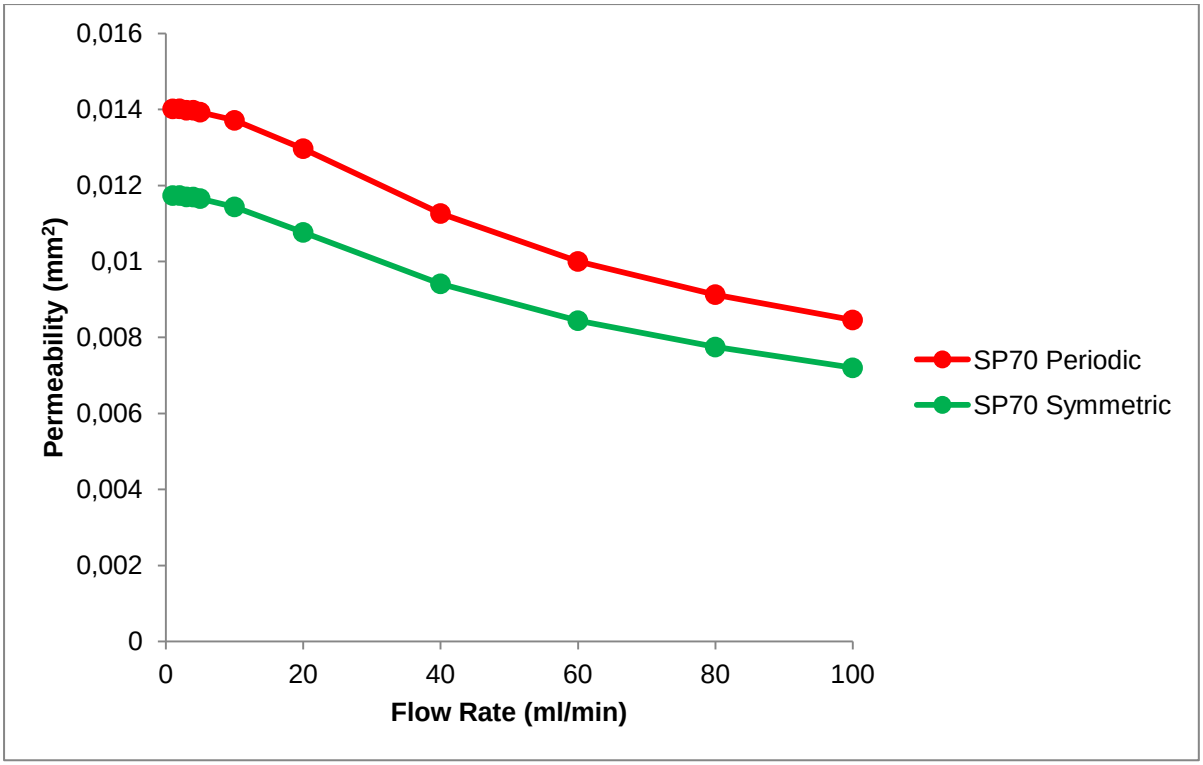

Figure 5.14. Calculated permeability in function of the flow rate for the periodic and symmetric models of the SP70 scaffold.

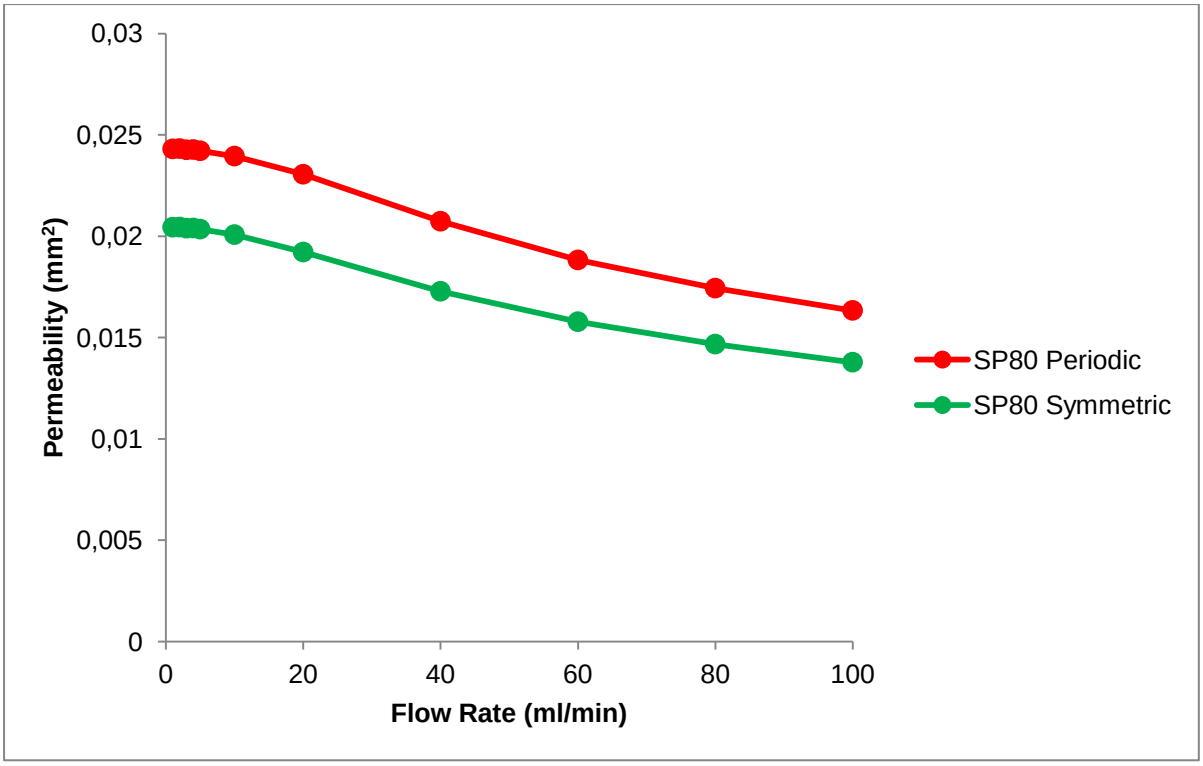

Figure 5.15. Calculated permeability in function of the flow rate for the periodic and symmetric models of the SP80 scaffold.

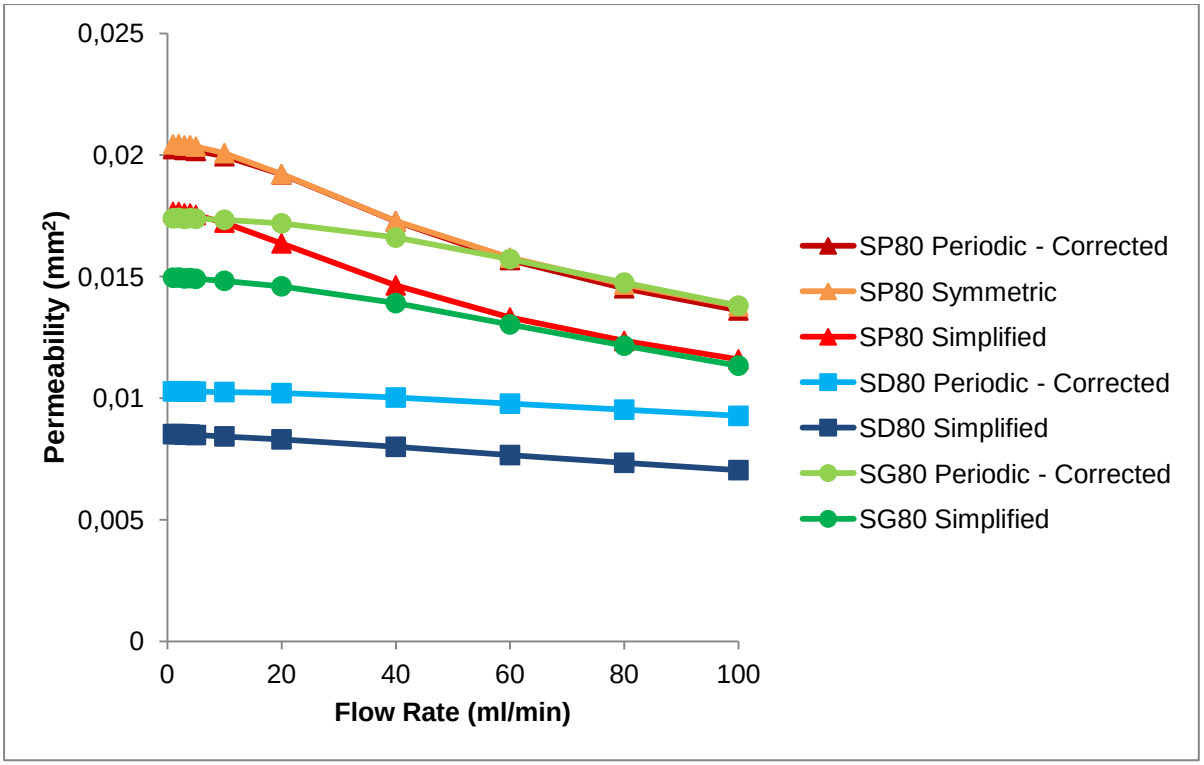

Figure 5.16. Calculated permeability in function of the flow rate for all scaffold models with 50% porosity.

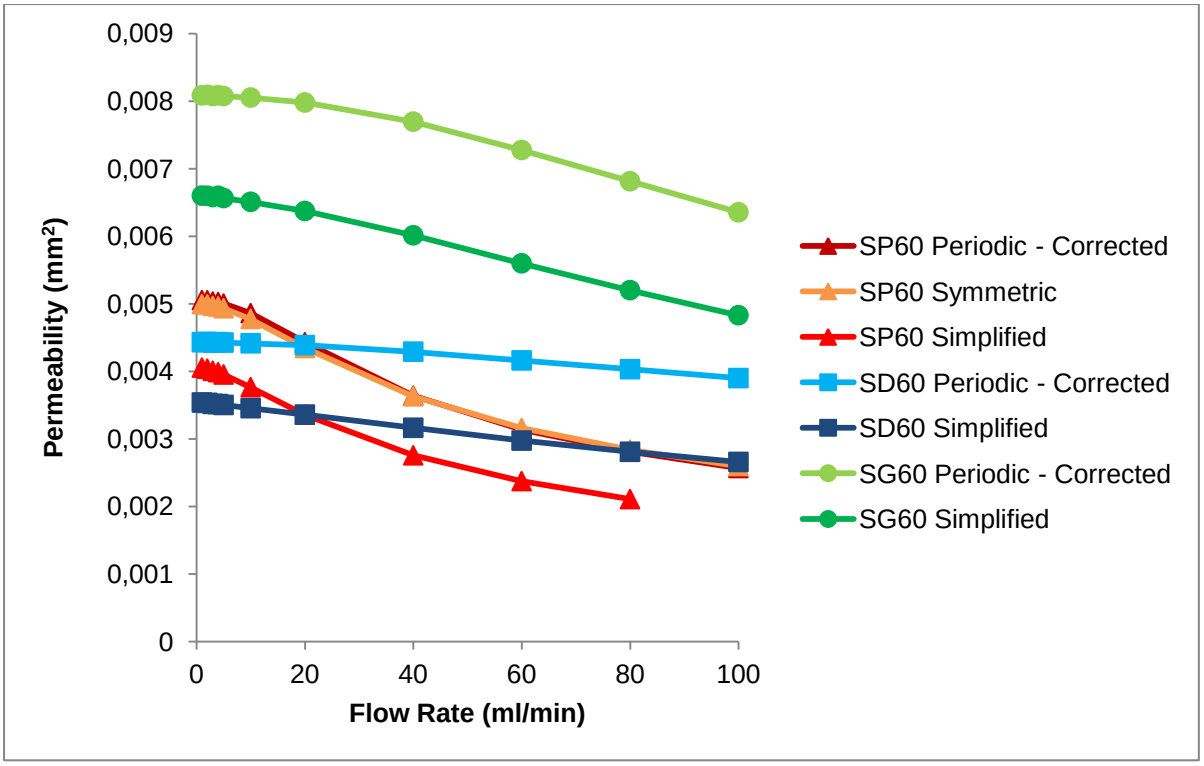

Figure 5.17. Calculated permeability in function of the flow rate for all scaffold models with 60% porosity.

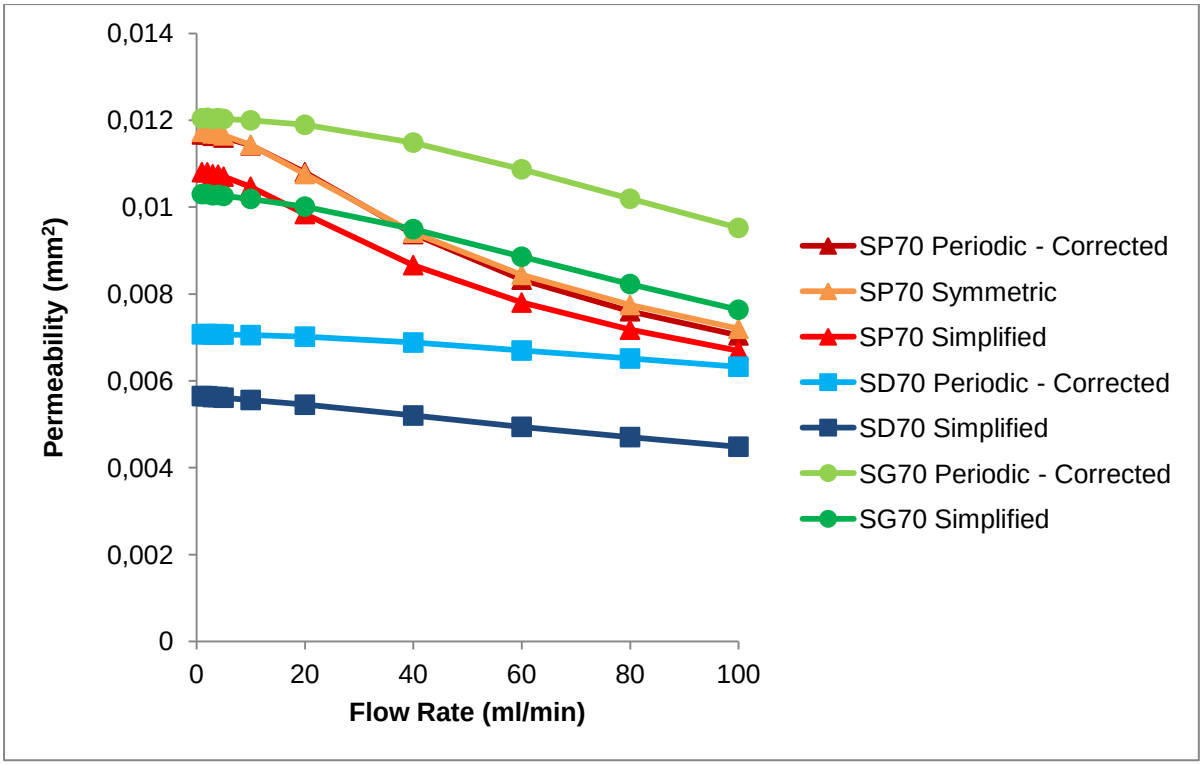

Figure 5.18. Calculated permeability in function of the flow rate for all scaffold models with 70% porosity.

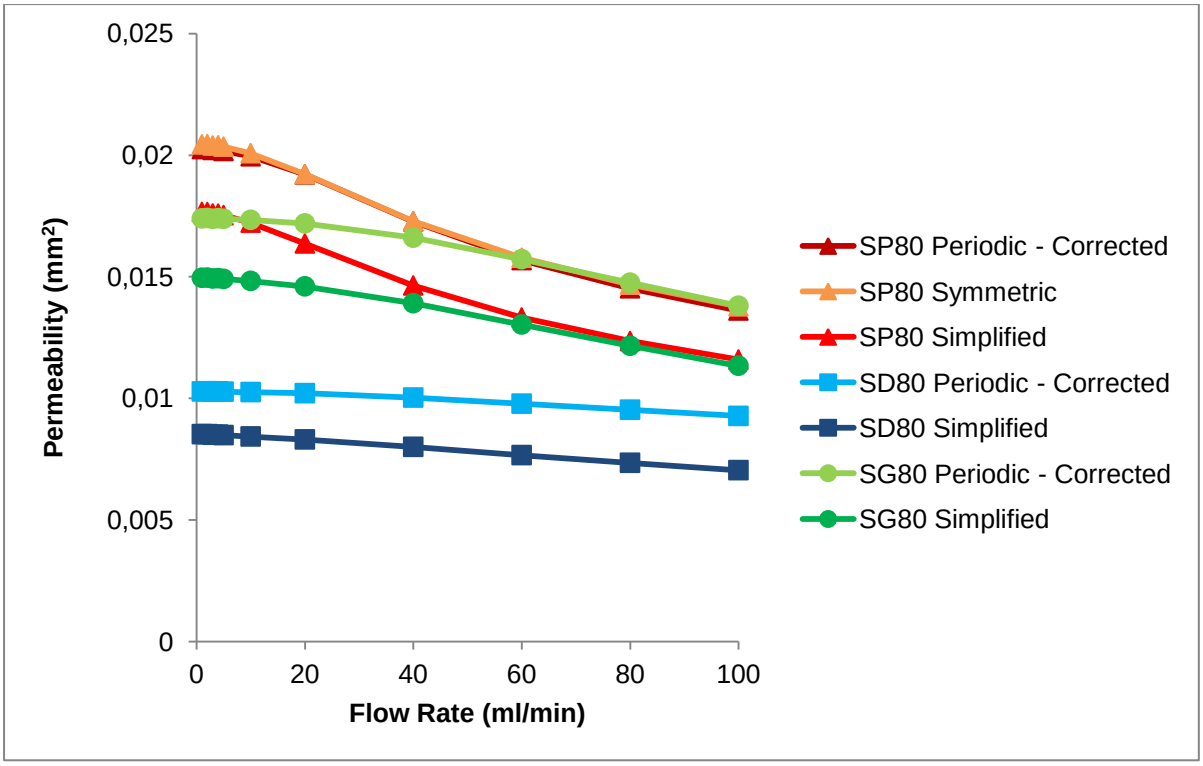

Figure 5.19. Calculated permeability in function of the flow rate for all scaffold models with 80% porosity.

The results from the SP geometries show how the calculated permeabilities from the symmetric simulations were almost identical to the values from the corrected periodic simulations. Furthermore, the results also demonstrate how the simplified models always had a lower calculated permeability comparatively to the corrected periodic models. However, it was not possible to establish a direct correlation between the values from the corrected periodic models and the simplified models (the simplified SP80 and SP60 models had a much higher difference to the corrected periodic models comparatively to the simplified SP70 model).

5.5. Experimental Results

Finally, this chapter presents the results from an experimental setup (the same setup used by *Castro et al. (2019)*). These results (obtained through an ongoing parallel research, with our contribution) are a selection of the porosities, namely 60% and 70% porous scaffolds, in order to evaluate the correlation between the experimental values and the numerical ones. The measured pressure drop of the six considered scaffolds; their calculated $\Delta P_{Scaffold}$ and permeability are presented in the appendix. The permeability values for the experimental scaffolds were compared with the previous results of the corrected periodic model and are displayed in Figure 5.20 and Figure 5.21.

In order to determine whether these two sets of permeability have a good correlation, a comparison was established between the two sets for all of the points as a whole (Figure 5.22) and for each of the scaffolds (Figure 5.23).

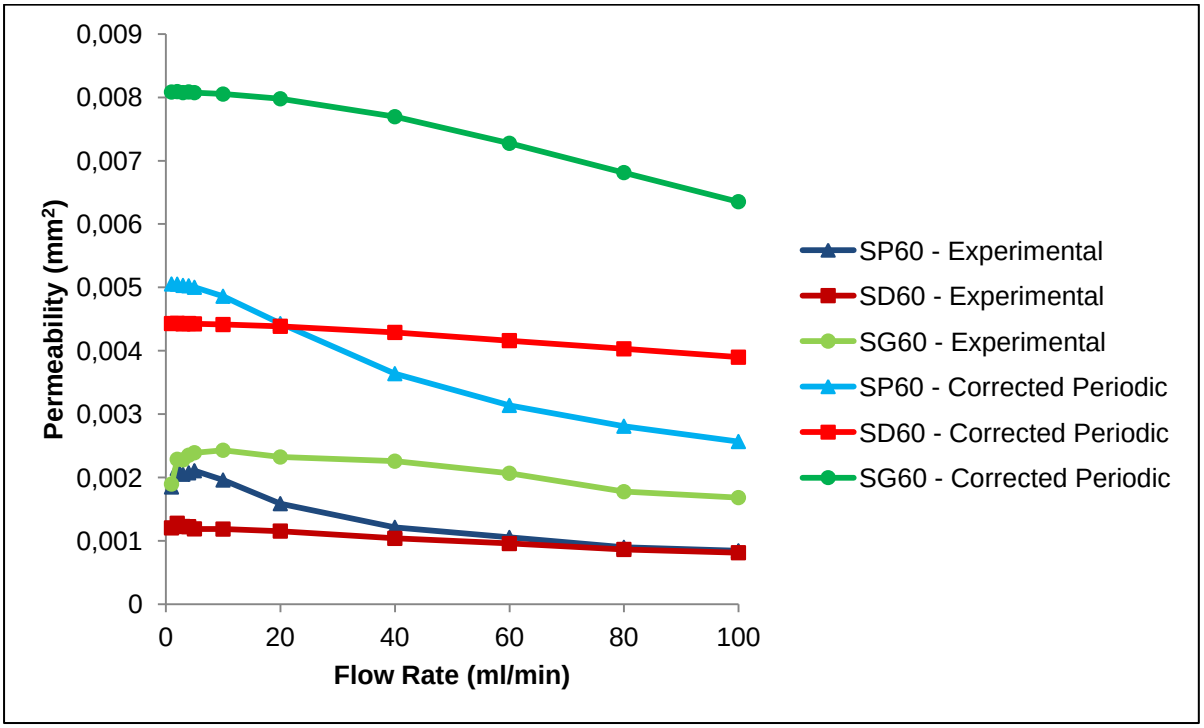

Figure 5.20. Calculated permeability in function of the flow rate for the experimental values and periodic values of scaffolds with 60% porosity.

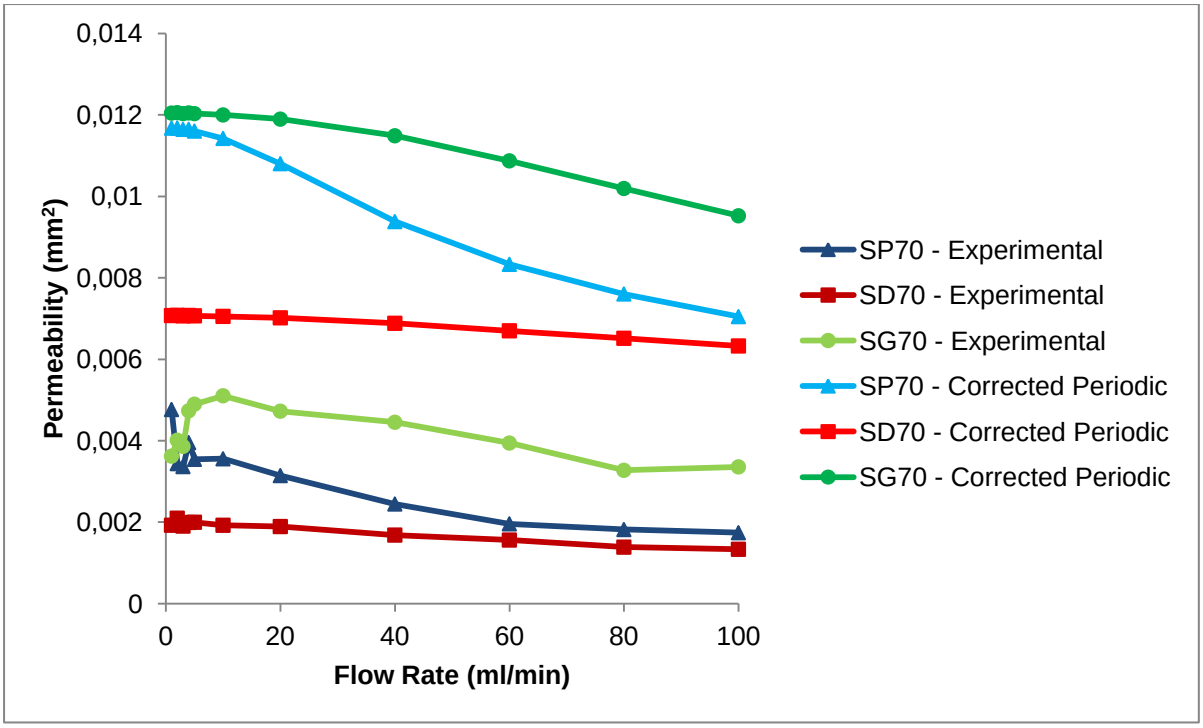

Figure 5.21. Calculated permeability in function of the flow rate for the experimental values and periodic values of scaffolds with 70% porosity.

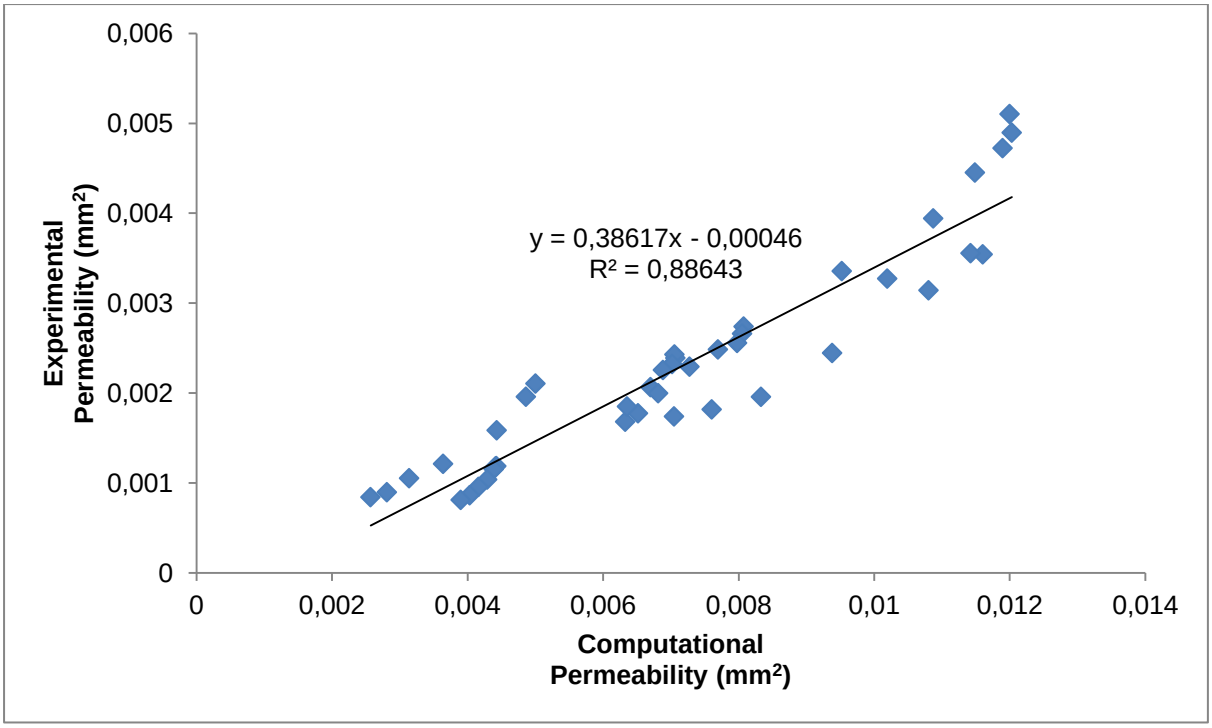

Figure 5.22. Correlation between the computationally calculated permeability and the experimentally measured permeability for all of the 60% and 70% scaffold porosities.

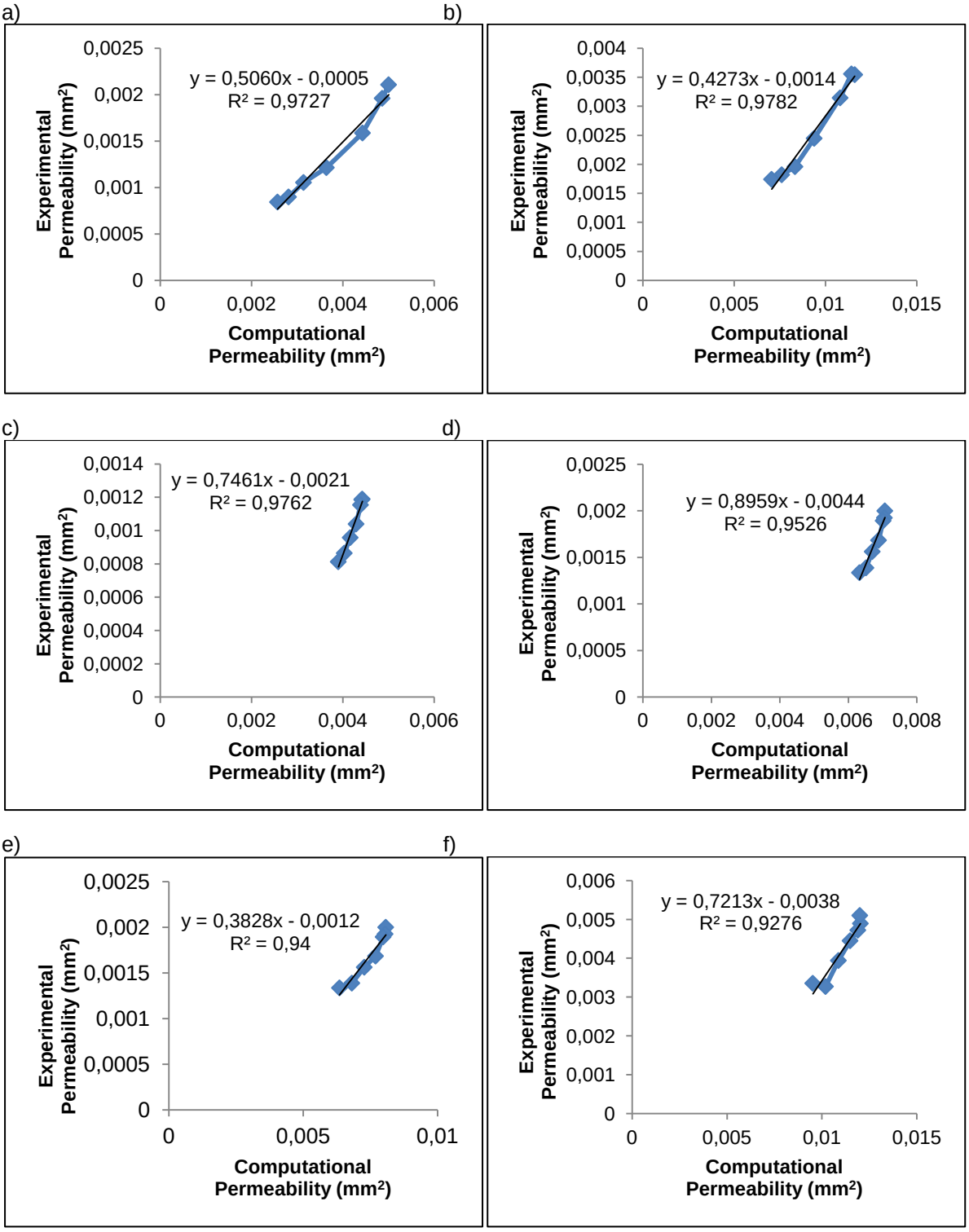

Figure 5.23. Correlation between the computationally calculated permeability and the experimentally measured permeability for a) SP60, b) SP70, c) SD60, d) SD70, e) SG60 and f) SG70.

5.6. Streamlines

The streamlines from each TPMS geometry, of the chosen porosity and inlet flow rate (70% porosity and 5 ml/min), are shown from an overview (Figure 5.24), a side view (Figure 5.25) and a view from the outlet at the bottom (Figure 5.26).

a)

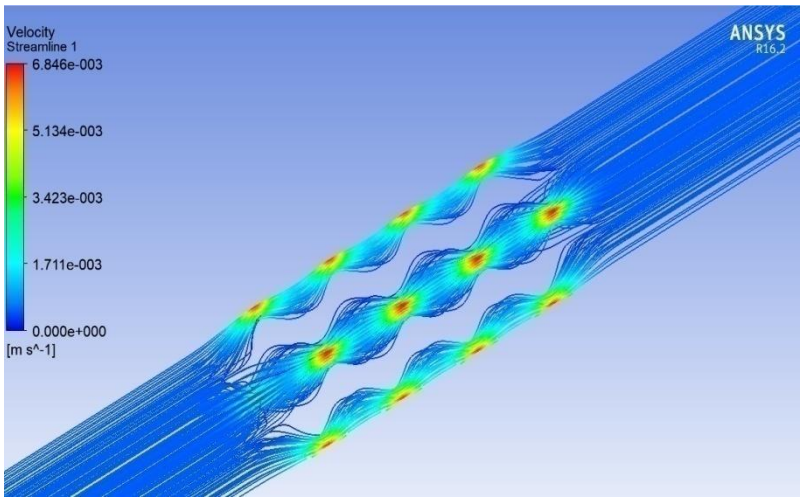

b)

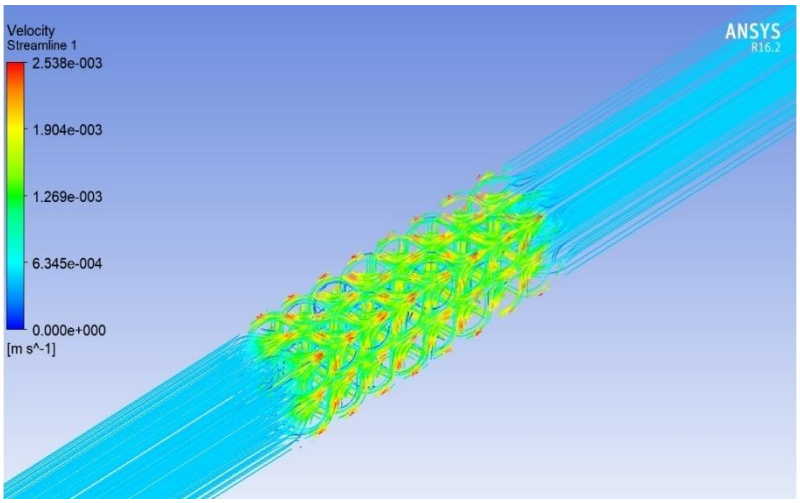

c)

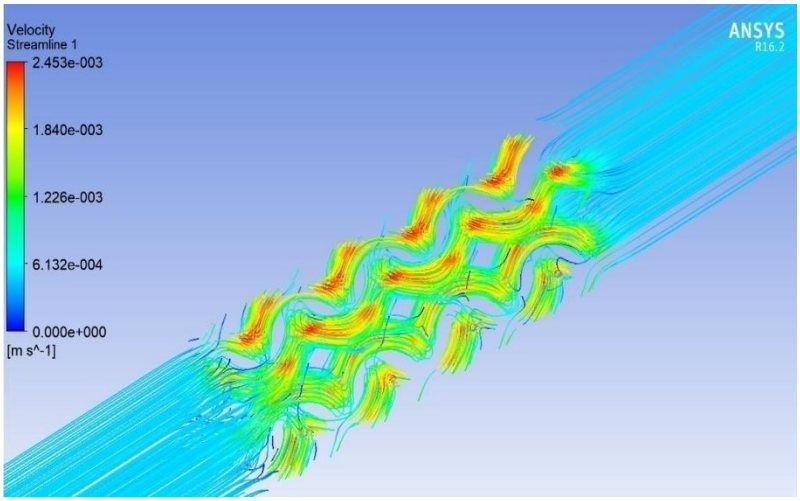

Figure 5.24. Overview of the streamlines of the a) SP70 scaffolds; b) SD70 scaffolds and c) SG70 scaffolds.

a)

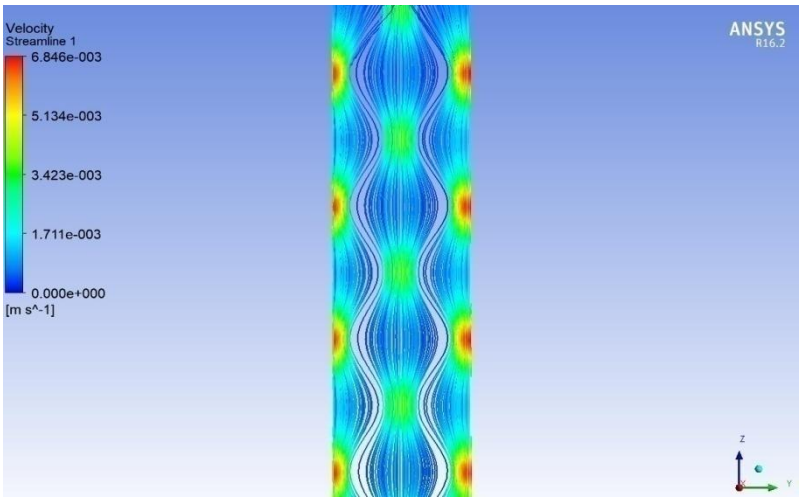

b)

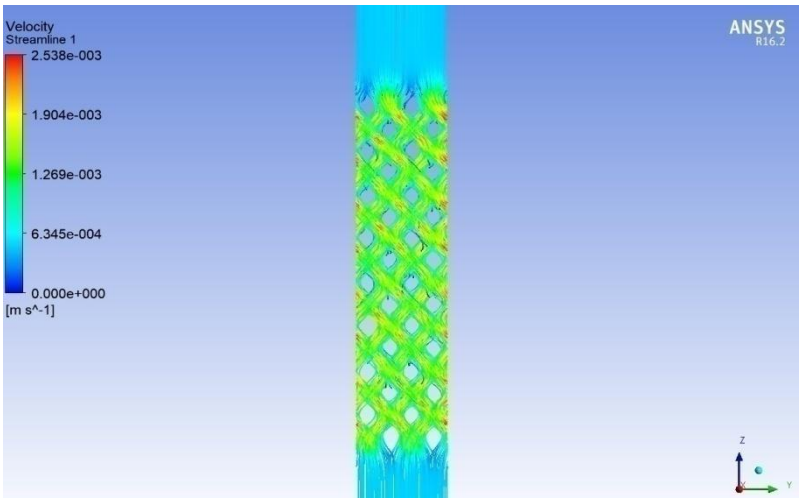

c)

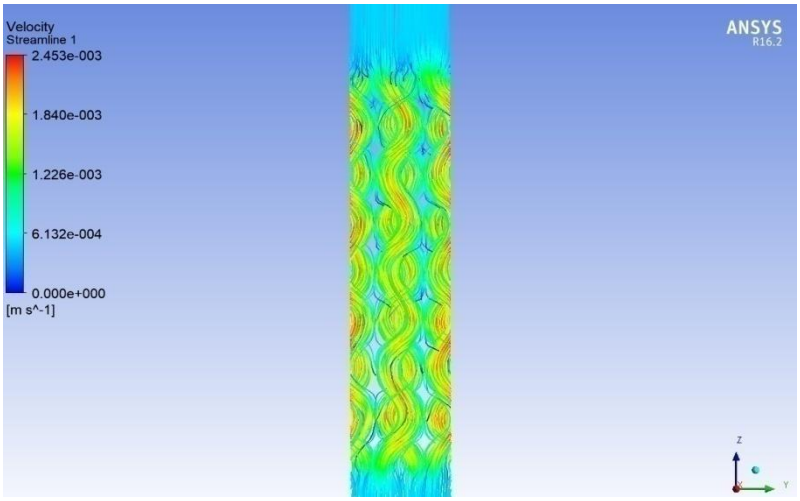

Figure 5.25. Side view of the streamlines of the a) SP70 scaffolds; b) SD70 scaffolds and c) SG70 scaffolds.

a)

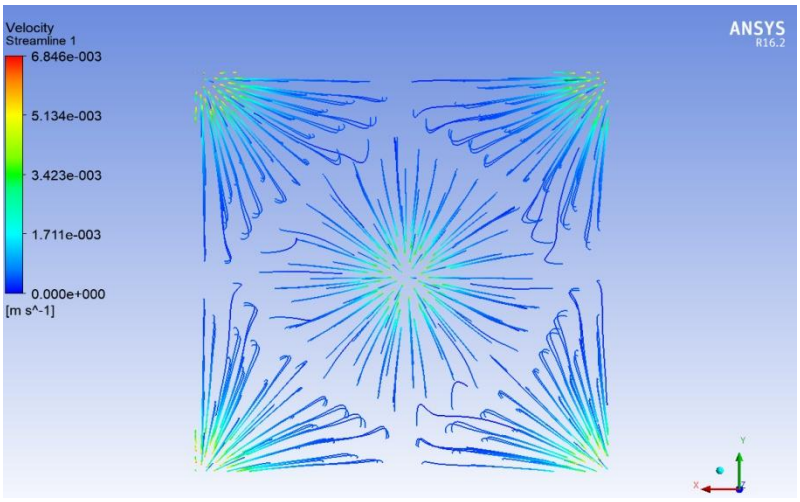

b)

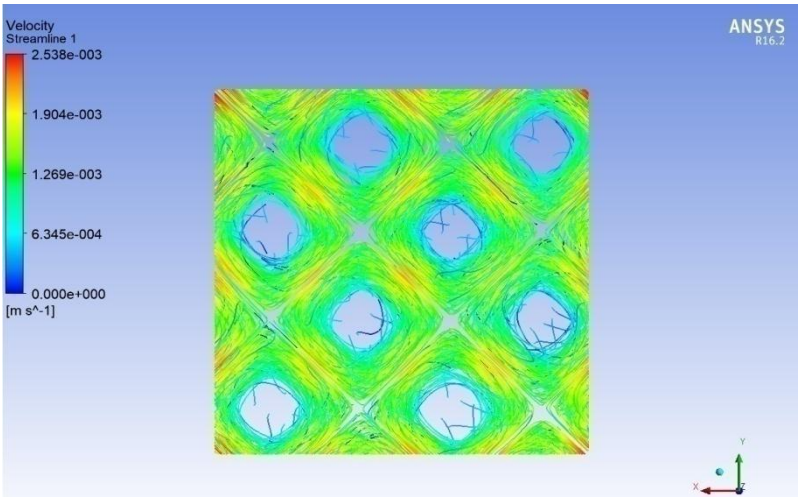

c)

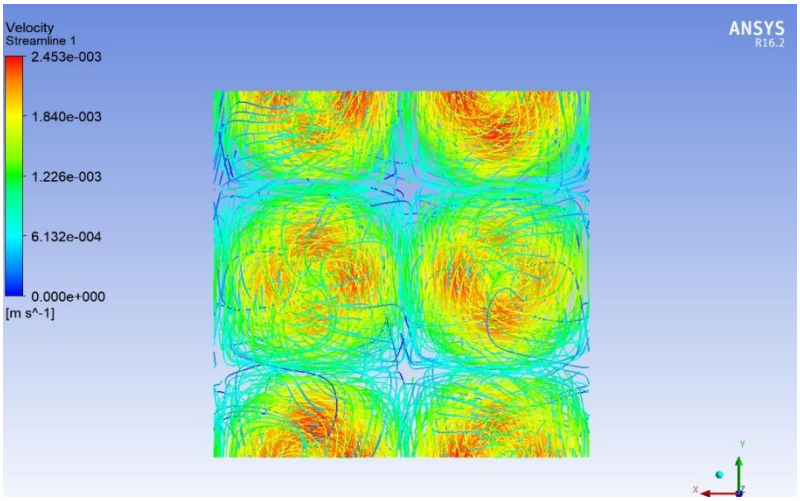

Figure 5.26. View from the outlet of the streamlines of the a) SP70 scaffolds; b) SD70 scaffolds and c) SG70 scaffolds.

Afterwards, comparisons were made to observe how different porosities and inlet flow rates influenced the streamlines for each TPMS geometry. For the changes in porosity, there were no significant changes for the SG and the SD scaffolds, other than increase in velocity and narrower paths for lower porosities (both of which were caused by a higher percentage of volume being taken up by the scaffold instead of the fluid). However, this was not the case that was observed for the SP scaffolds, as demonstrated in Figure 5.27.

Finally, when comparing the streamlines for inlet flow rates between 5ml/min and 100 ml/min, for 70% porous scaffolds, there were no noticeable differences for either the SD or SG scaffolds, other than an overall increase of the velocity across the simulations (which were expected because of the increased inlet velocity). However, when comparing these differences for the SP70 model, the distinctions were very apparent (Figure 5.28).

a)

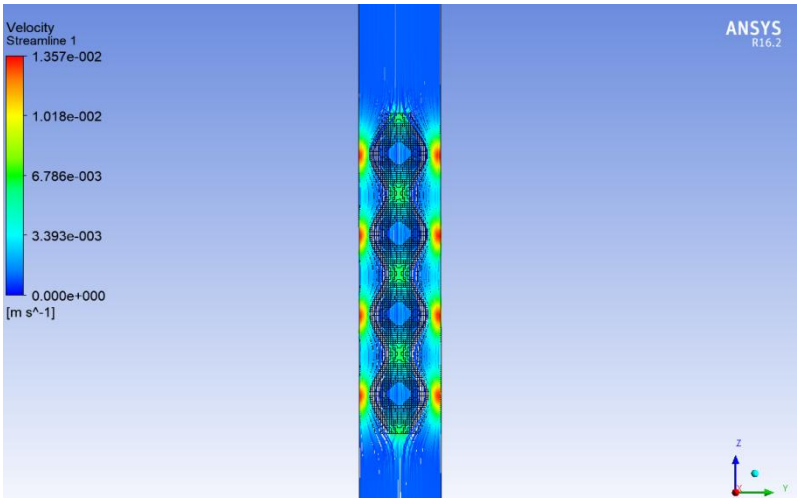

b)

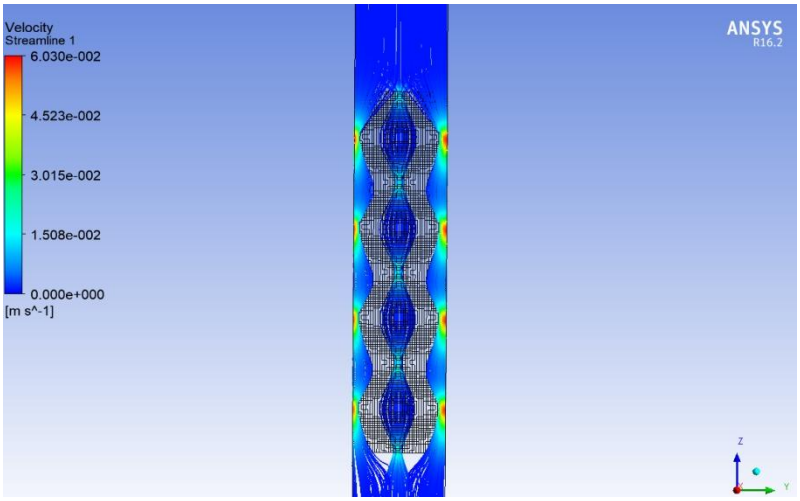

Figure 5.27. Sideview of the wireframe plus streamlines with an inlet flwo rate of 10 ml/min of a) the SP70 scaffold and b) the SP50 scaffold.

a)

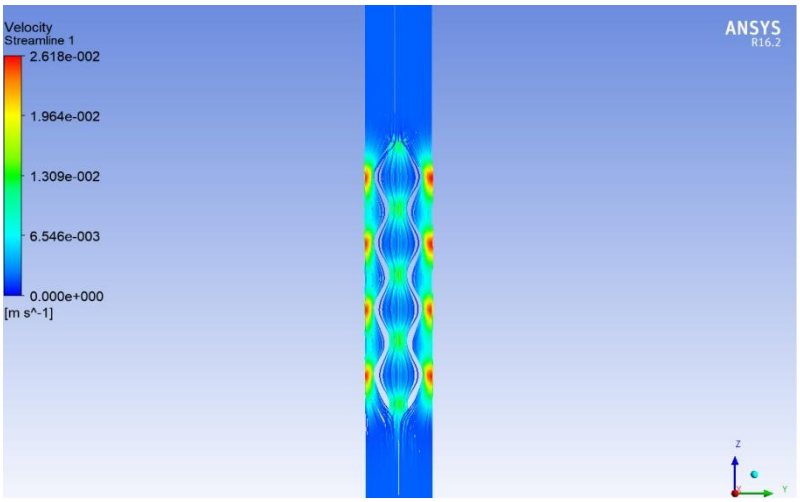

b)

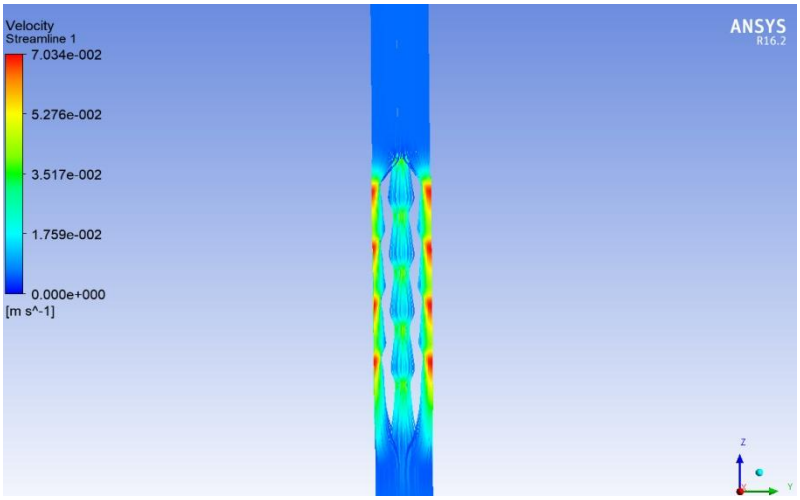

c)

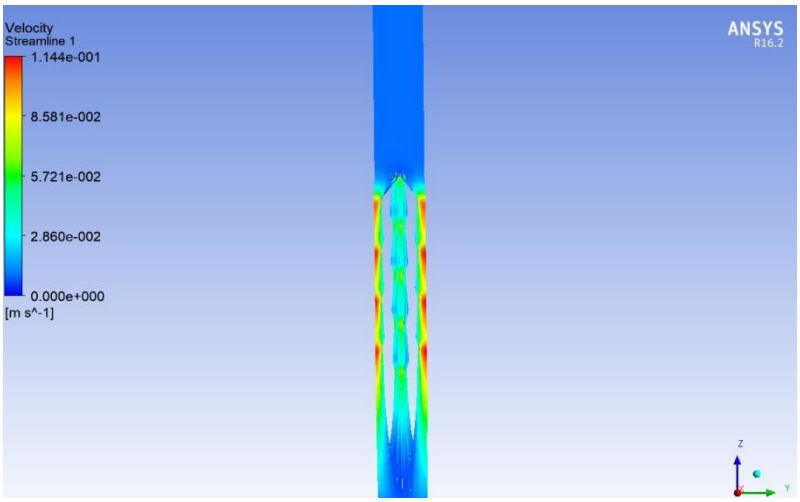

Figure 5.28. Sideview of the streamlines of the SP70 scaffold with a) 20 ml/min inlet flow rate; b) 60 ml/min inlet flow rate c) 100 ml/min inlet flow rate.

6. Discussion

The results obtained in the previous chapter will be analysed and discussed in further detail in the present chapter. The focus will be: the discussion of the differences between the three alternative modelling methods; the relation between the differences of a scaffold geometry and its permeability; the analysis of the fluid flow streamline and comparison between the computational and experimental results.

6.1. Model Comparison

From the three alternative models, the symmetric models are the ones that more accurately reflect the actual scaffolds inside the permeability chamber. This is because the symmetric models possess the same number of elements per side of a unitary scaffold, as would be used in an experimental setup (unlike the simplified models) and take into account the wall of the permeability chambers that cause an increase in the measured pressure (unlike the periodic models). In previous chapters (4.2.2 and 5.1), it was proven that the conditions required to employ the symmetric boundary are met (the boundary acts as a plane of symmetry and the fluid does not flow through the boundary), which means that this model can be applied to this work's simulations, even if only for the SP scaffolds.

Having exhibited the reliability of the symmetric models, the focus turns the periodic models, more specifically the correction factor of 0.833 calculated in chapter 5.4. As previously mentioned, this factor was calculated with the intention of including the effects of the chamber wall to the more simple periodic models. This would allow the periodic model, which is the one with the fewest elements and nodes (as seen on Table 4.1), to be used and analysed in place of any of the other more computational demanding models.

When comparing the permeabilities obtained from the symmetric model to the periodic model with the correction factor (Figure 5.16, Figure 5.17, Figure 5.18 and Figure 5.19), they are almost identical, with the error between the two almost always bellow 1%. This indicates how the periodic model with a correction factor of 0.833 is an excellent approximation for SP permeability simulations. However, without any simulations conducted with a complete model for either the SD or SG scaffolds, the correction factor for both of these geometries might be slightly different than the 0.833 factor for the SP. Nevertheless, this factor should still be a good approximation for the remaining scaffolds as a stand in for the influence of the chamber wall.

Moving onto the simplified model, the comparison between the simplified SP models and the symmetric SP models reveals how the simplified models always returned a lower permeability. In addition, the relation between the difference of permeability was never consistent across the four SP porosities, with the simplified SP50 having an average of around 50% lower permeability and the SP70 an average difference of around 7%. This discrepancy across the porosities signifies that they are dependent on the changes made to the geometry instead of an actual factor than could have

been accounted for. In other words, the cause of the lower permeabilities is not a systematic problem, but the fact that reducing the number of elements by half considerably alters the scaffold's geometry and, consequently, its permeability. Furthermore, the permeability of the scaffolds with a small cross sectional area of fluid passage (such as the SP50 scaffold), are the ones more influenced from any change to its geometry (which can be confirmed in the SP50 with the 50% decrease of their permeability).

Finally, the comparison between the corrected periodic model's permeabilities and the simplified model's permeabilities, shows that all of the simplified models always have a lower permeability to that of the corrected periodic model. This demonstrates how the inherent changes of the simplified model to the scaffolds geometry always results in a worse permeability. This raises a concern not only in computational tests, but also in experimental setups. As *Marin and Lacroix (2015)* previously found, changes in a scaffold's manufacturing process can greatly alter its fluidic properties. The results from the simplified models reveal how, similar to the imperfections in the printing process, small flaws in the simplified geometry will lead to a decrease in the scaffold's permeability. This means that besides the characteristics discussed by *Dias et al. (2012)* that influence a scaffold's permeability (pore size, porosity and permeability), there should also be a careful consideration of the refinement (the number of elements per side) of the CAD model being designed.

Beyond this, it can also be observed that the order of the permeability of the simplified models is the same as the one previously establish for the periodic model. The one exception is that in the simplified model, the permeability of the SP70 is higher than the SG70. However, since the permeability of the SG70 and SP70 are almost identical in both the periodic and simplified models, this minor difference can be attributed to a change in the geometry of the simplified models (that made the SG70 less permeable than the SP70) and/or a higher influence of the chamber's wall for the SG70 scaffold than the 0.833 correction factor (for example, a lower correction factor of 0.8 instead of 0.833 would account for the difference in the order). Nonetheless, the difference was immaterial. Therefore, this comparison reveals how both the periodic and simplified models, although not perfect, can be used as a means of determining which scaffolds are more permeable.

These results reveal how, for the purpose of obtaining the optimal permeability values, the periodic model is preferable because of the limitations of the simplified model (after applying the appropriate correction factor to the periodic model). In addition, because the periodic models represent fewer scaffold unitary cells, it is easier to observe and study the fluid flow inside it. Having this is mind, the analysis in the following chapters will be on the periodic models. Regarding the velocity, to attempt to use an illustrative velocity that falls in the domain of Darcy's law and can be compared with the experimental results, the inlet flow rate of 5 ml/min was chosen.

6.2. Geometry Influences

As previously mentioned, *Montazerian et al. (2017)* conducted a similar permeability study to the one in this work, regarding the permeability of TPMS scaffolds with different porosities (Figure 3.7). In spite of this, without the specifics of the scaffolds (how they were created and their refinement) a direct comparison between both sets of results would not be appropriate. Furthermore, *Montazerian et al. (2017)* studied a scaffold's normalized permeability instead of the measured permeability this work focuses on. Regardless, the study can still be used to verify and validate the order of permeability mentioned in previous chapters. *Montazerian et al. (2017)* first created the scaffolds and only then measured their porosity and permeabilities, meaning that, contrary to our work, for each of the three scaffold geometries, the measured porosities are always different. This invalidates the possibility of determining, for a given porosity, which are the more permeable geometries (like determining if SP70 or SG70 are the more permeable). Nevertheless, these results are still important for giving an overall view of the geometries' permeability as a whole. The normalized permeabilities of that study show that, for similar porosities, the SG geometries always had a higher permeability than the SD geometries. *Montazerian et al. (2017)* also found that the SP scaffolds were less permeable than the SD scaffolds at low porosities, but were more permeable at higher porosities. At high porosities the permeability values of the SP scaffolds were very close to the permeability values of the SG scaffolds. All of these results were also observed in the periodic models of the present work, which strengthen the validity of the results that were obtained in the CFD simulations.

Having corroborated this work's periodic model, the next step is a closer examination of these numerical results. As was expected, the periodic models reveal how, for the same geometry, a lower porosity results in a lower permeability. However, when comparing different geometries, a lower porosity was not an assurance of a lower permeability. An example of this is how the SG50 has a higher permeability than the SD60 even though it has a lower porosity. The results ultimately show that only increases of at least 20% porosity guaranty an increase of the scaffold's permeability (all 50% porous scaffolds had lower permeability than the 70% scaffolds and all 60% porous scaffolds had lower permeability than the 80% scaffolds). The results support the view that even though porosity is the main factor in determining a scaffold's permeability, if it's coupled with the choice of geometry there can be greater control over the precision of the permeability. This is important, because the differentiation cells inside a scaffold is dependent on the velocity of the fluid passing through them and the shear strain they are under *(Castro and Lacroix, 2017)*. Therefore, being able to more precisely control a scaffold's permeability would allow better control of the differentiation of cells inside the scaffold (seeing as both shear stress and fluid velocity are related to permeability).

A last observation that can be made to the numerical results is the aforementioned fact that for flow rates higher than 10 ml/min, there is a noticeable progressive decrease in the calculated permeability for all 12 scaffolds. This is because, as stated before, the Reynolds number of the fluid flow at those velocities is higher than 1 and, therefore, the application of Darcy's law results in some deviations.

Nevertheless, because of the inability to precisely determine the scaffold's pore size, Darcy's law is still the preferable method to determine their permeability.

6.3. Streamline Analysis

In this section, there will be an in depth analysis of the fluid streamlines from the different scaffolds in order to better understand and justify the differences described in the previous chapters.

Two major observations were made when the streamlines were analysed. First, the difference of the flow travel path for each geometry, secondly the volume occupied by the flow in the SP scaffolds. While the overview of the three scaffolds gives an idea of how the fluid flows in each of them, only the outlet view (alongside the other views) gives a clear view of the travel path. These different travel paths, for each scaffold, were the first major observation.

First of all, for each model there is not a singular path, but instead several paths with the same shape. These paths are: linear paths which expand in the interconnected areas for the SP scaffolds; circular helixes for the SG scaffolds and squared helixes for the SD scaffolds. Even though there are zones of connection between these paths, they never combine or separate. This means that there is always the same number of paths throughout the scaffold, as seen in Figure 5.24, Figure 5.25 and Figure 5.26.

The difference in the types of helixes between the SG and the SD explain why the latter always had a higher calculated permeability than the former. The more uniform circular helix of the SG scaffolds permitted the fluid to pass the scaffold without the interruptions brought on by the sharper angle in the edges of the squared helixes of the SD scaffolds. For this chosen permeability, the flow inside SP scaffolds also had a clear path (almost a straight line); therefore it makes sense that it would have a higher permeability than the SD scaffolds.

The other major observation relates to how the SP scaffolds was the only one of the scaffolds where there were large volumes without streamlines (indicating that when proceeding to cell seeding, the cells would not flow into these areas *(Marin et al., 2017a)*). The volumes were the paths could have merged, which were perpendicular to the fluid flow, presented an appealing zone where the cells could be deposited and differentiated. But if the flow does not pass through these zones, then the cells could never interact with them, meaning there is a less overall area of interaction between the scaffold walls and cells.

Regarding the analysis on how different inlet flow rates and different porosities could influence the streamlines, the only notable difference occurred in the SP scaffolds. Regarding the changing porosities, it was seen that the lower the porosity, the less volume was occupied by the streamlines inside the scaffold and the more length of the permeability chamber was required for the flow to

stabilize (Figure 5.27). The same behaviour happened for SP70 scaffolds with the increase in the inlet flow rate (Figure 5.28).

Finally, examining the behaviour of the fluid for a low porosity and a high inlet flow rate revealed a turbulent flow instead of a laminar flow. This occurrence explains why, in certain simulations of the SP50 at very high inlet flow rates, analysis was impossible (because of the instability of the flow, it was never laminar at the outlet).

In the end, all of the problems raised regarding the SP scaffolds stem from its design (straight channels connected between them). The fact the flow is not forced into any change of directions and being able to travel in an almost straight line, means that the cells might pass the scaffold without interacting with it at all, rendering the entire purpose of the scaffold moot. Furthermore, the changes in porosity affect the SP scaffolds much more than any of the other two geometries, because it directly determines the size of the holes where the fluid enters the scaffold. This means that the resulting smaller hole will cause the same amount of fluid to enter at a much higher speed, further reducing the interaction between the fluid and the inside of the scaffold. In terms of the other two scaffolds, although both present paths that force the interaction between the flow and the scaffold walls, the design of the SD geometries causes the overall lowest permeability of all three scaffolds (except for a porosity of 50%). This means the preferable option for scaffold design, that has both a high permeability and a travel path that leads the cells inside the flow to interact with the scaffold, is the Gyroid geometry. Nevertheless, the SD scaffolds presented the most stable permeability out of the three scaffolds regarding the increase in inlet flow rate. This means that the decrease in permeability for higher inlet flow rates was minimal for these scaffolds. Therefore, SD scaffolds might be the more preferable design in scenarios which involve fluids travelling at varying velocities and that have a need for a constant permeability.

6.4. Experimental comparison

In this section, there will be a more in depth look into the results obtain experimentally and how they compare to the numerical results.

The experimental setup shows some inconsistencies at the flow rates smaller than 5 ml/min, caused by the sensitivity of the pressure transducer not being able to accurately measure the considerable small changes of pressure associated with those flow rates. Furthermore, the experimental results appear to support what was seen in the numerical simulations: for 60% and 70% porosity the SG scaffolds are the most permeable and the SD scaffolds are the less permeable; for the same geometry the more porous scaffold is more permeable and at high inlet flow rates (above 20 ml/min) a decrease in the scaffolds' permeability occurs. However, the comparison between the experimental data with the numerical data reveals the numerical permeability values are between two to three times higher than the empirical values.

Nevertheless, the comparison between the sets of values (Figure 5.23) revealed, for each scaffold, a linear relation with an R^2 between 0.93 and 0.98, indicating a good correlation between both sets of results. Another comparison that analysed all of the points as a whole (Figure 5.22), instead of separating them by scaffold, found a R^2 equal to 0.886, indicating high correlation between the sets, but not as strong as the previous individual ones.

Having demonstrated the good correlation between the numerical and experimental data, the focus shifts towards the discrepancy between their values (with the numerical values of the permeability being almost three times higher than those of the experimental ones). In a similar permeability study, *Dias et al. (2012)* also obtained a good correlation between the calculated and measured permeability values of their scaffolds (R^2 = 0.9172), but also registered calculated values much higher than the measured ones, approximately four times higher. *Dias et al. (2012)* raised some possible explanations behind these inconsistencies, such as the disregarded surface effects of the materials like their roughness and wettability. These factors were also not taken into account in this work's simulations, which could have lead to higher permeability in the CFD values. These aspects were not taken into consideration in this work seeing as all similar permeability simulations normally disregard them (as established in chapter 3.2). However, the more complex scaffold geometries, in conjunction with the material's roughness and wettability, might have caused a drop in the measured permeability. This could also have been further compounded by the lack of a chamber wall in the simulations (even with the correction factor, the chamber wall combined with the surfaces effects might have lead to a significant increase in the pressure drop).

Another component that could justify the difference in values is the manufacturing process. As discussed in chapter 3.2, a scaffold's permeability can be greatly influence by small imperfections caused by the printing process. Another possibility that could result in a change to the geometry is the wax that was used as the printing support material. This material might not have been correctly removed from the inside of the scaffolds, given the nature of the process, resulting in blockages to the fluid flow and decreasing the permeability.

Finally, a factor that could also account for the decrease in permeability is how the whole permeability system was represented in the CFD model. Although the use of a squared permeability chamber instead of the full cylindrical chamber should not lead to a significant change in the permeability (as previously discussed in section 4.1.1), a problem might arise from not representing the rubber pipes attached to the chamber. These pipes, used in the experimental setup *(Castro et al., 2019),* have an inferior area to cross sectional area of the cylindrical chamber. This means that the fluid experiences a large change in velocity in order to pass from pipes to the chamber and from the chamber to the pipes. This shift in velocity, in conjunction with the increase in pressure resulting from the presence of the scaffold in the chamber (when compared to the empty chamber), might result in an additional increase in pressure registered by the pressure sensor.

7. Conclusions and Future research

This dissertation intended to understand how a scaffold's geometry could affect its permeability and how this was significant for BTE. This final chapter will present an overview of the results obtained from this work as well as discuss possible future research in this area.

7.1 Conclusions

The focus of this work was to better the understanding of the relation between a scaffold's design (geometry and porosity) and its permeability, in order to determine the optimal scaffold geometry for BTE applications. To achieve this, three different TPMS geometries with four different porosities were tested, for a total of twelve different scaffolds, using numerical models. The tests allowed us to conclude that the SP scaffolds are unsuitable for most BTE applications and that SG scaffolds present the best characteristics for this end. The tests also allowed us to conclude that a scaffold's permeability is highly influenced, not only by its porosity, but also by its geometry.

The values obtained from the numerical simulations were considered valid given their good correlation with experimental results, despite the differences between both sets of values (this was attributed to the simplifications of the numerical models and the imprecisions of the scaffold manufacturing process). Furthermore, the computational results were also were coherent with the findings of previous studies of TPMS scaffolds, regarding the permeability order of the different scaffolds designs.

The high computational demand from the attempt to represent the entire permeability chamber lead to the creation of three types of alternative models: symmetrical models, simplified models and periodic models. When comparing these three models, the symmetric models were the closest to the full model because they included the chamber walls and the same geometry as the experimental setup. However, the fact that only one of the three geometries could be represented with this model (the SP geometry), led to the model having very limited applications, unlike the other models.

The simplified model was the only model that allowed for the representation of the entire chamber, but it compromised the precision of the scaffold. This resulted in a decrease in the calculated permeability of the scaffolds when compared to the symmetrical model (this decrease varied between 7% and 50%, depending on the scaffold). This fact also raised concern regarding similar simplifications on CAD models of 3D printed scaffolds, which might also caused changes in their permeability.

The periodic models revealed much better results than the simplified models because they kept the original structure of the scaffold. However, the permeability values of the periodic models were higher than symmetrical models, most likely because of the lack of the effect of the chamber wall. To correct this, a correction factor of 0.833 (obtain by comparing the SP values of the symmetrical and periodic models) was applied to all of the periodic models. The problem with this correction factor was that it

was obtained from the analysis of only one geometry, meaning it might be different for the SD or SG scaffolds. Nevertheless, these corrected periodic models were the chosen models to analyse the scaffolds because they offered the best results while still being applicable to all twelve scaffolds.

The permeabilities obtained from the corrected periodic models revealed how a higher porosity did not necessarily mean a higher permeability. This meant that the correct choice of geometry, alongside porosity, could allow for a greater precision regarding the scaffold's permeability.

Afterwards, the analysis of the streamlines showed how the SP scaffolds were the ones most influenced by shifts in the porosity and inlet flow rate. Furthermore, because of the path that the fluid, and consequently the cells, would follow inside this scaffold, it was demonstrated that there was a limited interaction between these cells and the scaffold walls. Therefore, the SP geometry was revealed not to have the necessary qualities to promote cell seeding inside the scaffold.

Regarding the SD scaffolds, these were found to be the less permeable but the most consistent out of the three (relative to fluid velocities). Because of these characteristics, the SD scaffolds were determined as not to be a suitable geometry for most cases, unless there was a specific requirement for a scaffold with a constant permeability at various fluid velocities.

Finally, the SG scaffolds had the overall highest permeability values and travel paths that promoted cell-scaffold interactions. Because of this, the SG geometry was recognized as the most advisable scaffold choice for most situations.

7.2 Future research

The results obtained throughout this dissertation underline the importance of numerical analysis and CFD models in the study of scaffolds with applications in BTE. However, alongside these results, several possibilities for further study around this subject emerged.

A possibility for a future study is developing and analysing a complete model of not only the permeability chamber, but the entire experimental setup. This complete model would possess a much higher computational cost than any of the models that were considered for this work. Nevertheless, this more precise model would eliminate many of the errors associated with the simplifications, namely using a squared chamber instead of a cylindrical one; not knowing the true influence of the chamber walls and testing the remainder of the experimental setup (such as the pipes attached to the ends of the chamber).

An alternative to designing models and running numerical simulations for all twelve possibilities would be to run a model for each of the three geometries (for example testing only the 70% porous models). Using this method, the tested models could be used to determine the influence of the unaccounted factors (the pipes, the cylindrical chamber and the chamber wall in the SD and SG models) for a less computationally demanding model, such as the periodic models used in this work.

Another interesting study that could be undertaken involves examining how the number of elements per side of the scaffold models influences the permeability values, or in other words, a convergence test of the mesh used to design the models. This test would be relevant not only in a numerical sense but also in determining how the precision of the model affects the permeability of the printed scaffolds. To achieve this, there could be either a test with a single scaffold with an increasing number of elements or a similar setup to the periodic model described in this work (this model would be more computationally demanding but would allow the visualization of the interaction inside a more complex scaffold).

In addition, a factor that was not taken into account in this work was the influence of gravity forces. As discussed by *Marin et al. (2017b)*, gravity influences how the fluid flows through the scaffold and, consequently, how the cells would interact with it. Therefore, the addition of gravity might reveal new solutions to force the desired cell seeding (for example, forcing the cells to travel into the areas of the SP scaffolds they wouldn't have otherwise) or new complications that would need to be overcome. However, it should be highlighted that this area of research would be more significant in the field of bioreactors than in bone implants.

Another type of design that was not discussed and that could present interesting applications in the creation of scaffolds consist on the combination of different geometries *(Yang et al., 2014)*. These scaffolds would allow for portions of them to have different permeabilities (different porosities and/or geometries) and could be a possible better mimic for bone structure (with a more permeable geometry for trabecular bone portion and another less permeable geometry for the compact bone portion).

Finally, an interesting research could be the study the permeabilities of the different bones in the human body and the assignment the optimal scaffold design to each type of bone according to its permeability.

In the end, this work presents itself as a contribution that will hopefully make an impact in the promising and ever developing area of Tissue Engineering.

Bibliography

Ali, D. and Sen, S. (2018). Permeability and fluid flow-induced wall shear stress of bone tissue scaffolds: Computational fluid dynamic analysis using Newtonian and non-Newtonian blood flow models. *Computers in Biology and Medicine*, 99, pp.201-208.

Almeida, F.F.L.S. (2015), *Estudo teórico-experimental de um sistema de medição de permeabilidade*. Masters Thesis in Mechanical Engineering, Instituto Superior Técnico, Universidade de Lisboa.

Brunelli, M., Perrault, C. and Lacroix, D. (2017). Mechanical response of 3D Insert ® PCL to compression. *Journal of the Mechanical Behavior of Biomedical Materials*, 65, pp.478-489.

Castro, A. and Lacroix, D. (2017). Micromechanical study of the load transfer in a polycaprolactone–collagen hybrid scaffold when subjected to unconfined and confined compression. *Biomechanics and Modeling in Mechanobiology*, 17(2), pp.531-541.

Castro, A., Pires, T., Santos, J., Gouveia, B. and Fernandes, P. (2019). Permeability versus Design in TPMS Scaffolds. *Materials*, 12(8).

Chandran, K., Rittgers, S. and Yoganathan, A. (2012). *Biofluid mechanics*. Boca Raton: CRC Press, Taylor & Francis Group.

Chor, M. and Li, W. (2006). A permeability measurement system for tissue engineering scaffolds. *Measurement Science and Technology*, 18(1), pp.208-216.

Currie, I. (2012) *Fundamental Mechanics of Fluids, Fourth Edition*. Boca Raton: CRC Press, Taylor & Francis Group

Darcy, H. (1856). Les Fontaines Publiques de la Ville de Dijon, Dalmont, Paris,1856.

Dias, M., Fernandes, P., Guedes, J. and Hollister, S. (2012). Permeability analysis of scaffolds for bone tissue engineering. *Journal of Biomechanics*, 45(6), pp.938-944.

Dinis, J., Morais, T., Amorim, P., Ruben, R., Almeida, H., Inforçati, P., Bártolo, P. and Silva, J. (2014). Open Source Software for the Automatic Design of Scaffold Structures for Tissue Engineering Applications. *Procedia Technology*, 16, pp.1542-1547.

El-Rashidy, A., Roether, J., Harhaus, L., Kneser, U. and Boccaccini, A. (2017). Regenerating bone with bioactive glass scaffolds: A review of in vivo studies in bone defect models. *Acta Biomaterialia*, 62, pp.1-28.

Hutmacher, D., Schantz, J., Lam, C., Tan, K. and Lim, T. (2007). State of the art and future directions of scaffold-based bone engineering from a biomaterials perspective. *Journal of Tissue Engineering and Regenerative Medicine*, 1(4), pp.245-260.

Jones, K. (1962). On the differential form of Darcy's law. *Journal of Geophysical Research*, 67(2), pp.731-732.

Jung, Y. and Torquato, S. (2005). Fluid permeabilities of triply periodic minimal surfaces. *Physical Review E*, 72(5).

Kelly, C., Miller, A., Hollister, S., Guldberg, R. and Gall, K. (2017). Design and Structure-Function Characterization of 3D Printed Synthetic Porous Biomaterials for Tissue Engineering. *Advanced Healthcare Materials*, 7(7).

Marin, A. and Lacroix, D. (2015). The inter-sample structural variability of regular tissue-engineered scaffolds significantly affects the micromechanical local cell environment. *Interface Focus*, 5(2).

Marin, A., Grossi, T., Bianchi, E., Dubini, G. and Lacroix, D. (2017a). µ-Particle tracking velocimetry and computational fluid dynamics study of cell seeding within a 3D porous scaffold. *Journal of the Mechanical Behavior of Biomedical Materials*, 75, pp.463-469.

Marín, A., Brunelli, M. and Lacroix, D. (2017b). Flow perfusion rate modulates cell deposition onto scaffold substrate during cell seeding. *Biomechanics and Modeling in Mechanobiology*, 17(3), pp.675-687.

Marques, V.R.S. (2013), *Permeability Analysis of Scaffolds in Bone Tissue Engineering using Computational Fluid Dynamics*. Masters Thesis in Mechanical Engineering, Instituto Superior Técnico, Universidade de Lisboa.

McDonough, J. M. (2009). *Lectures in elementary fluid dynamics: Physics, Mathematics and applications*, lecture notes. Lexington, KY: Departments of Mechanical Engineering and Mathematics, University of Kentucky.

Melchels, F., Barradas, A., van Blitterswijk, C., de Boer, J., Feijen, J. and Grijpma, D. (2010). Effects of the architecture of tissue engineering scaffolds on cell seeding and culturing. *Acta Biomaterialia*, 6(11), pp.4208-4217.

Mohee, L., Offeddu, G., Husmann, A., Oyen, M. and Cameron, R. (2019). Investigation of the intrinsic permeability of ice-templated collagen scaffolds as a function of their structural and mechanical properties. *Acta Biomaterialia*, 83, pp.189-198.

Montazerian, H., Zhianmanesh, M., Davoodi, E., Milani, A. and Hoorfar, M. (2017). Longitudinal and radial permeability analysis of additively manufactured porous scaffolds: Effect of pore shape and porosity. *Materials & Design*, 122, pp.146-156.

Moukalled, F., Mangani, L. and Darwish. M. (2016). *The finite volume method in computational fluid dynamics*. Cham, Switzerland: Springer.

Ochoa, I., Sanz-Herrera, J., García-Aznar, J., Doblaré, M., Yunos, D. and Boccaccini, A. (2009). Permeability evaluation of 45S5 Bioglass®-based scaffolds for bone tissue engineering. *Journal of Biomechanics*, 42(3), pp.257-260.

Oh, S., Oh, N., Appleford, M. and Ong, J. (2006). Bioceramics for Tissue Engineering Applications - A Review. *American Journal of Biochemistry and Biotechnology*, 2(2), pp.49-56.

Orr, D. and Burg, K. (2008). Design of a Modular Bioreactor to Incorporate Both Perfusion Flow and Hydrostatic Compression for Tissue Engineering Applications. *Annals of Biomedical Engineering*, 36(7), pp.1228-1241.

Pennella, F., Cerino, G., Massai, D., Gallo, D., Falvo D'Urso Labate, G., Schiavi, A., Deriu, M., Audenino, A. and Morbiducci, U. (2013). A Survey of Methods for the Evaluation of Tissue Engineering Scaffold Permeability. *Annals of Biomedical Engineering*, 41(10), pp.2027-2041.

Pillai, K. and Advani, S. (1995). Numerical and analytical study to estimate the effect of two length scales upon the permeability of a fibrous porous medium. *Transport in Porous Media*, 21(1), pp.1-17.

Porter, J., Ruckh, T. and Popat, K. (2009). Bone tissue engineering: A review in bone biomimetics and drug delivery strategies. *Biotechnology Progress*, p.1539-1560.

Rahbari, A., Montazerian, H., Davoodi, E. and Homayoonfar, S. (2016). Predicting permeability of regular tissue engineering scaffolds: scaling analysis of pore architecture, scaffold length, and fluid flow rate effects. *Computer Methods in Biomechanics and Biomedical Engineering*, 20(3), pp.231-241.

Sikavitsas, V., Temenoff, J. and Mikos, A. (2001). Biomaterials and bone mechanotransduction. *Biomaterials*, 22(19), pp.2581-2593.

Skalak R. (1988). *Tissue Engineering: Proceedings of a Workshop, Held at Granlibakken, Lake Tahoe, California, February 26–29, 1988*. New York: Liss

Tan, L., Yu, X., Wan, P. and Yang, K. (2013). Biodegradable Materials for Bone Repairs: A Review. *Journal of Materials Science & Technology*, 29(6), pp.503-513.

Tortora, G. and Derrickson, B. (2014). *Principles of anatomy & physiology*. 14th ed. John Wiley & Sons, pp.170-175.

Truscello, S., Kerckhofs, G., Van Bael, S., Pyka, G., Schrooten, J. and Van Oosterwyck, H. (2012). Prediction of permeability of regular scaffolds for skeletal tissue engineering: A combined computational and experimental study. *Acta Biomaterialia*, 8(4), pp.1648-1658.

Vijayavenkataraman, S., Zhang, L., Zhang, S., Hsi Fuh, J. and Lu, W. (2018). Triply Periodic Minimal Surfaces Sheet Scaffolds for Tissue Engineering Applications: An Optimization Approach toward Biomimetic Scaffold Design. *ACS Applied Bio Materials*, 1(2), pp.259-269.

Yang, N., Quan, Z., Zhang, D. and Tian, Y. (2014). Multi-morphology transition hybridization CAD design of minimal surface porous structures for use in tissue engineering. *Computer-Aided Design*, 56, pp.11-21.

Appendix

Experimental data

Table 1. Measured pressure drop for the experimental setup.

Flow rate (ml/min)	$\Delta P_{Measured}$ (Pa)						
	SP60	SD60	SG60	SP70	SD70	SG70	Empty
1	1.604	1.975	1.587	1.180	1.577	1.265	0.911
2	3.368	4.178	3.292	2.917	3.393	2.810	2.171
3	5.153	6.414	4.966	4.421	5.298	4.274	3.278
4	7.052	8.769	6.76	5.876	7.152	5.662	4.579
5	8.718	11.066	8.356	7.484	8.882	6.984	5.675
10	18.667	22.939	17.402	15.731	18.787	14.638	12.126
20	43.214	49.270	38.091	35.212	40.600	32.483	27.056
40	109.326	116.420	89.801	88.045	97.550	78.600	67.084
60	190.234	197.582	154.477	156.524	166.522	136.766	117.258
80	285.862	290.342	229.444	228.071	245.626	203.022	171.694
100	391.652	397.400	315.868	313.297	335.681	277.854	239.667

Table 2. Calculated pressure drop for the experimental setup.

Flow rate (ml/min)	$\Delta P_{Scaffold}$ (Pa)					
	SP60	SD60	SG60	SP70	SD70	SG70
1	0.693	1.064	0.676	0.269	0.666	0.354
2	1.197	2.007	1.121	0.746	1.222	0.639
3	1.875	3.136	1.688	1.143	2.020	0.996
4	2.473	4.190	2.181	1.297	2.573	1.083
5	3.043	5.391	2.681	1.809	3.207	1.309
10	6.541	10.813	5.276	3.605	6.661	2.512
20	16.158	22.214	11.035	8.156	13.544	5.427
40	42.242	49.336	22.717	20.961	30.466	11.516
60	72.976	80.324	37.219	39.266	49.264	19.508
80	114.168	118.648	57.750	56.377	73.932	31.328
100	151.985	157.733	76.201	73.630	96.014	38.187

Table 3. Resulting permeability for the experimental setup of the 60% porous scaffolds.

Flow rate (ml/min)	Permeability (mm^2)		
	SP60	SD60	SG60
1	$1.85 * 10^{-3}$	$1.21 * 10^{-3}$	$1.90 * 10^{-3}$
2	$2.14 * 10^{-3}$	$1.28 * 10^{-3}$	$2.29 * 10^{-3}$
3	$2.05 * 10^{-3}$	$1.23 * 10^{-3}$	$2.28 * 10^{-3}$
4	$2.07 * 10^{-3}$	$1.22 * 10^{-3}$	$2.35 * 10^{-3}$
5	$2.11 * 10^{-3}$	$1.19 * 10^{-3}$	$2.39 * 10^{-3}$
10	$1.96 * 10^{-3}$	$1.19 * 10^{-3}$	$2.40 * 10^{-3}$
20	$1.59 * 10^{-3}$	$1.15 * 10^{-3}$	$2.32 * 10^{-3}$
40	$1.21 * 10^{-3}$	$1.04 * 10^{-3}$	$2.26 * 10^{-3}$
60	$1.05 * 10^{-3}$	$0.96 * 10^{-3}$	$2.07 * 10^{-3}$
80	$0.90 * 10^{-3}$	$0.86 * 10^{-3}$	$1.78 * 10^{-3}$
100	$0.84 * 10^{-3}$	$0.81 * 10^{-3}$	$1.68 * 10^{-3}$

Table 4. Resulting permeability for the experimental setup of the 70% porous scaffolds.

Flow rate (ml/min)	Permeability (mm^2)		
	SP70	**SD70**	**SG70**
1	$4.77 * 10^{-3}$	$1.93 * 10^{-3}$	$3.62 * 10^{-3}$
2	$3.44 * 10^{-3}$	$2.10 * 10^{-3}$	$4.01 * 10^{-3}$
3	$3.37 * 10^{-3}$	$1.90 * 10^{-3}$	$3.86 * 10^{-3}$
4	$3.95 * 10^{-3}$	$1.99 * 10^{-3}$	$4.74 * 10^{-3}$
5	$3.54 * 10^{-3}$	$2.00 * 10^{-3}$	$4.90 * 10^{-3}$
10	$3.56 * 10^{-3}$	$1.93 * 10^{-3}$	$5.10 * 10^{-3}$
20	$3.14 * 10^{-3}$	$1.89 * 10^{-3}$	$4.73 * 10^{-3}$
40	$2.45 * 10^{-3}$	$1.68 * 10^{-3}$	$4.45 * 10^{-3}$
60	$1.96 * 10^{-3}$	$1.56 * 10^{-3}$	$3.94 * 10^{-3}$
80	$1.82 * 10^{-3}$	$1.39 * 10^{-3}$	$3.27 * 10^{-3}$
100	$1.74 * 10^{-3}$	$1.34 * 10^{-3}$	$3.36 * 10^{-3}$

ANSYS FLUENT Parameters

Double Precision Solver

Because of the nature of the scaffolds being studying, namely their multiple enclosures interconnected between themselves, the ANSYS FLUENT 16.2 User's Guide advices the use of the double-precision solvers instead of single-precision solvers. This is to resolve the pressure differences that drive the flow (which are much smaller than the pressure levels).

Velocity formulation

There exist two distinct parameters for velocity formulation, those being relative velocity formulation and absolute velocity formulation. The former is preferable for situations where most of the fluid in the domain is moving, such as the case of a large impeller in a tank of a similar size. The latter formulation is preferable in the opposite situations, that is, when most of the flow in the domain is not moving. Since in the case of the scaffolds plus the chamber the fluid flow is mostly unidirectional and there exist no rotations, the absolute velocity formulation is therefore preferable.

Flow Solver

For the flow solvers there exist two distinct options: pressure-based and density-based solvers. The chosen solver for this work was the pressure-based solver, since it is used for smaller velocities and non-compressible fluids (which are the exact conditions being studied), whereas the density-based solver is normally reserved for higher velocities and/or compressible fluids. The pressure-based solver consists on the application of the projection method to solve the continuity and momentum equations in an iterative manner, where the equations are solved repeatedly until the solutions converge (or until a predetermined threshold is reached).

Spatial Discretization Scheme - Gradient

Concerning special discretization schemes, there exist three alternatives: Least Squares Cell-Based gradient (LSCB), Green-Gauss Cell-Based gradient and Green-Gauss Node-Based gradient. Of the two Green-Gauss gradient, the node-based gradient is much more accurate that the cell-based gradient, therefore the Green-Gauss Cell-Based gradient was disregarded. Finally, between the two remaining methods LSCB returns results with comparable accuracy to the Green-Gauss Node-Based gradient, but with a much lower computing cost, making it the optimal choice for this parameter.

Pressure and Momentum scheme

For both the pressure and momentum interpolation, the standard approach was tested and accepted. These parameters, for both pressure and momentum, were second-order upwind schemes. Upwind means that the values for the cells are obtained from the ones that are upstream. Second order is used to reduce the risk of the occurrence of diffusion of the results, increasing the accuracy of the solution.

Solution controls

Because of the laminar nature of the flow, as discussed before, the ANSYS FLUENT 16.2 User's Guide advices with using the SIMPLE solution method. For the values of pressure, density, body force and momentum under relaxation, the pre-established values were chosen (those values being 0.3, 1, 1 and 0.7 respectively).

Monitoring Residuals

For the monitoring residuals, values up to 10^{-5} were tested and, in the end, it was decided to use residuals of 10^{-4} for the residuals of the continuity equation, x, y and z. This was because it was significantly faster than the 10^{-5} residuals and resulted in margins of error inferior to 0.1% (when compared to the results obtained using 10^{-5} residuals).